[redacted]

CENTRAL RESEARCH LIBRARY
DOCUMENT COLLECTION

1

OAK RIDGE NATIONAL LABORATORY
operated by
UNION CARBIDE CORPORATION
NUCLEAR DIVISION
for the
U.S. ATOMIC ENERGY COMMISSION

UNION CARBIDE

ORNL-TM-1700

MARTIN MARIETTA ENERGY SYSTEMS LIBRARIES
3 4456 0060134 7

DECLASSIFIED
CLASSIFICATION CHANGED TO
BY AUTHORITY OF AECM-2104 a 2 B6 8/24/74
BY: BL Rudd

FUELS AND MATERIALS DEVELOPMENT PROGRAM QUARTERLY PROGRESS REPORT FOR PERIOD ENDING SEPTEMBER 30, 1966

CENTRAL RESEARCH LIBRARY
DOCUMENT COLLECTION
LIBRARY LOAN COPY
DO NOT TRANSFER TO ANOTHER PERSON
If you wish someone else to see this document, send in name with document and the library will arrange a loan.

NOTICE This document contains information of a preliminary nature and was prepared primarily for internal use at the Oak Ridge National Laboratory. It is subject to revision or correction and therefore does not represent a final report.

[redacted]

LEGAL NOTICE

This report was prepared as an account of Government sponsored work. Neither the United States, nor the Commission, nor any person acting on behalf of the Commission:

A. Makes any warranty or representation, expressed or implied, with respect to the accuracy, completeness, or usefulness of the information contained in this report, or that the use of any information, apparatus, method, or process disclosed in this report may not infringe privately owned rights; or

B. Assumes any liabilities with respect to the use of, or for damages resulting from the use of any information, apparatus, method, or process disclosed in this report.

As used in the above, "person acting on behalf of the Commission" includes any employee or contractor of the Commission, or employee of such contractor, to the extent that such employee or contractor of the Commission, or employee of such contractor prepares, disseminates, or provides access to, any information pursuant to his employment or contract with the Commission, or his employment with such contractor.

[redacted]

ORNL-TM-1700

Contract No. W-7405-eng-26

FUELS AND MATERIALS DEVELOPMENT PROGRAM QUARTERLY PROGRESS REPORT FOR PERIOD ENDING SEPTEMBER 30, 1966

Compiled by

P. Patriarca

DECEMBER 1966

OAK RIDGE NATIONAL LABORATORY
Oak Ridge, Tennessee
operated by
UNION CARBIDE CORPORATION
for the
U.S. ATOMIC ENERGY COMMISSION

[redacted]

MARTIN MARIETTA ENERGY SYSTEMS LIBRARIES

3 4456 0060134 7

[redacted]

FOREWORD

This is the tenth quarterly progress report describing work performed at the Oak Ridge National Laboratory for the Fuels and Materials Branch, Division of Reactor Development and Technology, U.S. Atomic Energy Commission. A new program, Weldability of Nickel-Bearing Alloys, was started during the past quarter and its progress is summarized in this report. The specific programs covered are as follows:

Part I. Metals and Ceramics Division

Program Title	Person in Charge	Principal Investigator(s)
Controlled Precipitation in Nuclear Materials	W. O. Harms	J. L. Scott and J. P. Hammond
Fuel Element Development	G. M. Adamson, Jr.	W. R. Martin and C. F. Leitten, Jr.
Nondestructive Test Development	W. O. Harms	R. W. McClung
Zirconium Metallurgy	C. J. McHargue	M. L. Picklesimer
Sintered Aluminum Products	G. M. Adamson, Jr.	W. R. Martin and C. F. Leitten, Jr.
Weldability of Nickel-Bearing Alloys	G. M. Adamson, Jr.	G. M. Slaughter

Part II. Reactor Chemistry Division

Fission-Gas Release and Physical Properties of Fuel Materials During Irradiation	O. Sisman	R. M. Carroll and J. G. Morgan

Part III. Solid State Division

Irradiation Effects on Alloys and Structural Materials	D. S. Billington	J. T. Stanley

[redacted]

[redacted]

CONTENTS

Page

Summary ix

Part I. Metals and Ceramics Division

1. Controlled Precipitation in Nuclear Materials 3
   - Production of Fine Precipitates in Uranium Nitride 3
     - Molybdenum Additions 4
     - Thorium and Oxygen Additions 10
   - Controlled Precipitation in Thorium Alloys 12
2. Fuel Element Development 19
   - Deposition of Uranium Dioxide by Hydroreduction of Uranium Hexafluoride 19
   - Preparation of PuO_2 Powder from PuF_6 by Thermochemical Reduction 20
   - Deposition of Uranium Compounds by Lithium Vapor Reduction of UF_6 20
   - Deposition of Tungsten Alloys 22
3. Nondestructive Test Development 29
   - Electromagnetic Test Methods 29
     - Analytical Studies 29
     - Phase-Sensitive Eddy-Current Instrument 30
     - Spacing Measurements 30
   - Ultrasonic Test Methods 30
     - Fabrication of Reference Notches 30
     - Optical System 31
   - Penetrating Radiation Methods 32
4. Zirconium Metallurgy 33
   - Anisotropy in Zircaloy-2 and Zircaloy-4 33
     - Zircaloy Tubing Acquisition 33
     - Determination of Average Basal Pole Figures 34
     - Preferred Orientation in Zircaloy Tubing 35
     - Multiaxial Testing of Tubing 37

[redacted]

[redacted]

Stress Orientation of Hydrides in Zircaloy-2 37
Effects of Cooling Rate 38
Temperature Cycling Under Load 40
Orientation of Hydrides in Unstressed Tubing 40
Studies of Zirconium Alloys in Shear 43
Optical Properties of Zirconium Alloys 45
Oxide Film Studies 48
Properties of High-Purity Zirconium 52
Anisotropy of Oxidation in Zirconium 52
5. Sintered Aluminum Products Development 54
Powder Characteristics 54
Dispersion Preparation 56
Ball Milling 56
Controlled Oxidation of Aluminum Powders 57
Powder Consolidation 58
Evaluation of Product 60
High-Temperature Stability of Alloy after Extrusion . . 60
Identification of the Oxide Species in Extruded SAP Rods 63
Mechanical Properties Evaluation 64
Microstructural Evaluation 79
Nondestructive Testing Development 85
6. Weldability of Nickel-Bearing Alloys 90
Special Alloy Fabrication 90
Weldability Studies 92
VARESTRAINT Testing Performed Under Subcontract at Rennselaer Polytechnic Institute 92
Hot-Ductility Testing 97
Influence of Flaws on Properties of Nickel-Bearing Alloys 99

Part II. Reactor Chemistry Division

Fission-Gas Release and Physical Properties of Fuel Materials During Irradiation 105
Fission-Gas Release 105

[redacted]

[redacted]

Thermal Conductivity of UO_2 During Irradiation 105
General Theory 107
Thermocouple Transfer Function 108
Modification of Experimental Procedure 109
Response of UO_2 to Electrical Potentials 109

Part III. Solid State Division

Irradiation Effects on Alloys and Structural Materials 115
Radiation Effects on Pressure-Vessel Steels 115
Neutron Dosimetry 120
Stress-Grain Size Analysis of the Ductile-Brittle Transition for Steel and Similar Metals 125
Radiation Hardening in Iron 128
Tensile Tests 129
Transmission Electron Microscopy 132
Discussion 136
Effect of the Number of Zone Passes on the Flow Stress of Niobium Single Crystals 137
Experimental Procedure 138
Results and Discussion 139
Conclusions 143
Dependence of Yield Stress on Neutron Dose in Niobium Single Crystals 143
Materials and Experimental Procedure 145
Experimental Results and Discussion 150
Stress Dependence of Dislocation Velocity in Irradiated and Unirradiated Niobium 155
The Interaction of Radiation Produced Defects and Interstitial Impurity Atomis in Niobium 163
Specimen Preparation 163
Internal Friction Measurements in Unirradiated Niobium . 164
Irradiation Procedure and Results 167
Discussion of Results 169
Fission Flux Converter Facility for the BSR 172

[redacted]

SUMMARY

PART I. METALS AND CERAMICS DIVISION

1. Controlled Precipitation in Nuclear Materials

We have found that an almost ideal distribution of molybdenum results in samples prepared from nitrided, arc-melted alloys of uranium and molybdenum and that the solubility of molybdenum in UN is about 0.04 wt % at 2300°C. Additions of molybdenum at an 0.1 wt % level hold most promise for formation of very fine precipitate particles. The main problem encountered in the internally oxidized thorium-uranium nitride approach is obtaining optimum distribution of the admixed UO_2, which is used as the source of oxygen.

Boronation of thorium-zirconium solid-solution alloys by powder-metallurgy procedures has resulted in hot hardnesses far in excess of those reported for competitive alloys at temperatures to 800°C, where softening occurs abruptly. Studies using electron metallography, x-ray diffraction, and chemical analysis point to a solid-solution strengthening effect stemming from boron in combination with zirconium as being responsible for hardening. The analysis suggests that the softening tendency may be reduced by eliminating carbon, which is presently introduced by the preparation method.

2. Fuel Element Development

Thoria pellets for fabrication of irradiation specimens by thermochemical deposition have not been received; therefore, additional experiments were run to increase the efficiency of conversion of UF_6 to UO_2 powder. Experiments run in the last period on direct conversion of UF_6 to UN by reduction with lithium vapor in nitrogen show considerable difficulties in separation of the UN and the by-product LiF.

Deposition of tungsten-rhenium alloys as flat plate for mechanical properties testing is under way, and considerable data have been gathered to establish the low-temperature portion of the tungsten-rhenium phase diagram.

3. Nondestructive Test Development

We are developing new techniques and equipment for the nondestructive evaluation of materials and components. The major emphasis has been on eddy-current, ultrasonic, and penetrating radiation methods.

Our analytical work on electromagnetic phenomena has included a successful solution to the problem of a long encircling coil around a rod for several test variables and the beginning of a closed-form solution for a coil of any length and thickness above a conducting plane. Improvements to the phase-sensitive eddy-current instrument provide better temperature stability and use of longer lived batteries. New spacing probes have been developed which are more flexible, durable, and have longer signal cables allowing improved use in hot cells.

Further miniaturization and techniques development now allow us to fabricate and measure longitudinal notches on the inner surface of tubing with a bore as small as 0.055 in. With our Schlieren system we are now attempting to observe ultrasonic energy inside transparent solids.

A new solid-state, closed-circuit television system for use with the x-ray sensitive camera has been checked and shown to have improved resolution over the old system.

4. Zirconium Metallurgy

Three more lots of Zircaloy-2 tubing have been obtained from vendors. All were made from the same ingot stock, all were extruded, two were further worked by tube-reducing but by different schedules, and one was ball-swaged to size. All received the same total working and to the same final size. Examination of the basal pole figures by the Knoop microhardness method and visual examination with a polarized light microscope showed that the textures present in the three lots are widely different. This indicates the sensitivity of the final texture to details of the fabrication procedure. Quantitative determination of the basal pole figures as functions of position through the wall thickness is presently under way.

Tapered tube sections with complete die and mandrel profiles from six stages of tube reduction have been obtained from another vendor.

Detailed examination of the microtexture and texture gradients as functions of position in the reduction step is under way.

The information obtainable from the Knoop microhardness method of determining the "average" basal pole figure has been increased by an empirical correlation between one of the parameters determined in that method and data obtained from pole figures obtained by x-ray diffraction techniques. It is now possible to assign an intensity of basal pole concentration (times random) at the pole of each of the planes of the specimen on which the microhardness measurements are made. Thus, the utility of the method is considerably increased.

Variation of the cooling rate during precipitation of hydrides in elastically stressed Zircaloy-2 over the range of 4 to 170°C/min had no appreciable effect on the hydride pole figure. It did affect the morphology of the hydrides, those precipitated during fastest cooling being quite small and intragranular while those formed during slow cooling occurred in the grain boundaries and were much larger in size.

A rerun of a test in which a specimen was thermally cycled between 100 and 400°C twenty times while elastically stressed confirmed the earlier results which showed the hydrides were appreciably reoriented at 20 cycles but not at 5 and 10 cycles. A 100-cycle test is presently under way to determine if the reorientation of hydrides continues with increased number of thermal cycles.

Hydride pole figures have been determined for nine lots of Zircaloy-2 and Zircaloy-4 unstressed tubing. A correlation between concentration of hydride poles and basal poles at the same orientation point in the specimens was found to exist in tubing. No such correlation was found for plate and sheet Zircaloy-2. This correlation indicates that the hydride orientation in tubing may be sensitive to some fabrication variable that produced the observed crystallographic texture, but not to the texture itself.

Attempts to examine the texture in the shear zone of sheared polycrystalline specimens of zirconium by an x-ray diffraction method have shown that the equipment must be modified. An electrical-discharge cutting machine has been constructed for shaping the single-crystal

shear specimens to be used in the study of the magnitude of the shear stresses required to cause deformation systems in zirconium alloys to operate.

The "angle of rotation" of polarized light has been measured for a Zircaloy-2 single-crystal specimen as a function of basal pole tilt and wavelength of the illuminating light. These data now allow the microtexture and texture gradients in polycrystalline Zircaloy-2 and Zircaloy-4 to be determined by quantitative polarized light microscopy, with the pole figures being plotted on a polar chart directly from the microscope. The differences observed in the data for Zircaloy-2 and zirconium indicate the possibility of chemical analysis in binary zirconium alloys by measurement of some of the optical properties by microscopy.

Spectrophotometer studies of oxide films formed anodically on zirconium have shown that water is incorporated in the oxide film when the aqueous solution contains $K_2Cr_2O_7$, K_2CrO_4, and KNO_3; no foreign ions are incorporated in dilute KOH, $(NH_4)_3BO_3$, H_3BO_3, or Na_2MoO_4 solutions; and phosphate, lactate, citrate, and oxalate ions are incorporated when the solutions contain them. The carboxylate ions cause thinner films to be formed at any given anodizing voltage, higher electrical resistivities, and slower dissolution rates during vacuum annealing.

Accelerated oxidation has been observed on single-crystal zirconium plates at hydrides but only on certain slowly oxidizing planes. It occurs on both chemically and electrochemically polished specimens, and also seems to depend to some extent on the size of the hydride precipitates.

5. Sintered Aluminum Products Development

A program has been undertaken at ORNL directed toward developing processes, and, ultimately, specifications for the fabrication of aluminum-oxide-strengthened wrought aluminum products. Sintered aluminum products containing 2 to 10% oxide as a fine dispersion retain strength at high temperatures, thus making them attractive for 450°C

service as pressure tubes and fuel cladding in organic-cooled or desalination reactors.

We have approached the problem by thoroughly characterizing commercially available aluminum powder products and studying means for specific oxide additions. Fabrication and testing of the materials thus developed have shown that in comparison to previously available commercially sintered aluminum materials significant improvement of homogeneity and uniform strength properties may be attained.

Work on the characterization of commercially available powders is continuing. These powders are being used in experiments aimed at optimizing the ball-milling operation. A preferred ball-milling process has been chosen and steps are under way to scale it up from laboratory-size to 50-lb batches. Dispersion preparation by controlled oxidation of aluminum powders is also being investigated.

Extrusion billets of SAP are being made by a number of different procedures. A process flow sheet has been prepared for each. The suitability of each procedure is being evaluated by testing of the subsequent extrusions, with the objective of optimizing the consolidation step.

Product evaluation includes numerous techniques such as chemical analysis, x-ray diffraction, electron and light microscopy, mechanical properties, and nondestructive testing. Improved methods of chemical analysis and x-ray diffraction for identification of oxide species have been developed. Mechanical property testing continues to be the primary means of evaluating the extruded SAP product with electron microscopy used as an adjunct in analyzing the results. Excellent progress is being made on the development of a rapid nondestructive test for the determination of the dimensions of SAP flake material.

6. Weldability of Nickel-Bearing Alloys

A new program has been initiated to determine the effects of specific elements, individually and combined, upon the cracking behavior and mechanical properties of welds in nickel-bearing alloys. Much of the effort in this reporting period has been aimed at procuring high-purity raw materials and at fabricating special alloys for

testing both at Rensselaer Polytechnic Institute under subcontract and at ORNL. Commercial heats of Inconel 600, Incoloy 800, and Hastelloy X were weldability tested at Rensselaer using the VARESTRAINT test developed by them; the Inconel 600 exhibited the most overall hot-cracking resistance of the three materials with the other two alloys being pocrer, but roughly equivalent, in this respect.

A study has also been initiated to determine the influence of occasional small flaws upon the low-cycle fatigue properties of welds in nickel-bearing alloys. The results of preliminary tests in this investigation are reported.

PART II. REACTOR CHEMISTRY DIVISION

Fission-Gas Release and Physical Properties of Fuel Materials During Irradiation

A hollow-cylinder specimen of single-crystal UO_2 is being irradiated for the purpose of measuring thermal conductivity and fission-gas release during irradiation. In these experiments the specimen is oscillated sinusoidally in the reactor so as to oscillate the neutron flux and thus oscillate the fission rate in the specimen in a sinusoidal manner. The specimen temperature, measured by axial thermocouples, will also oscillate in response to the changing fission power. The base specimen temperature can be controlled by air cooling the outside of the specimen capsule.

The response of the specimen temperature will not be instantaneous with change of fission power, but will have a time lag depending on the specific heat, thermal conductivity, and emissivity of the specimen. The amplitude of the temperature oscillations will depend upon the amplitude of the fission-rate oscillations and the frequency of the oscillations. From measurements of phase shift and temperature amplitude as a function of frequency and amplitude of fission-rate oscillations, the thermal conductivity of the specimen can be calculated. By changing the base temperature and base fission rate, the thermal conductivity can be measured as a function of fission rate and temperature.

From these studies we find that thermal conductivity (at constant temperature) decreases when the fission rate in the specimen is increased. Increasing the temperature of the specimen (at constant fission rate) will increase the thermal conductivity by annealing some of the irradiation damage. The thermal conductivity during irradiation at elevated temperatures is apparently a balance between the creation and annihilation of defects in the UO_2 crystal structure.

The effect of electrical fields on UO_2 during irradiation was measured, and it was established that the feedback results were a property of the irradiated UO_2 rather than the specimen surroundings.

PART III. SOLID STATE DIVISION

Irradiation Effects on Alloys and Structural Materials

Our study of the response of weld heat-affected-zone samples of ASTM A-212, grade B, pressure-vessel steel is continuing and the latest results reported below reinforce the earlier observations that heat-affected-zone samples show a higher ductile-to-brittle transition temperature after irradiation and are less responsive to postirradiation annealing than baseplate specimens. Studies of the effect of neutron irradiation and postirradiation annealing on the tensile properties of this steel are reported and show that annealing of radiation hardening takes place in the temperature interval from 300 to 600°C.

Our section has been fortunate in having R. W. Armstrong from Brown University with us for the summer as a research participant with the Oak Ridge Associated Universities. He has contributed an analysis of the grain size dependence of the ductile-to-brittle transition temperature to this report. This analysis expresses the ductile-to-brittle transition temperature in terms of experimentally obtainable parameters and leads to the conclusion that the transition temperature should increase at an increasing rate with increases in yield stress due to radiation hardening.

An analysis of the stress-strain curves of Ferrovac-E specimens after neutron irradiation at temperatures between 55 and 90°C

has suggested that radiation hardening may be viewed as equivalent to strain hardening. Electron microscope examination of irradiated and strained Ferrovac-E specimens shows that dislocation tangles form at lower strains in the irradiated specimens than in the unirradiated specimens and that this early formation of tangles may be a consequence of dislocation channeling. These electron microscope observations also support the idea that radiation hardening is similar to strain hardening.

Our study of plastic deformation in niobium single crystals is continuing and progress is reported in several areas. The effect of specimen purity on the flow stress of niobium single crystals was studied using tensile specimens cut from rods given various numbers of zone refining passes. For niobium prepared from Wah Chang starting stock the lower yield shear stress dropped from 2.5 kg/mm^2 after 1 pass to 1.6 kg/mm^2 after 4 passes. Further numbers of passes up to 12 caused only a slight change in the flow stress. Similar effects were observed using Du Pont niobium starting material.

The effect of neutron irradiation on the plastic deformation of niobium single crystals is being studied. The increase in upper yield stress after neutron irradiation at about 90°C was found to be proportional to the one-fourth power of the neutron dose for doses in the range of 10^{15} to 10^{18} neutrons/cm^2. Studies of dislocation etch pits in irradiated niobium showed that the dislocation velocity is proportional to the tenth power of the applied shear stress. A comparison of these results with stress-strain curves of niobium irradiated to the same dose leads to the following conclusions:

1. The dislocation velocity at the upper yield point is about the same in both unirradiated niobium and irradiated niobium.

2. The dislocation velocity at the lower yield stress is a factor of 6 greater in irradiated niobium than in unirradiated niobium.

3. The mobile dislocation density at the lower yield stress is a factor of 6 less in the irradiated niobium than in the unirradiated niobium.

The interaction of interstitial impurity atoms in niobium with radiation produced defects is being studied using internal friction

measurements. Niobium containing oxygen, nitrogen, and carbon as interstitial impurities was irradiated at 50°C and then annealed. Internal friction measurements showed that upon warming the oxygen interstitials, which are the most mobile of the three species, migrate to radiation produced defects and are effectively removed from the normal lattice sites. It was concluded that this process is responsible for the stage III changes of resistivity and yield stress observed by previous investigators.

Progress toward completion of the design of a fission-flux neutron convertor irradiation facility is described.

[redacted]

PART I.

METALS AND CERAMICS DIVISION

[redacted]

[redacted]

1. CONTROLLED PRECIPITATION IN NUCLEAR MATERIALS

J. L. Scott J. P. Hammond

The purpose of this program is to develop means of improving the performance characteristics of both fissionable and nonfissionable materials by optimizing the microstructure through controlled precipitation of stable dispersed phases. Recent emphasis has been placed on uranium nitride and metallic thorium. Uranium nitride finds application in space nuclear reactors, and solid solutions of (Pu,U)N are long-range contenders for use in fast-breeder reactors. Thorium metal is of interest in desalination reactors and as a safety device in fast-breeder reactor cores when combined with plutonium. Fine precipitates in the microstructure of these fuels may enhance irradiation stability by pinning fission-gas bubbles, thereby preventing coalescence.

Production of Fine Precipitates in Uranium Nitride

T. G. Godfrey J. M. Leitnaker
R. A. Potter

A thermally stable dispersion of fine precipitate particles could greatly enhance the irradiation performance of fuels through provision of nucleation and pinning sites for fission gases. We are investigating several possible methods of producing such a dispersion in pressed-and-sintered uranium nitride.

The first method involves the addition of molybdenum, which is nonreactive chemically with UN, but slightly soluble at high temperature. Our current efforts are directed toward determining the temperature dependence of this solubility so that we may control the sintering and annealing conditions to produce a fine dispersion of molybdenum.

The second method involves controlled internal oxidation of a (U,Th)N solid solution to produce fine ThO_2 precipitates in the UN matrix. The oxygen is supplied by admixed UO_2, and present work is concerned with obtaining the optimum distribution of the UO_2 powder.

[redacted]

Molybdenum Additions

Our initial work with molybdenum in uranium nitride was done on specimens prepared from admixed powders.[1] The microstructure of UN containing 0.1 wt % Mo after sintering at 2335°C is shown in Fig. 1.1a; the distribution of molybdenum was not random and the particles were excessively large. In order to obtain a more homogeneous distribution, we arc melted uranium alloys containing 0.1, 0.5, and 1.0 wt % Mo and used these alloys for powder synthesis by the hydride-nitride process. The microstructures resulting from the 2335°C sintering, Figs. 1.1b and 1.2, showed a much improved distribution of the molybdenum phase. In Fig. 1.1b, the molybdenum phase in the nitrided U–0.1% Mo alloy is barely detectable, while in Fig. 1.2 it is more readily seen because of its greater concentration (0.5 and 1.0 wt % Mo). The etchant used on UN (lactic, nitric, and hydrofluoric acids) rapidly dissolves the molybdenum particles, but examination of areas before and after etching has shown that the molybdenum particles are randomly distributed throughout the UN matrix. As would be expected, a sizeable number of the molybdenum particles are located in grain boundaries, but the fact that many are located within the UN grains indicates that gross redistribution did not occur during sintering.

The effect of heat treatment on composition and lattice parameters of UN-molybdenum specimens prepared from the alloys is shown in Table 1.1. It is significant to note that the lattice parameters of the 0.1, 0.5, and 1.0 wt % Mo specimens are essentially the same after the 2335°C sintering treatment. Since some molybdenum is visible as a second phase in the 0.1 wt % sample, Fig. 1.1b, it is evident that the solubility of molybdenum in UN is less than 0.1 wt % under these conditions. Assuming the validity of Vegard's law for this dilute solution, we calculate that the maximum solubility of molybdenum in UN is 0.09 at. % or 0.035 wt % at 2300°C. In view of the approach used in arriving at this value, we recognize that it may be in error by as much as a factor of 3.

---

[1]T. G. Godfrey, J. M. Leitnaker, and R. A. Potter, Fuels and Materials Development Program Quart. Progr. Rept. June 30, 1966, ORNL-TM-1570, pp. 3–10.

[redacted]

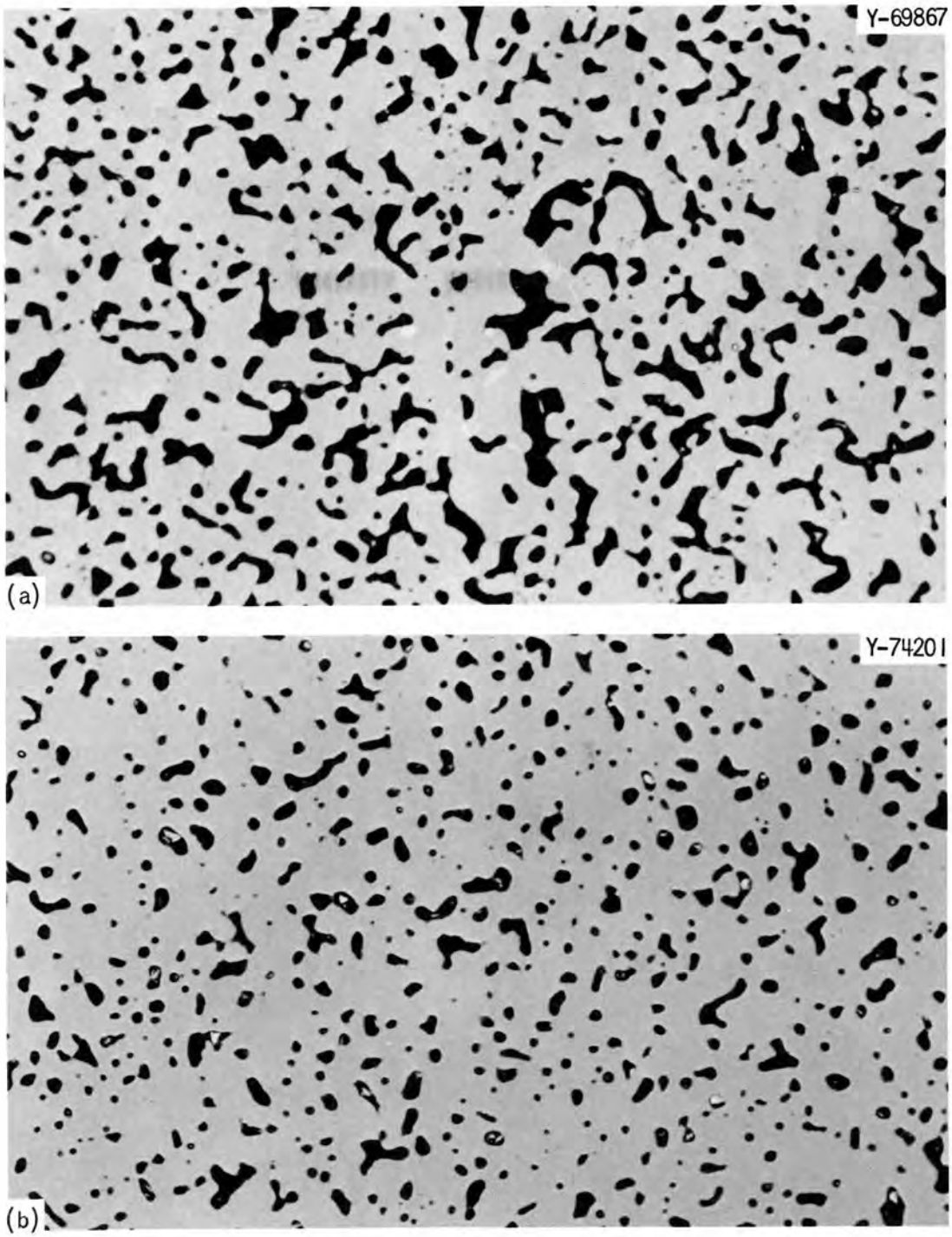

Fig. 1.1. Microstructures of UN Containing 0.1 wt % Mo after Sintering at 2335°C. As polished. 500×. (a) Prepared from admixed powders. Note nonrandom distribution of large molybdenum particles. (b) Prepared from arc-melted alloy. Bright areas in pores are primarily reflections, but some are metallic molybdenum particles. Small molybdenum particles in matrix are difficult to see.

[redacted]

[redacted]

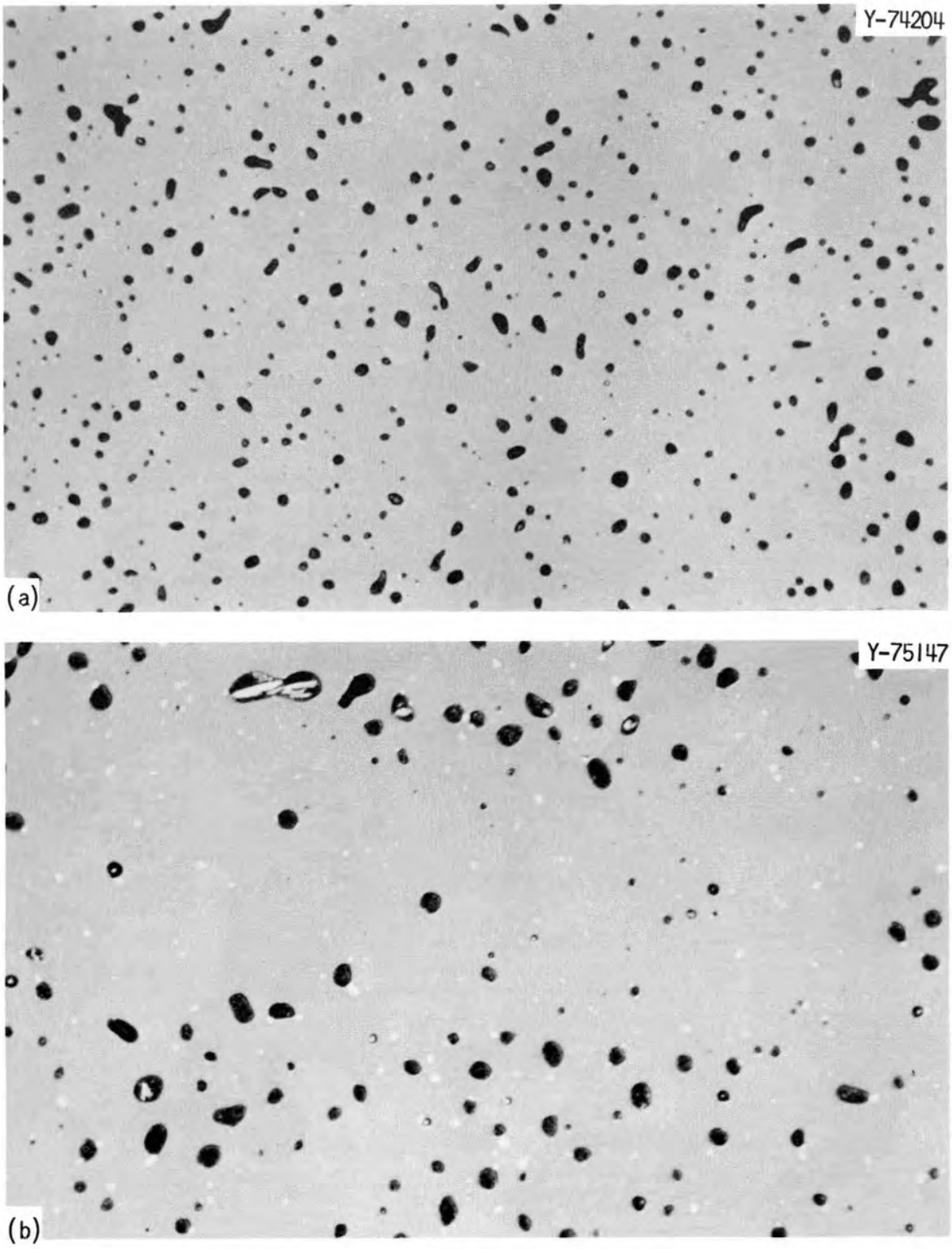

Fig. 1.2. Microstructures of UN Containing Molybdenum Prepared from Arc-Melted Alloys and Sintered at 2335°C. As polished. (a) 0.5 wt % Mo. 500×. (b) 1.0 wt % Mo. 750×.

[redacted]

Table 1.1. Effect of Heat Treatment on Lattice Parameter and Density of UN-Molybdenum Specimens

Nominal Composition (wt %)	Heat Treatment[a]	Actual Composition, wt %		Lattice Parameter[b] (A)	Density (% of Theoretical)
		O_2	Mo		
UN–0.1 Mo	Powder, 1800°C	0.074	0.10	4.8887	
	Sintered, 2335°C	0.088	0.11	4.8874	89.1
UN–0.5 Mo	Powder, 1800°C	0.051	0.55	4.8884	
	Sintered, 2335°C	0.134	0.48	4.8876	93.5
	Annealed 1 hr, 2300°C	c	0.48	4.8878	
	Annealed 1 hr, 2400°C	0.095	0.46	4.8879	
	Annealed 1 hr, 2500°C	0.102	0.46	4.8885	
	Annealed 1 hr, 2600°C	0.090	0.40	4.8891	
	Annealed 4 hr, 2000°C	0.310	0.49	4.8876	
	Annealed 8 hr, 1800°C	0.180	0.48	4.8878	
UN–1.0 Mo	Sintered, 2335°C	c	0.92	4.8878	95.5

[a]Sintering was done in tungsten-resistance furnace under 1 atm N_2 and annealing in induction furnace 2/3 under 2/3 atm N_2.

[b]Standard deviations were computed from a least-squares treatment of the Nelson-Riley extrapolation and were always less than 0.0002 A.

[c]Not reported.

The lattice parameters of sintered and heat-treated UN-molybdenum specimens, as shown in Fig. 1.3, indicate a marked change in solubility in the vicinity of 2350°C. The microstructure of the sample annealed at 2600°C, Fig. 1.4, suggests that three phases existed at this temperature: solid UN, U-Mo (liquid alloy), and molybdenum. (Though not apparent in the photomicrograph, close examination of the intergranular regions of Fig. 1.4 clearly shows the presence of two metallic phases. At 2500°C and below, no evidence of liquid phase was found in the microstructure; however, the amount would be very small and possibly would not be seen.) At 2/3 atm N_2 pressure and 2600°C, the free-energy change, ΔF_T, for the reaction

$$UN(s) = U(\ell) + 1/2\ N_2(g) \qquad (1)$$

is positive, since the reaction is not observed. However, the reaction

$$Mo(s) + x\ U(\ell) = (x\ U,Mo)(\ell,sol'n) \qquad (2)$$

has a negative free energy change. Reaction (2) plus x times reaction (1) yields

$$Mo(s) + x\ UN(s) = (x\ U,Mo)(\ell,sol'n) + x/2\ N_2(g) \qquad (3)$$

which is the reaction we believe explains the observations. Experimentally, the reaction has a positive free energy change below about 2350°C. For a particular value of x, the free energy change for reaction (2), and hence reaction (3), becomes more negative as the temperature increases and both reactions will proceed to the right. Eventually, one of the solid phases (which one depends on the relative amounts present) will disappear and a two-phase region will result.

The influence of the thermodynamic quantities on the extent of reaction (3) in this instance can be viewed in an alternative, but equivalent way. Reaction (3) will have a free energy change of zero at equilibrium in the temperature range of interest. The value of x

[redacted]

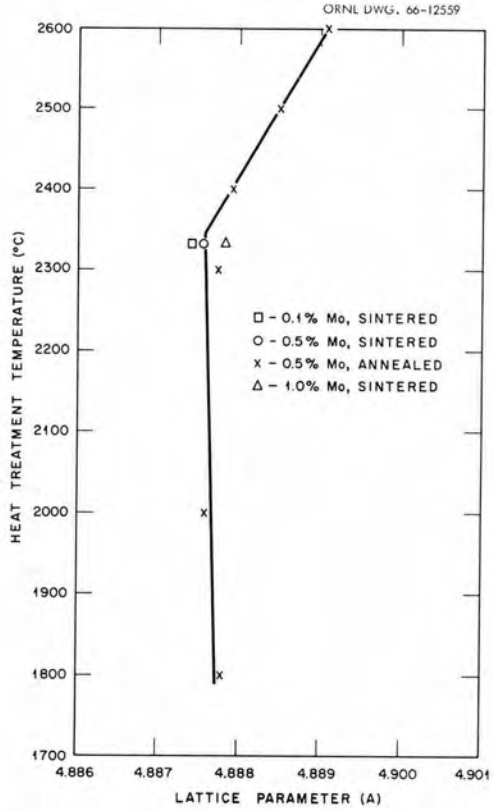

Fig. 1.3. Room-Temperature Lattice Parameters of UN-Mo Specimens, Prepared from Arc-Melted Alloy, as a Function of Heat Treatment.

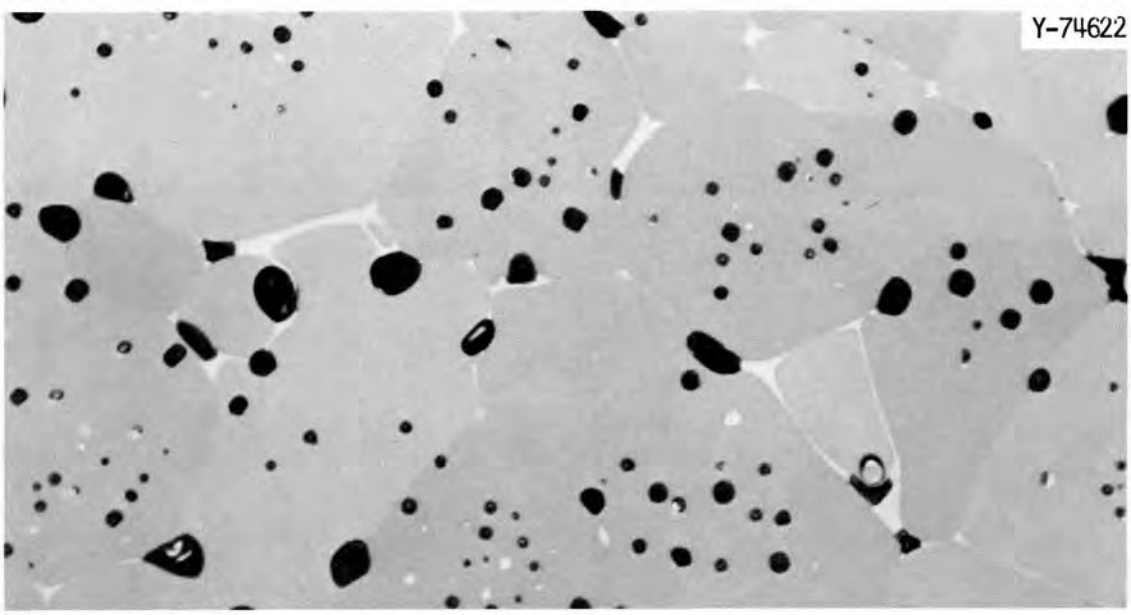

Fig. 1.4. Microstructure of UN–0.5 wt % Mo Specimen Annealed at 2600°C Under 2/3 atm N_2 Showing Evidence of Extensive Liquid-Phase Formation. As polished. 200×.

[redacted]

changes, however, in order to maintain the equilibrium value. Eventually the amount of molybdenum present is no longer sufficient to permit a three-phase equilibrium and all the molybdenum dissolves.

Further support for a liquid-phase formation or for an increased preliquid mobility is given by the density of as-sintered specimens of 0.1, 0.5, and 1.0 wt % Mo (Table 1.1). The density of these identically treated specimens markedly increased with molybdenum content at the sintering temperature of 2335°C.

It is unfortunate that the induction furnace used for the annealing experiments allowed the pickup of significant quantities of oxygen, particularly at the lower temperatures, as shown in Table 1.1. Microstructural examination of these samples annealed at the lower temperatures clearly showed the presence of an oxide phase, generally associated with pores. It is hoped that this problem of oxygen contamination can be corrected in the future.

We feel that we can obtain valuable phase information from further annealing experiments on the 0.5 and 1.0 wt % Mo specimens. However, from our results to date, it appears that 0.1 wt % Mo is about the proper concentration in terms of fine precipitate formation.

Thorium and Oxygen Additions

Further microstructural examination of the (U,Th)N alloy specimens, to which carbon and oxygen additions had been made in the form of graphite flour and UO_2 as previously described,[2] has shown that we must improve our starting materials and techniques if we are to understand the U-Th-N-O-C system. Clear evidence of this is presented in Fig. 1.5, which shows the very nonuniform distribution of the oxide phase. In these preliminary experiments, the (U,Th)N powder was prepared by the hydride-nitride process and given a 2000°C final treatment to reduce

---

[2]T. G. Godfrey, J. M. Leitnaker, and R. A. Potter, Fuels and Materials Development Program Quart. Progr. Rept. June 30, 1966, ORNL-TM-1570, pp. 3–10.

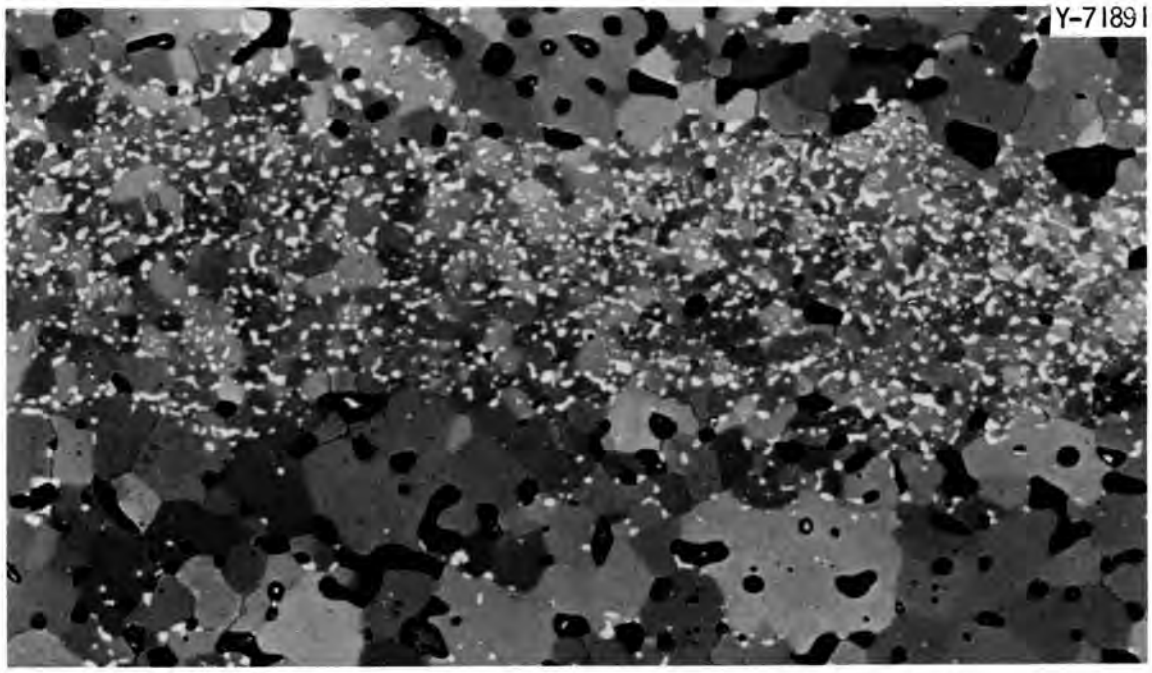

Fig. 1.5. Microstructure of 97% UN–3% ThN with 2 1/2 wt % UO_2, Sintered at 2335°C, Showing Nonuniform Distribution of White Oxide Phase. Etchant: 30 parts lactic acid, 10 parts HNO_3, and 1 part HF. 500×.

the surface area of the powder. This treatment coarsened the powder and caused the subsequent wet mixing of the alloy powder and the UO_2 to yield a nonhomogeneous powder. Figure 1.6 also shows nonuniform distribution of the oxide phase and a number of metallic inclusions which were identified by microprobe analysis to be principally Fe, Ni, and Cr. The origin of these inclusions is unknown.

In order to overcome the purity and mixing problems described above, we have altered our synthesis scheme to yield a finer powder that should lead to better mixing and are using arc-melted uranium-thorium alloys prepared from high-purity (< 300 ppm impurities) metal. We will try several different ways of mixing the nitride and oxide powders in order to determine the procedure leading to proper dispersion and minimum contamination. Sintering and heat-treating studies on these homogeneous specimens should lead to a clearer understanding of how UO_2 reacts with (U,Th)N and the conditions necessary for the production of a dispersion of fine precipitate particles through internal oxidation.

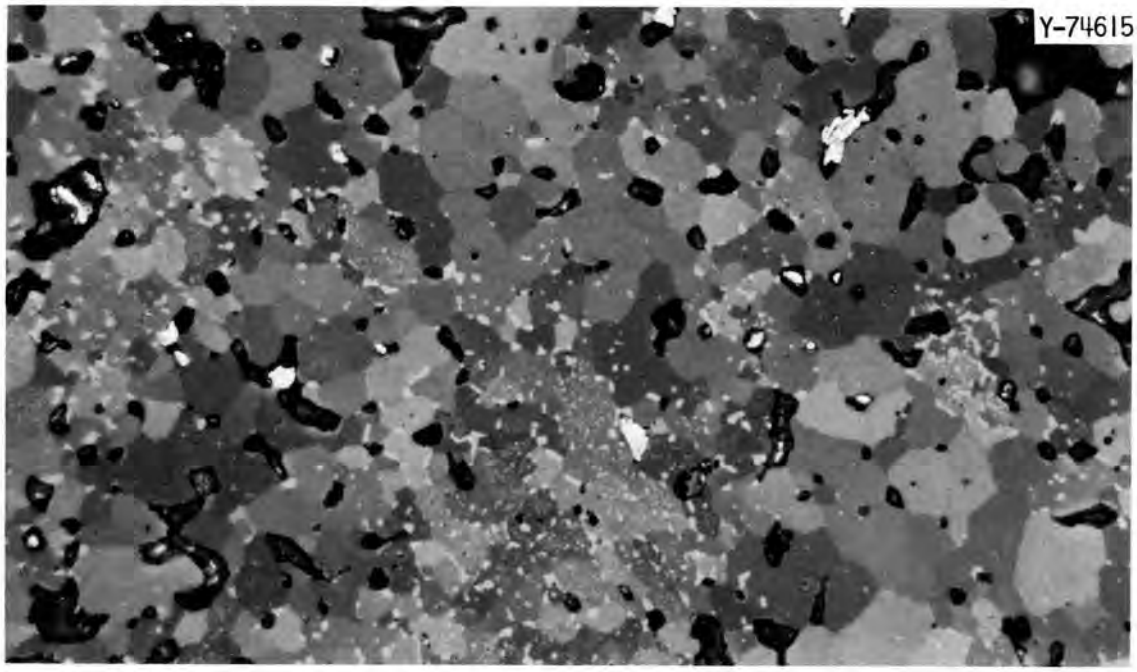

Fig. 1.6. Microstructure of 95% UN–5% ThN with 5 wt % UO_2, Sintered at 2335°C, Showing Nonuniform Distribution of White Oxide Phase and Metallic Inclusions. Etchant: 30 parts lactic acid, 10 parts HNO_3, and 1 part HF. 200×.

Controlled Precipitation in Thorium Alloys

J. P. Hammond

Studies to dispersion strengthen thorium for potential use as a fuel matrix material were continued. The results of hot-hardness tests were previously reported[3] for thorium-rich thorium-zirconium solid-solution alloys hardened by internal boronation and for thorium dispersion hardened with ThO_2 by the particle embedment technique. Both materials were fabricated by powder metallurgy procedures. Thorium metal or alloy was made ultrafine by high-energy impact ball-milling as hydride using hexane as a lubricant. This was followed by dehydriding and then kneading the additive (boron or ThO_2) in the metal or alloy powder by

[3]J. P. Hammond, Fuels and Materials Development Program Quart. Progr. Rept. March 31, 1966, ORNL-TM-1500, pp. 5–7.

further ball-milling in hexane before finally consolidating and extruding into bar. Material hardened with boron, where the aim was to dispersion harden by producing an ultrafine precipitate of ZrB_2, gave hardnesses in the 600 to 800°C temperature range twice as high as had been obtained on competitive alloys,[4] but further work was needed to refine and explain the process. The ThO_2 embedment method, on the other hand, gave conspicuously low hot hardnesses in spite of the fact that the high-energy milling process was used to obtain the finest possible dispersions.

Chemical analyses and metallography of these alloys have revealed an unexpected high level of carbon (approximately 1 3/4% for the boronated alloys). This was attributed to a pickup of carbon from the hexane used in the double-milling procedure and indicates the high reactivity of finely divided thorium with this lubricant. Techniques were then altered to confine the ball-milling to powders in their presumably less active, hydride state. Further modifications, designed to improve the distribution of additive, consisted of substituting boron soot measuring 200 A in mean particle size for the coarser, commercial grade of boron and reducing its amount.

A summary of the hot-hardness results for these alloys is given in Table 1.2. Data for unalloyed thorium and a cast Th–5% Zr alloy, shown to be the most attractive arc-cast alloy in earlier work,[4] are included for comparison.

Specimen 3 of this table, corresponding to 70 Th–10 Zr–20 B (at. %), represents the earliest attempt to harden thorium by boronation. In spite of the fact that boron was introduced at a level appropriate to form diboride of all the zirconium present, this specimen exhibited the lowest hot hardness. The microstructure showed severe segregation of the boron which no doubt resulted from the coarseness of the boron and the inferior milling process used.

---

[4]J. A. Burka and J. P. Hammond, Evaluation of Thorium-Base Alloys for High-Temperature Strength, ORNL-3777 (April 1965).

[redacted]

Table 1.2. Hot Hardness of Dispersion-Hardened Thorium Alloys

Specimen Number	Method of Hardening	Composition (wt %)	Size and Type of Dispersant	Post-Extrusion Anneal	Chemical Analysis, wt%			Hot Hardness[a] (DPHN) at				
					B	C	O	25°C	500°C	600°C	700°C	800°C
1[b]	None	Thorium		None				85	30	22	15	ND
2[c]	Alloying	Th–5 Zr		None				104	71	60	42	ND
3[d]	Boronation	Th–4.65 Zr–1 B	–200 μ B	None				126	69	49	40	28
4[e]	Boronation	Th–4.65 Zr–0.54 B	–400 μ B	None	0.37	1.79	0.79	494	208	120	81	61
5[e]	Boronation	Th–4.65 Zr–0.27 B	–400 μ B	None	0.21	1.82	0.68	419	139	89.5	54	39.5
6[f]	Boronation	Th–4.65 Zr–0.54 B	0.02 μ B	None	0.43			427	129.5	92	70.5	64.5
7[f]	Boronation	Th–4.65 Zr–0.14 B	0.02 μ B	None	0.15	0.91	0.53	403	152	94	62	53
8[f]	Boronation	Th–4.65 Zr–0.14 B	0.02 μ B	100 hr, 750°C				414	157	87	58	53
9[f]	Boronation	Th–4.65 Zr–0.14 B	0.02 μ B	100 hr, 850°C				324	148	71	33	23
10[g]	(Carburization)	Th–4.65 Zr		None		0.77		280	88	33	16	10
11[h]	ThO_2 embedment	Th–5 ThO_2	0.04 μ ThO_2	None				123	53	41	29	21
12[h]	ThO_2 embedment	Th–5 ThO_2	0.04 μ ThO_2	None		0.14		220	91	63	43	31
13[i]	ThO_2 embedment	Th–5 ThO_2	0.04 μ ThO_2	None				326	126.5	68.5	23	7
14[i]	ThO_2 embedment	Th–10 ThO_2	0.04 μ ThO_2	None		1.05		296	91.5	60.5	21.5	5.5

[a]Values reported represent average of two measurements.

[b]Chemical analysis: 99.8% Th, 340 ppm C, 2000 ppm O, and 180 ppm N.

[c]Thorium has same chemical content as that used in specimen 1 and was prepared by arc casting.

[d]Thorium same as in specimen 1; prepared from –325 mesh powder of hydrided and dehydrided Th–4.65% Zr alloy and 1.1% commercial boron powder by ball-milling dry for 3 hr, hot pressing at 1000°C, and extruding at 750°C.

[e]Thorium same as in specimen 1; prepared by hydriding Th–4.65% Zr alloy, ball-milling in hexane 24 hr, dehydriding, introducing 0.54% commercial boron refined by ball-milling 24 hr, again ball-milling in hexane 24 hr, cold pressing, vacuum sintering 3 hr at 800°C, and extruding at 750°C. Milling steps were performed in high-energy impact mill.

[f]Same as specimen 5 but substituting 0.02 μ-size boron soot (produced from B_2H_6 by thermal decomposition) for the coarser commercial grade, and replacing the final hexane – milling operation (performed with thorium in metallic state) with a 3-hr dry blending step to limit carbon pickup.

[g]Thorium same as in specimen 1; prepared by simply ball-milling hydrided Th–4.65% Zr alloy 24 hr in hexane, dehydriding, cold pressing, vacuum sintering 3 hr at 800°C, and extruding at 750°C. Milling was with high-energy impact mill.

[h]Thorium same as in specimen 1; prepared by dry milling hydrided thorium and ultrafine, "Vitro" ThO_2 for 24 days in an ordinary low-energy mill, vacuum hot pressing at 1000°C, and extruding at 900°C.

[i]Thorium same as in specimen 1; prepared by ball-milling hydrided thorium and ultrafine "Vitro" ThO_2 in hexane 24 hr, dehydriding, cold pressing, vacuum sintering 3 hr at 800°C, and extruding at 750°C. Milling steps were performed in high-energy impact mill.

[redacted]

Specimens 4 and 5 were prepared using the double-milling process whereas 6 and 7 were prepared by the method using once-milling on powder as hydride and subsequent introduction of boron as soot. Elevated-temperature hardness appears to be significantly improved and at a lower level of boron as a result of modifying the process. Metallographic examination of these specimens revealed a precipitate-free matrix with a coarse (1 to 2 1/2-μ diam) secondary constituent, present in amounts of about 8 to 12 vol % in specimens 4 and 5 and 2 to 4 vol % in specimens 6 and 7.

Annealing experiments were performed on the material with lowest boron content (specimen 7) to determine the effect of high-temperature aging on retention of hot hardness. Annealing for 100 hr at 750°C produced virtually no softening (specimen 8); whereas, annealing for this period at 850°C gave a hardness at 800°C less than one-half the former value. Twenty-four hour anneals at 800°C were conducted on specimens 4 and 5, resulting in only a small reduction in hardness at 800°C. Thus, it is clear that for these alloys high hardness persists to around 800°C, where softening occurs quite abruptly.

When it was discovered that large amounts of carbon were picked up during milling, a specimen (specimen 10 of Table 1.2) was processed without the addition of boron to establish whether or not carbon, in conjunction with zirconium, produces hardening in thorium. It is to be noted that the hardness of specimen 10 at 700 and 800°C is slightly higher than that of unalloyed thorium.

Specimens 11 through 14 illustrate the detrimental effect of carbon contamination when dispersion hardening thorium with ThO_2. Although specimens 11 and 12 were processed by an inferior, dry ball-milling method, the hot hardnesses obtained were far superior to those achieved with the high-energy process which introduces carbon from the hexane lubricant. Carbon analyzed 1.05% for the latter process (specimen 14) but only 0.14% for the former (specimen 12).

An examination of the chemical analyses listed in Table 1.2 for the boronated alloys shows that boron is largely retained during

processing. For once-milling with thorium in the hydride state, the carbon content was approximately 1% (specimens 7 and 10) compared to about 1.75% for the twice-milling procedure (specimens 4 and 5). Oxygen, except for intentional addition as ThO_2, may range from about 0.5% (specimen 7) to approximately 0.75% (specimens 4 and 5). In consideration of the solubility limits of these elements in thorium, ThC and ThO_2 would be expected to be the chief secondary phases in these alloys. The solubility of carbon in thorium at room temperature is variously reported between 0.2 and 0.35%, oxygen is very insoluble, and boron is soluble to an unspecified amount.[5] An x-ray diffraction examination of specimen 7, discussed further below, showed ThC and ThO_2 as sole secondary phases.

A diffractogram taken of specimen 7 disclosed alpha thorium with weak spectra of ThC and ThO_2. The lines for thorium were shifted and very diffuse, indicating an expansion and considerable strain in its crystal lattice. After annealing at 850°C (specimen 9), little change was noted except for a sharpening and definite intensification of the thorium spectrum.

We had expected that with the marked hardening exhibited in these alloys at high temperature that dispersion hardening would contribute to strengthening. However, repeated electron metallographic examination by the replication technique failed to disclose any evidence of an ultrafine dispersion. Figure 1.7 shows electron micrographs for the 0.14% B-containing material as extruded (specimen 7) and after annealing at 850°C (specimen 9). The massive particles in the micrograph, Fig. 1.7a, present at about 3 vol %, would appear to be ThC based upon a correlation between chemical analyses and variations in amounts of the phase between samples. The microstructure in Fig. 1.7b, instead of showing a coalescence of a matrix precipitate as normally accompanies overaging, displayed an unexpected behavior involving the coarse

---

[5]F. A. Rough and Arthur A. Bauer, Constitution of Uranium and Thorium Alloys, BMI-1300 (June 1958).

[redacted]

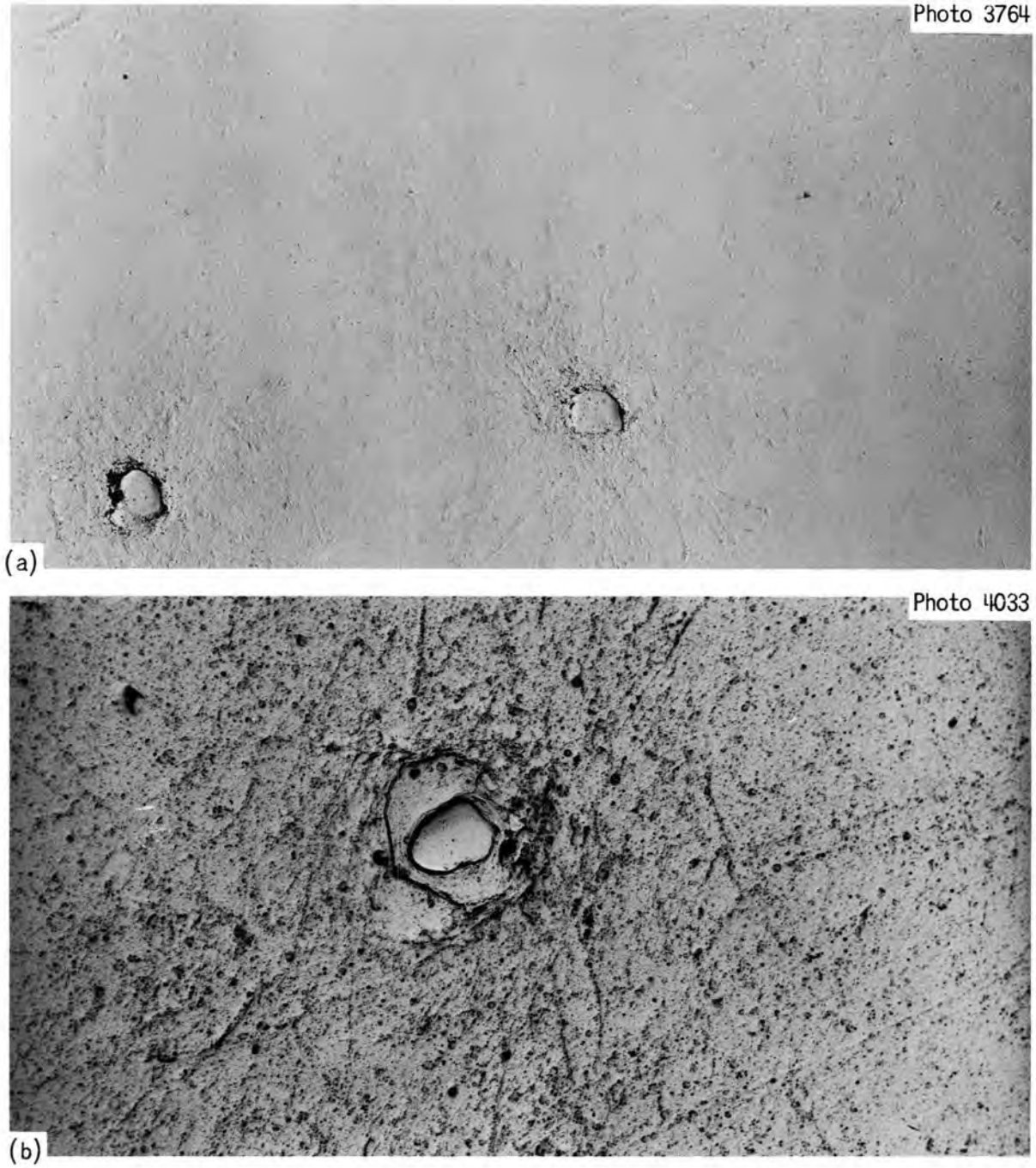

Fig. 1.7. Electron Micrograph of Th–4.65% Zr–0.14% B Alloy. (a) Sintered at 800°C and extruded at 750°C. 6000×. (b) Same but subsequently annealed 100 hr at 850°C. 9000×. The peppery material on the particles in (a) and seen rather generally in (b) is foreign matter. Note the disturbed region around particles in (a) and an advanced stage of this in (b). Two-stage plastic carbon replication.

[redacted]

ThC particles. A dissolution effect appears to be occurring in areas surrounding the carbide particles. The incipient stage of this is seen in this material in its as-extruded form (Fig. 1.7a).

From the preliminary information at hand, we believe that the hardening of these thorium alloys results essentially from solid-solution strengthening by boron in combination with zirconium. Thermodynamic data indicate that boron in preference to carbon would associate with zirconium while oxygen combines with thorium.[6] We suggest that the pronounced softening occurs as a result of a sudden dissolution of zirconium and boron into the ThC particles, precluding the formation of an otherwise fine precipitate of ZrB_2. Facts concerning phase equilibria that support this hypothesis are discussed below.

The zirconium-boron phase diagram by Glaser and Post[7] shows one compound, ZrB_2, below 800°C but from 800 to 1250°C ZrB coexists with ZrB_2. Samsonov and cohorts[6] have shown that whereas the system ZrB_2-ZrC is a mixture of two phases with no significant solubilities of one phase in the other, ZrB and ZrC form a continuous series of solid solutions. If ThC acts like ZrC, which would not be unexpected since they are structurally analogous phases, this suggests that at temperatures below 800°C any ZrB_2 of the thorium alloys would be compatible with the ThC phase; but at higher temperatures ZrB would begin to form and immediately dissolve in the ThC.

Future experiments are planned to further test this explanation. In some samples, carbon will be kept low by performing the ball-milling dry so as to preclude ThC and any accompanying dissolution softening. The boron soot shows indications of serving as an inhibitor to particle seizure and mass agglomeration, an ever-present problem when grinding thorium, even as hydride, under the conditions of high-energy impaction.

---

[6]G. V. Samsonov *et al.*, Boron, Its Compounds and Alloys, AEC-tr-5032 (Book 2) (1960), p. 542.

[7]F. W. Glaser and B. Post, "System Zirconium-Boron," Trans. AIME 197, 1117–18 (1953).

2. FUEL ELEMENT DEVELOPMENT

G. M. Adamson, Jr.

Our studies in the process of thermochemical deposition as a means of fabricating refractory fuels and refractory-metal cladding are continuing. Specimens of TCD UO_2 for irradiation experiments are being prepared in two forms: UO_2-coated thoria pellets and UO_2 pellets prepared from powder.

The evaluation of the process for thermochemical reduction of PuF_6 to PuO_2 is awaiting the completion of an experimental apparatus.

Experiments in lithium reduction of UF_6 in the presence of nitrogen to obtain UN indicate feasibility of the reaction. Inability to obtain clean separation of the UN and the by-product LiF remains a problem area.

We have deposited tungsten-rhenium alloys having compositions with nominally 5, 25, and 90 wt % Re. Our technique is very successful for alloys containing up to 25% Re but grown-in porosity is found with rhenium-rich deposits.

Deposition of Uranium Dioxide by Hydroreduction of Uranium Hexafluoride

R. L. Heestand W. R. Martin

Two types of specimens are being prepared to evaluate the irradiation behavior of UO_2 produced by direct thermochemical reduction of UF_6. Fully enriched UF_6 was obtained for deposition of theoretically dense coatings on thoria pellets, and 2.5% enriched UF_6 was obtained for conversion to powder for fabricating pressed-and-sintered pellet specimens. Metallographic examination of thoria pellets coated with solid UO_2 shows good adhesion of the two oxides; however, cracks were found originating in the thoria, which propagate through the UO_2. Large variations in density of the thoria pellets were found, which might contribute to the cracking problem; therefore, a new batch of thoria pellets was ordered. These have not been obtained.

Experiments in powder preparation were continued to increase the yield of usable material. Since the apparatus for deposition was built

to demonstrate chemical feasibility and not necessarily to produce material, only 40% of the feed material was recovered as usable powder for further experiments. Without significant changes in the apparatus we have increased UF_6 feed rate by 50% and UO_2 powder recovery to above 75%.

Since sufficient material for preparation of pressed-and-sintered pellets may be produced at this efficiency, we have proceeded with processing 2.5% enriched material.

Preparation of PuO_2 Powder from PuF_6 by Thermochemical Reduction

R. L. Heestand W. C. Robinson, Jr.

Completion and checkout of the experimental apparatus for conversion of PuF_4 to PuO_2 have been held up due to insufficient craft support. Work is scheduled to be completed early in the next quarter.

Deposition of Uranium Compounds by Lithium Vapor Reduction of UF_6

W. C. Robinson, Jr. W. R. Martin

Previously, nitrogen gas was introduced into a heated chamber containing a mixture of UF_6 and lithium vapor. Lithium vapor had already been shown to reduce UF_6 according to the reaction

$$UF_{6(g)} + 6Li_{(g)} \rightarrow U_{(s)} + 6LiF_{(g)} \ .$$

When the nitrogen gas was introduced, the resulting solid deposits contained UN, UN_2, various lithium-uranium compounds including $Li_7U_6F_{31}$ and Li_3UF_7, LiF, and some uranium metal. A powder pattern of two typically crushed deposits is shown in Table 2.1.

Attempts were made to separate the UN solid product from these contaminants by heating the reaction chamber under vacuum to a temperature sufficient to remove all of the other compounds from the deposit. This was not successful for two reasons. The first reason was that the UF_6 and lithium vapor reacted in a low-temperature region of the chamber. To overcome this, the UF_6 injector was lengthened and the

Table 2.1. Reaction Products of UF_6-Lithium-Nitrogen Gas Reaction

Run Number	Phase Observed	Intensity[a]
13-2	UN	S+
	αU	M+
	LiF	M+
	$Li_7U_6F_{31}$	M–
20-1	UN	S+
	LiF	S
	αU	M+
	$Li_7U_6F_{31}$	M–
	Unknown phase	M

[a]Legend: S = strong, M = medium, and W = weak.

UF_6 shielded with argon so as to allow it to pass into the center of the reaction zone before it encountered the lithium vapor. A purer product was obtained with the UN being the strongest phase in the resulting powder patterns, but the LiF and lithium uranium compounds were never reduced to below the detection of x-ray analysis. Secondly, to attempt a separation the temperature of the reaction chamber was continually raised to obtain a purer solid nitride powder until the limit of the chamber material was reached, and it failed during an experiment. This method was discontinued. A new apparatus was constructed and attempts were made to produce UN powder. In order to obtain better contact between the UF_6 stream and the lithium vapor, the UF_6 was injected into the chamber just above the lithium container. Unfortunately the injector consistently plugged in 1/2 to 1 1/2 hr in each experiment and very little powder was obtained. To produce a sufficient quantity of UN powder for evaluation it is apparent that a considerable amount of engineering would be necessary. Problem areas remaining are to control a measured flow of lithium vapor into a heated chamber and to construct a reaction chamber capable of at least

1500°C for extended periods. It was finally decided that an expensive and time-consuming effort to optimize the process after feasibility was established was not in accordance with the purpose of this work. However, if one could find an easily handled material that was a strong enough reducing agent to reduce UF_6 to uranium metal in the presence of nitrogen gas, the problem of trying to control a measured flow of lithium would be eliminated. This would drastically reduce the engineering problem and perhaps, with the aid of a series of baffles in the reaction zone, a reasonably pure UN powder could still be prepared. There is a possibility that this can be done by contacting UF_6 gas with $Li\text{-}NH_2$ vapor. Further work will concentrate on this reaction.

A short topical report will be written on the feasibility of producing UN from the simultaneous reaction of UF_6, nitrogen, and lithium vapor.

Deposition of Tungsten Alloys

J. I. Federer W. R. Martin

A method for depositing tungsten-rhenium alloy tubing having uniform composition in both the axial and radial directions has been previously discussed.[1] A water-cooled injector delivers the WF_6ReF_6 mixture directly into the heated zone of a mandrel where hydrogen reduction of the fluorides to metal occurs. The mandrel moves at a steady rate relative to the injector, continually furnishing new surface for deposition. The microstructure of alloys prepared to evaluate the technique are shown in Fig. 2.1. The deposit containing nominally 7% Re had a broken columnar grain structure (see Fig. 2.1a), that containing about 22% Re had a columnar structure (Fig. 2.1b), and that containing about 90% Re had a columnar or nodular structure with much grown-in porosity (Fig. 2.1c). There is very little microstructural evidence of compositional variations through the thickness of the

[1]J. I. Federer and C. F. Leitten, Jr., Fuels and Materials Development Program Quart. Progr. Rept. June 30, 1966, ORNL-TM-1570, pp. 11–13.

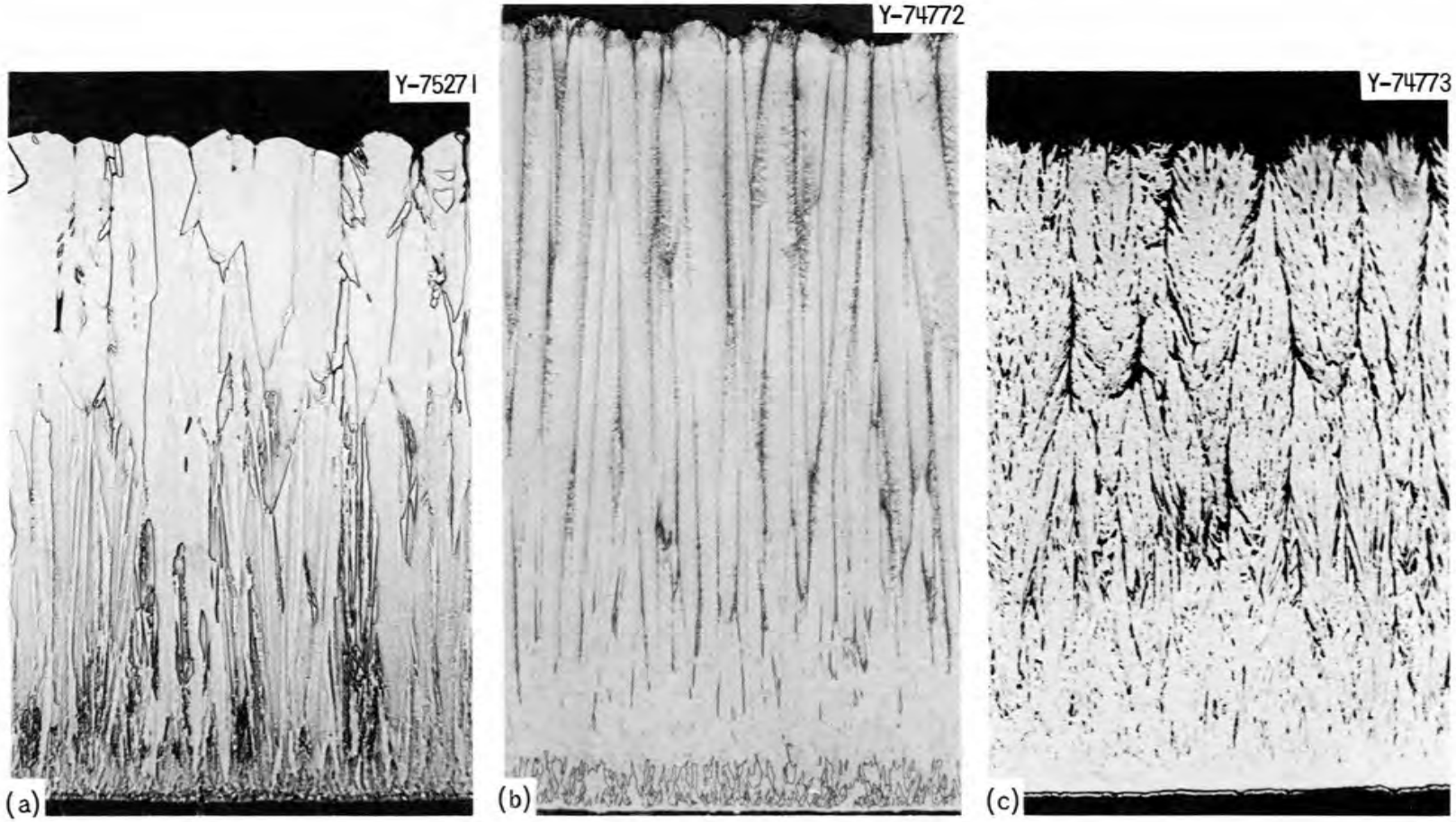

Fig. 2.1. Tungsten-Rhenium Alloys Deposited Using a WF_6-ReF_6 Injector in a Moving Hot Zone. (a) W–7% Re deposited at 800°C. Etchant: 50 NH_4OH (concd)–50 H_2O_2 (30%). 200×. (b) W–22% Re deposited at 900°C. Etchant: 50 NH_4OH (concd)–50 H_2O_2 (30%). 200×. (c) W–90% Re deposited at 900°C. As polished. 250×.

deposits shown in Fig. 2.1, as has been observed previously in deposits prepared without a WF_6-ReF_6 injector.[2] The axial variation in rhenium content was about ±0.5, ±1, and ±2% Re for nominal 5, 25, and 90% Re alloys, respectively. Metal recoveries approached 100%.

The results of these experiments indicated that the technique was suitable for deposition of alloys containing up to 25% Re and that grown-in porosity was a serious problem in rhenium-rich deposits. The next task was to prepare a sufficient amount of flat stock of approximately 5 and 25% Re alloys for mechanical properties evaluation by depositing the alloys on a mandrel having flat rather than tubular surfaces. First attempts to deposit flat stock utilized mandrels of square cross section (3/4 × 3/4 in.) prepared from 0.005-in.-thick molybdenum sheet. These mandrels, however, did not have sufficient structural strength to withstand deformation during handling, assembly into the deposition apparatus, and stresses due to differences in thermal contraction upon cooling from the deposition temperature. The deposits, therefore, were not suitable for preparation of specimens by grinding. Subsequently, five-sided mandrels were fabricated from 0.05-in.-thick low-carbon steel sheet. Each flat side of the mandrels measured about 3/4 in. wide and 18 in. long. The mandrels were supported inside nickel tubes for deposition at 750°C and in silica glass tubes for deposition at 900°C.

The following conditions were used to deposit an alloy containing about 6% Re: 750°C, 5 torr, 1000, 50, and 3 cm^3/min of H_2, WF_6, and ReF_6, respectively, and a mandrel travel rate of 0.9 in./hr. The deposit had a maximum thickness of about 0.04 in. along the longitudinal center line of the mandrel flats and was about half as thick in the corners. Specimens of desired thickness could not be obtained from this material; for example, bend specimens measuring 3/8 × 0.04 × 2 in. In a subsequent attempt to increase the deposit thickness, the gas flow

---

[2]J. I. Federer and C. F. Leitten, Jr., Fuels and Materials Development Program Quart. Progr. Rept. March 31, 1966, ORNL-TM-1500, pp. 14–18.

rates were doubled, other conditions being the same as in the previous experiment. Under these conditions a very rough, nodular deposit was obtained. The next attempt used the initial deposition conditions except that the mandrel travel rate was decreased to 0.45 in./hr. The maximum thickness in this case was about 0.1 in. The deposit contained an average 6.3% Re over a 7-in. length, and about 6.1% Re in the section from which specimens are being obtained. A cross-sectional view and the microstructure of the deposit are shown in Fig. 2.2. The thickness variation that can be observed in Fig. 2.2a is tentatively attributed to gas flow characteristics and can be minimized by increasing the number of flat surfaces (i.e., approximate a circle in mandrel cross section). The microstructure shown in Fig. 2.2b is columnar but exhibits a change in grain structure and contains a small amount of porosity. Compositional variations across the thickness of the deposit are being examined by means of the electron probe analyzer. Meanwhile, additional experiments are being conducted to deposit sufficient quantities of flat stock of both 5 and 25% Re alloys.

An investigation of the formation tendency and physical characteristics of the β-tungsten structure in tungsten-rhenium alloys is being conducted. Previous studies revealed two phases in alloys deposited at 500 to 750°C, a body-centered cubic solid solution of rhenium in tungsten coexisting with a cubic β-tungsten structure over the range 10 to 25% Re (ref. 3). Hardness increases up to 2000 DPH are associated with the β-tungsten structure; therefore, a knowledge of the conditions of occurrence and characteristics of the phase are needed. The temperature and compositional limits for formation of the phase are now being studied — in effect, determination of a portion of the phase diagram. X-ray diffraction is being used to identify and measure the lattice parameters of phases present in alloys containing up to about 40% Re that were deposited at a series of temperatures beginning at 800°C. Hardness values are being obtained, and the thermal stability

---

[3]J. I. Federer and C. F. Leitten, Jr., Fuels and Materials Development Program Quart. Progr. Rept. Dec. 31, 1964, ORNL-TM-1000, pp. 9,10.

[redacted]

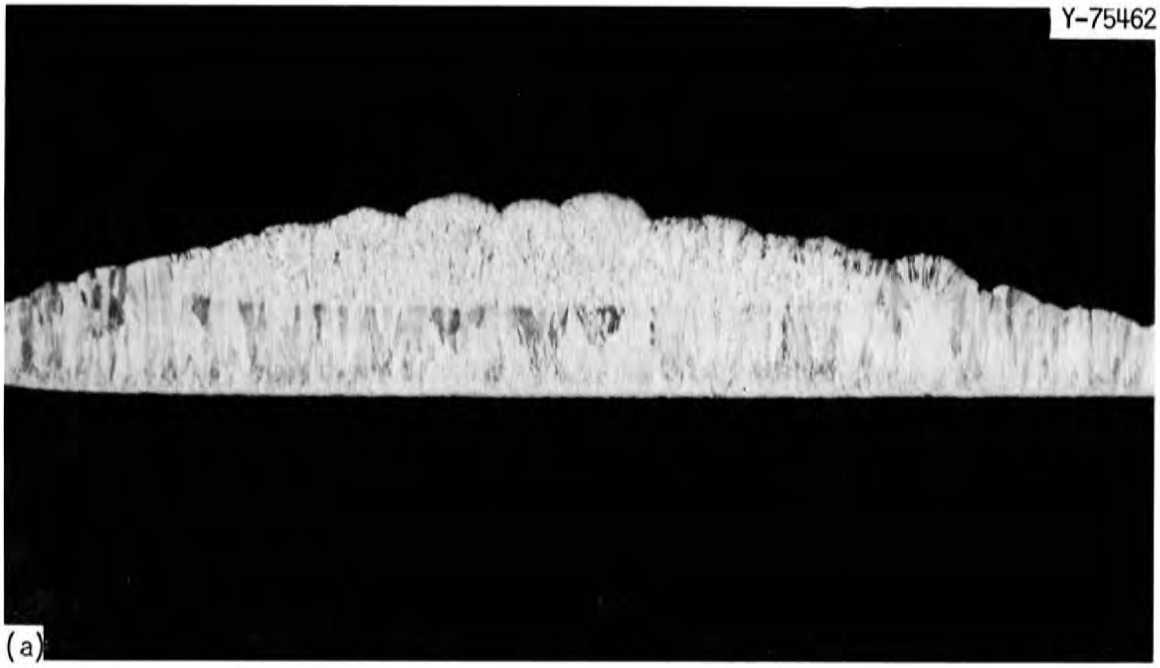

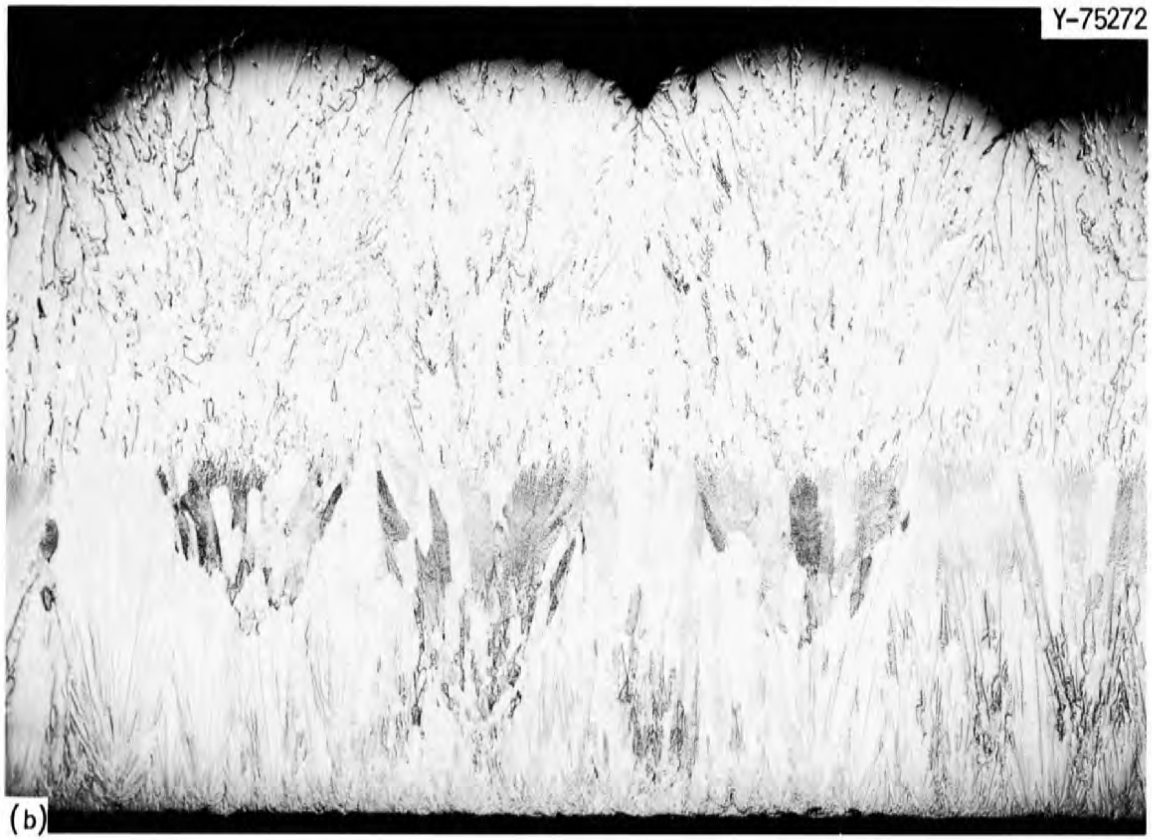

Fig. 2.2. Flat Stock of W–6% Re. Etchant: 50 NH_4OH (concd)–50 H_2O_2 (30%). (a) Showing thickness variation in a cross section of the deposit. 5×. (b) Microstructure of deposit showing change in grain structure. 50×.

[redacted]

of the as-deposited structures are being studied in a series of isothermal anneals.

The principal results obtained on as-deposited alloys are shown in Table 2.2. These results indicate that the occurrence of phases is both temperature and composition dependent, but insufficient data exist to establish phase boundaries. Lattice parameter shifts as a function of composition occurred in both phases. Additional specimens are being analyzed in order to resolve inconsistencies and to complete the survey of temperature and compositions.

[redacted]

Table 2.2. Phases Occurring in Thermochemically Deposited Tungsten-Rhenium Alloys

Temperature (°C)	Rhenium[a] (%)	Lattice Parameter, A	
		Solid Solution	β-Tungsten
800	7.5	3.162	b
	10.1	3.155	b
	18.8	3.160	5.024
	21.4	c	5.019
	27.9	3.165	5.005
	31.9	b	5.006
1000	7.9	3.161	b
	19.2	3.160	5.021
	28.6	3.162	5.010
	38.1	3.162	4.996
1100	13.5	3.155	b
	14.8	3.152	b
	19.6	3.152	b
	23.7	3.150	5.020
	24.7	3.147	5.009
	26.1	3.148	5.014
	28.5		5.007
	42.4		4.992
1200	11.1	3.155	b
	13.5	3.155	b
	16.6	3.152	b
	18.4	3.152	b
	25.8	3.151	5.015

[a]Separate experiments.

[b]Not detected.

[c]Not measured.

[redacted]

3. NONDESTRUCTIVE TEST DEVELOPMENT

R. W. McClung

Our program is intended to develop new and improved methods of evaluating reactor materials and components. To achieve this we are studying various physical phenomena, developing instrumentation and other equipment, devising application techniques, and designing and fabricating reference standards. Among the methods being actively pursued are electromagnetics (with major emphasis on eddy currents), ultrasonics, and penetrating radiation. In addition to our programs oriented toward the development of methods, we are studying these and other methods for remote inspection.

Electromagnetic Test Methods

C. V. Dodd J. W. Luquire

Analytical Studies

We have continued research and development on electromagnetic phenomena on both an analytical and empirical basis. We are making an attempt to obtain a closed-form solution to the vector potential of a coil in the presence of a conducting material. We have solved the problem for an infinitely long coil around an infinitely long rod for any frequency, conductivity, coil thickness, and rod diameter, and have attempted to solve the problem of a coil of any length and thickness above a conducting plane. We were able to divide the problem into twelve regions and obtain a solution in each region in terms of integrals of Bessel functions. However, we have not been able to solve the integral equations for the 30 unknown constants that appear in the problem. We are investigating other orthogonal polynomials to determine appropriate solutions.

Phase-Sensitive Eddy-Current Instrument

We made further improvements on the portable phase-sensitive eddy-current instrument. We added rechargeable nickel-cadmium batteries and a recharging circuit. We also added a regulating circuit to furnish constant direct-current power despite varying temperature and battery voltage.

Spacing Measurements

We designed a series of new coolant-channel spacing probes for use in hot cells. Sturdier probes were needed to allow mechanical handling, and the longer lengths of cable required some electronic circuit modifications. We built a mold and cast the probes using both fiber-glass and a flexible epoxy covered with teflon tape. The epoxy probes were more flexible than fiber glass, but the teflon tears on a sharp object. The fiber-glass probe, however, was more rigid than the epoxy probe, and had a much harder finish that can be scratched but will not tear.

We modified the bridge circuit of the Dermitron so that one side of the coil is at ground. We then used a single shielded cable to drive the coil. This reduced the capacitance between the "hot" lead and ground, and also reduced the error due to capacitance change as the probe was inserted in the coolant channel.

Ultrasonic Test Methods

K. V. Cook

Fabrication of Reference Notches

Studies are continuing on the use of electrodischarge machining (EDM) to produce appropriate reference standards. We have recently demonstrated that we can reproducibly fabricate longitudinal notches on the inner surface of tubing with an inner diameter as small as 0.055 in. Previously, our limit had been 0.085 in. The reduction was accomplished with the special 0.040-in.-diam electrode arm shown in Fig. 3.1, incorporating a tantalum tool. Tantalum was used in

Fig. 3.1. Miniature Electrode Arm, 0.040 in. in Diameter, Used to place EDM Notches Inside Tubes with a Very Small Bore.

place of brass because the latter requires approximately twice the exposed tool due to tool burn-off. We also made successful replications of these notches.

Optical System (K. V. Cook, H. L. Whaley, Jr.)

We observed pulses of ultrasound propagating in the transparent solids, plate glass and plexiglass, using the Schlieren system developed previously.[1] Only very faint pulses can be detected in the plate glass and this is due, at least in part, to the large number of impurities in the particular piece of material employed. In plexiglass the ultrasound is very easy to see; however, due to the highly attenuative nature of plexiglass, about 1 in. of penetration is all that we have been able to observe. We plan to continue our search for a transparent solid that will allow fundamental observations of ultrasound as it propagates through a material containing discontinuities such as drilled holes and notches. When a proper transparent solid is located we feel that much can be learned concerning basic ultrasonic phenomena.

---

[1]K. V. Cook, Fuels and Materials Development Program Quart. Progr. Rept. Dec. 31, 1965, ORNL-TM-1400, p. 36.

[redacted]

Penetrating Radiation Methods

W. H. Bridges

The recently acquired closed-circuit television system was operated with a beryllium window vidicon installed in the camera. The sensitivity and resolution were markedly improved over the 10-year-old system used previously. The greatest improvement was in the response to x rays at energies below 20 kv. This increased sensitivity was due for the most part to the better signal-to-noise ratio of the total solid-state circuitry of the television system. The better resolution was a direct result of the increased number of horizontal scan lines — 1029 lines per frame as opposed to the standard 525 lines. Work to establish quantitative data is in progress.

[redacted]

[redacted]

4. ZIRCONIUM METALLURGY

M. L. Picklesimer

We are conducting research along several lines on zirconium-base alloys of potential use as structural materials for water-cooled and/or moderated reactor systems. The principal projects are: (1) studies of the physical metallurgy, including transformation kinetics and morphologies, mechanical properties, phase diagrams, and heat-treatment response; (2) the development, evaluation, and utilitzation of preferred orientation and strain anisotropy in alpha zirconium alloys during fabrication, and the use of yield stress anisotropy in increasing maximum permissible design stresses in structures; (3) the determination of the effects of composition, temperature, and environment on the oxidation-corrosion rates in the thin film stage of oxide growth; (4) a study of the effects of alloy composition and oxidation environment on the structural properties of thin oxide films *in situ*; and (5) an investigation of stress orientation of hydrides in Zircaloy-2.

Anisotropy in Zircaloy-2 and Zircaloy-4

P. L. Rittenhouse M. L. Picklesimer

Zircaloy Tubing Acquisition

Three more lots of 3/4-in.-diam Zircaloy-2 tubing have been obtained. The materials were produced from the same extruded stock with the final reductions being made by tube reducing for two lots and by ball-swaging for the other. Short sections of the extruded tube stock were obtained for texture analysis. Tapered tube sections with the complete die and mandrel profiles from six stages of tube reduction were obtained from another source. These sections will allow an examination of the development of texture in tubing as a function of the deformation in each position of each die and mandrel. Examination of all of these materials is in progress.

[redacted]

Determination of Average Basal Pole Figures

An "average" basal pole figure for Zircaloy-2 can be determined by analysis of Knoop microhardness measurements made in a specified pattern.[1] The absolute intensity (times random) of the concentration of basal poles is not, however, given by this method. It has been shown[1] that the angle $\bar{\psi}_i$ (the tilt of the basal pole from the normal to the surface being examined) determined by Knoop microhardnesses was the same as that found from basal pole figures of the same material obtained by x-ray diffraction techniques. The x-ray basal pole figures of several lots of Zircaloy-2 were examined to see if some general relationship could be established between $\bar{\psi}_i$ and the maximum intensity of basal pole concentration, $R_{(0001)}$ in each material. An empirical relationship was found and is presented in Fig. 4.1. These data allow an absolute basal pole

[1]P. L. Rittenhouse and M. L. Picklesimer, "Comparison of Pole-Figure Data Obtained by X-Ray Diffraction and Microhardness Measurements on Zircaloy-2," Trans. Met. Soc. AIME 236, 496–501 (1966).

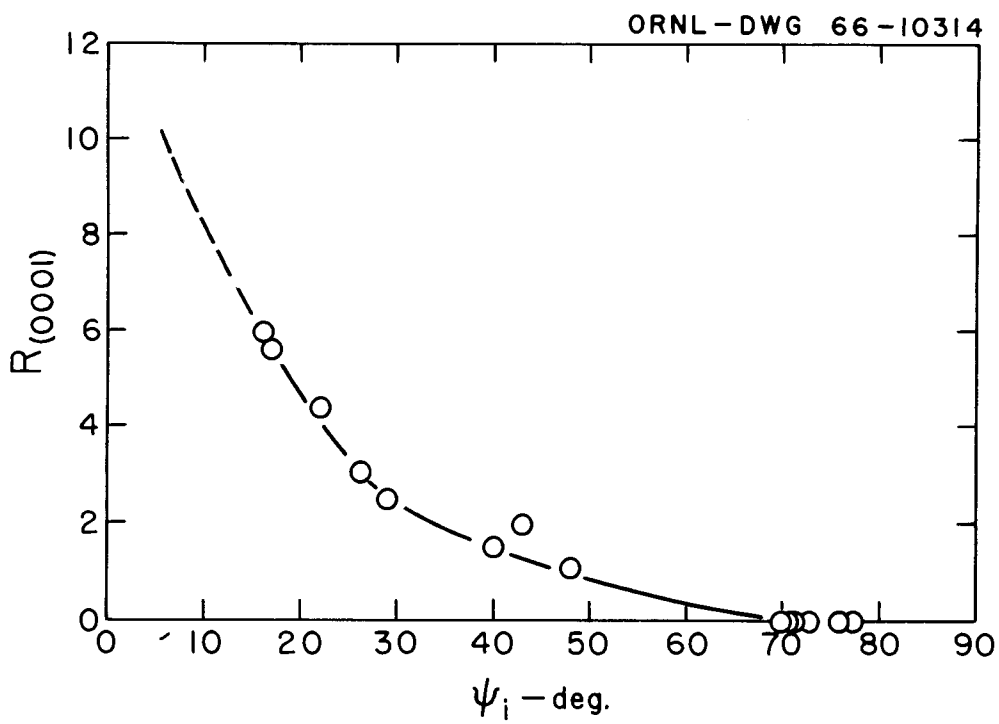

Fig. 4.1. Basal Pole Intensity, $R_{(0001)}$, vs the Angle ψ for Zircaloy-2.

intensity to be assigned at the pole of each of the planes of the specimen on which the microhardness traverses are made. Thus, it is now possible to determine both the area of the pole figure containing 50% of the basal poles of the material and the concentration of basal poles at three points of the pole figure from 36 Knoop microhardness measurements made in a specified pattern on specimens of the material. Efforts will continue to produce more information from the hardness measurements. This most recent development permits a more quantitative description of the texture by a set of simple measurements, increasing its utility in quality control in the mill and in characterization of the texture in the laboratory.

Preferred Orientation in Zircaloy Tubing

Average basal pole figures have been determined by the Knoop microhardness method for the three new lots of 3/4-in.-diam tubing. The basal pole intensities for the radial ($\overline{R}$) and tangential ($\overline{\theta}$) directions in both the tube extrusion and the finished tubing are given in Table 4.1 along with some fabrication details. The values of $R_{(0001)}$ determined for the extruded stock of material No. 1 are suspect and are being rechecked using both the Knoop microhardness method and the polarized light technique[2] (see also "Optical Properties of Zirconium Alloys," this chapter of this report). Cursory examination of this extrusion by polarized light microscopy indicates that $R_{(0001)}$ for $\overline{\theta}$ and $\overline{R}$ should be more nearly equal. Similar examination of extrusion No. 3 shows that it has a banded structure. The texture of the outer 40% of the wall thickness is such that basal poles are highly concentrated in the tangential direction but the inner region has basal pole concentrations about equal in the radial and tangential directions. The values of $R_{(0001)}$

[2]L. T. Larson and M. L. Picklesimer, "Determination of the Basal-Pole Orientation in Zirconium by Polarized-Light Microscopy," Trans. Met. Soc. AIME 236, 1104–1106 (1966).

Table 4.1. Basal Pole Intensities and Fabrication Details for Zircaloy-2 Tubing

Material	Fabrication Step	Reduction in Wall Thickness (%)	Reduction in Diameter (%)	Reduction in Area (%)	$R_{(0001)}$	
					$\bar{\theta}$	$\bar{R}$
1	Extrusion	96	58	99	5.6	2.0
2	Extrusion	94	67	99	3.0	1.6
3	Extrusion	92	73	99	3.4	1.6
1	Tube reduction	32	40	59	2.4	2.5
2	Tube reduction	44	25	59	4.7	1.6
3	Ball swaged	56	9	58	1.6	9.0

for extrusion No. 2 and all of the finished tubing from it as determined by the Knoop microhardness method are consistent with the microstructure observed in polarized light microscopy.

The ball-swaged material is unusual in that it shows three distinct bands of texture. The outer 15% of the wall thickness has basal poles highly concentrated about 20° from the radial direction, ($\overline{R}$); the next 20% has basal poles concentrated at about 45° to the radial direction, and the remainder of the wall has basal poles oriented about 30° from the radial direction. Quantitative measurements are under way.

All three lots of the finished tubing originated from the same stock and all received the same total reduction in area during fabrication, yet they have three very different crystallographic textures. This shows clearly the extreme effect of the fabrication method (tube reducing vs ball swaging) and of the reduction scheme within a given method on the texture of the finished product.

Multiaxial Testing of Tubing

Multiaxial testing of all lots of tubing has been prevented by instabilities encountered in the instrumentation used to control the programmed electro-hydraulic actuators of the testing equipment. Replacement parts for these controllers have been received and installed, and stability checks on their operation are now under way. Testing of tubing will be resumed as soon as we are assured the controllers will operate properly.

Stress Orientation of Hydrides in Zircaloy-2

P. L. Rittenhouse

Some effects of several variables on the directional precipitation of hydrides in Zircaloy-2 have been reported previously.[3–5] Two

---

[3]P. L. Rittenhouse and M. L. Picklesimer, The Effect of Preferred Orientation and Stress on the Directional Precipitation of Hydrides in Zircaloy-2, ORNL-TM-844 (June 1964).

additional variables have been recently examined — the number of precipitation cycles and the cooling rate during precipitation. The results are presented below.

Effects of Cooling Rate

Specimens of schedule J Zircaloy-2 (ref. 3) were stressed to 20,000 psi in the transverse direction while being cooled from 400°C at rates of 4 (normal), 12, and 170°C/min. The hydride pole figures[6] for the specimens cooled at 4 and 170°C/min are shown in Figs. 4.2a and b. There is obviously no appreciable effect of cooling rate on the orientation of hydrides in this material. The morphologies of the hydrides in the two cases are, however, different. In the specimen cooled at 4°C/min, the hydride plates were large and the precipitation sites were in grain boundaries and in the few twin boundaries that were present. In the material cooled at 170°C/min, the hydride plates were considerably smaller and many of them were precipitated within the grains. The majority of the intragranular hydrides were not associated with twins or twin boundaries.

Although the cooling rate seems to have had no appreciable effect on the orientation of the hydrides precipitated under stress, the location of their precipitation will have a large effect on the tensile ductility of the material. For stresses directed perpendicular to the platelets, the ductility will decrease as the platelet size increases (i.e., as the cooling rate decreases).

---

[4]P. L. Rittenhouse and M. L. Picklesimer, Precipitation of Hydrides in Zircaloy-2 as Affected by Preferred Orientation, Elastic Stress, and Hydrogen Content, ORNL-TM-1239 (September 1965).

[5]P. L. Rittenhouse, Fuels and Materials Development Program Quart. Progr. Rept. Sept. 30, 1965, ORNL-TM-1270, pp. 26–28.

[6]M. L. Picklesimer and P. L. Rittenhouse, "Hydride and Basal Pole Figures in Zircaloy-2 by Quantitative Metallography," pp. 55–79 in 19th Metallography Group Meeting held April 20–22, 1965, at the Oak Ridge National Laboratory, Oak Ridge, Tennessee, ORNL-TM-1161 (February 1966).

[redacted]

ORNL-DWG 66-8112

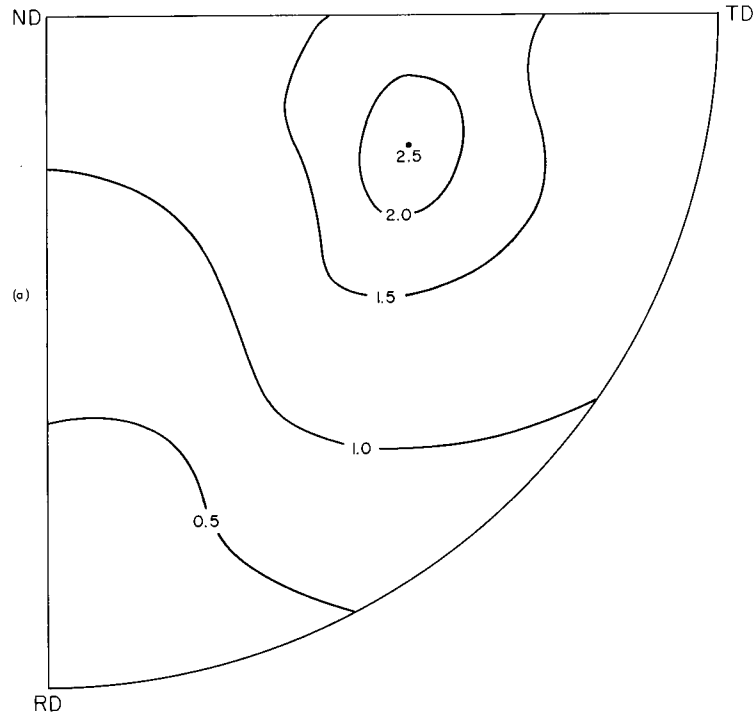

ORNL-DWG 66-8105

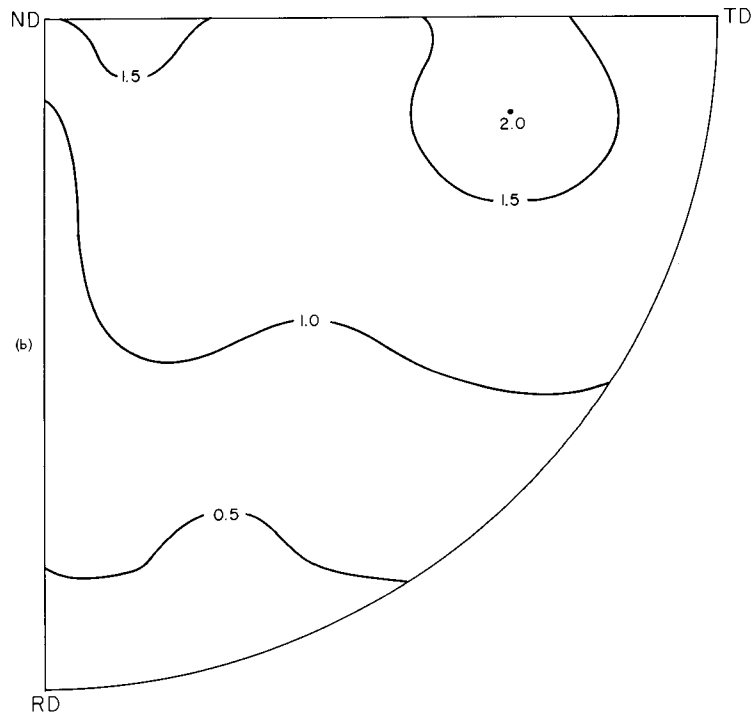

Fig. 4.2. Hydride Pole Figures for Zircaloy-2 Cooled from 400°C at 20,000 psi Applied Load, Transverse Direction. Schedule J, 120 ppm H_2. (a) 4°C/min. (b) 170°C/min.

[redacted]

Temperature Cycling Under Load

In a previously reported series of tests,[5] specimens of schedule 18 Zircaloy-2 were heated and cooled between 100 and 400°C for as many as 20 cycles while continuously under an elastic stress of 15,000 psi. A slight randomization of the hydride plates from the positions in unstressed material was observed after one cycle, and that orientation was also observed after 5 and 10 cycles. However, after 20 cycles the hydride pole density near the normal direction of the sheet material increased from 4 times random to 6, and a peak of 3 times random developed between the normal and transverse directions. At that time, we were dubious of the validity of the result for the 20-cycle specimen, so this test was rerun. A second 20-cycle specimen has produced results identical to those from the first. A 100-cycle specimen test is now under way to determine if the buildup of hydride poles continues.

Orientation of Hydrides in Unstressed Tubing

Pole figures for hydrides precipitated under no-load conditions have been determined for nine lots of Zircaloy-2 and Zircaloy-4 tubing. A fair correlation has been found to exist between the concentration of hydride poles, H_i (in units of times random), and the basal pole intensity, R_i, at the same point. Plots of $H_{\bar{R}}/H_{\bar{\theta}}$ vs $R_{\bar{R}}/R_{\bar{\theta}}$, $H_{\bar{\theta}}$ vs $R_{\bar{\theta}}$, and $H_{\bar{R}}$ vs $R_{\bar{R}}$ are shown in Fig. 4.3. Hydride pole figures for materials having basal poles predominantly in the radial and in the tangential directions are presented in Fig. 4.4a and b, respectively.

No such correlation could be found for plate or sheet Zircaloy-2. In these materials, however, values of H_i on the order of 20 were common. The values of H_i in tubing have so far all been less than 5. It is possible, then, that the hydride orientation in tubing may be sensitive to some fabrication variable or variables that produce the observed crystallographic texture, but not to the texture *per se*. The correlation observed will be examined further.

ORNL-DWG 66-10313

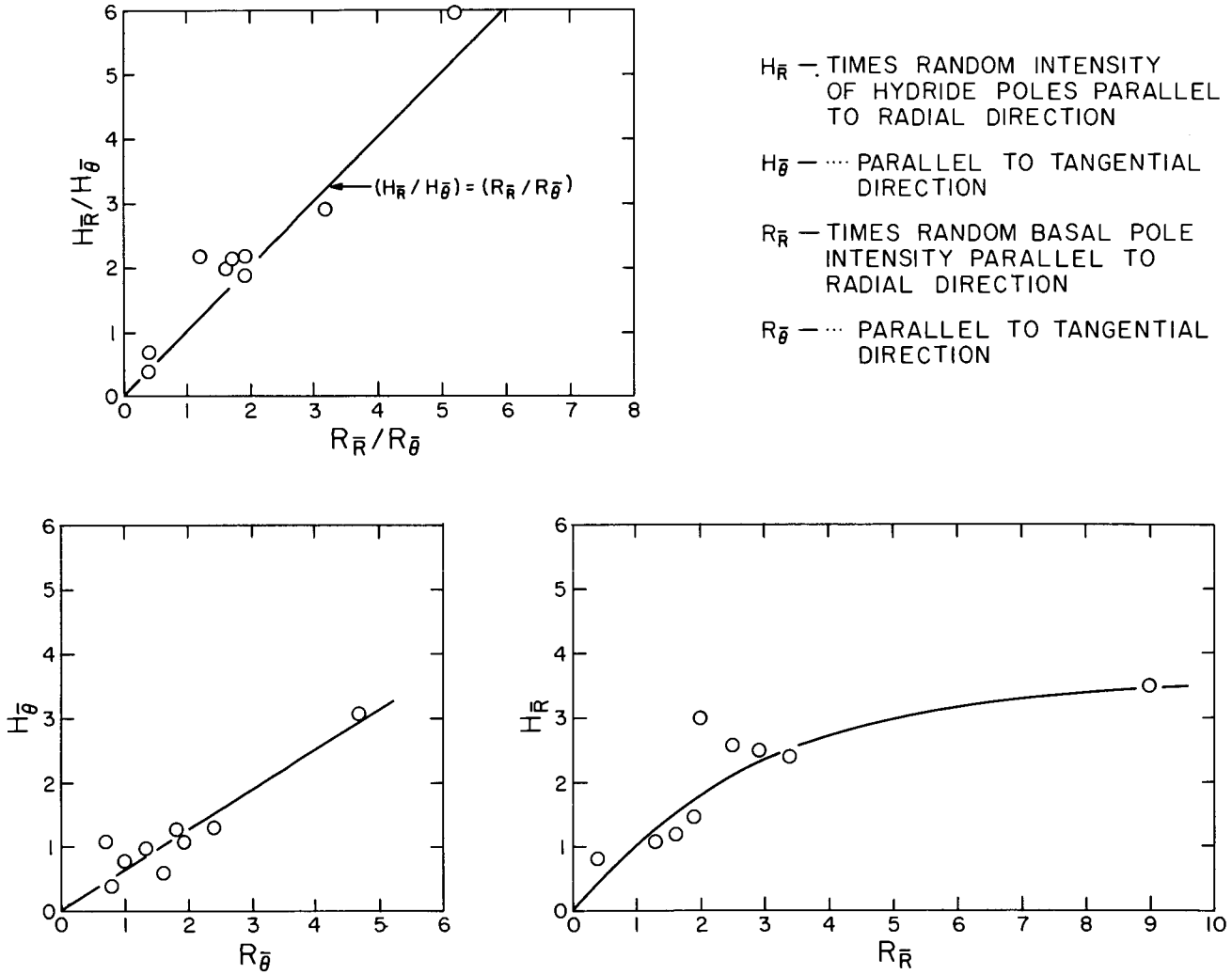

Fig. 4.3. Correlations Between Hydride Pole Density, H_i, and Basal Pole Density, R_i, in Zircaloy-2 and Zircaloy-4 Tubing.

[redacted]

ORNL-DWG 66-8111

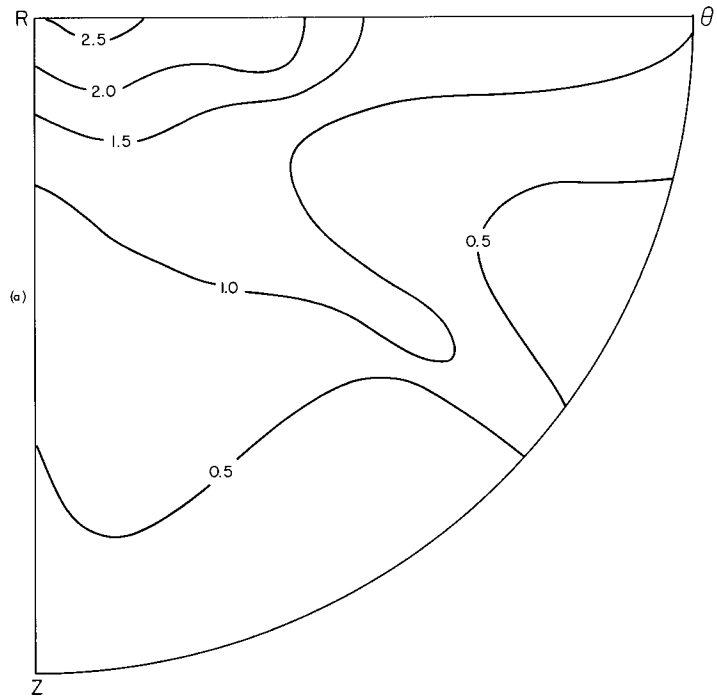

ORNL-DWG 66-9395

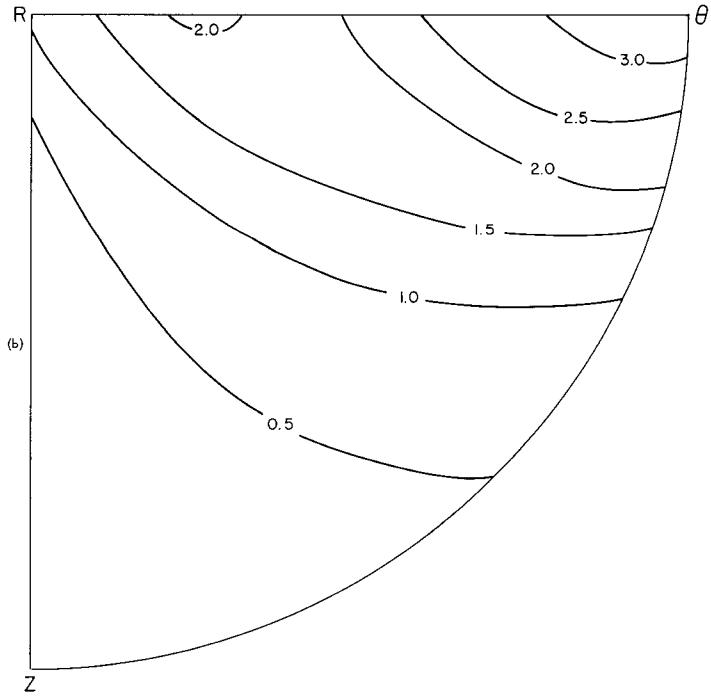

Fig. 4.4. Hydride Pole Figure for Unstressed Zircaloy-2 Tubing of Two Crystallographic Textures. (a) Basal pole parallel to the radial direction, $\overline{R}$. (b) Basal pole parallel to the tangential direction, $\overline{\theta}$.

[redacted]

[redacted]

Studies of Zirconium Alloys in Shear

D. O. Hobson

In the last report of this series, we discussed[7] the use of an x-ray diffraction technique to determine the crystallographic orientation in the shear zone of a polycrystalline zirconium alloy specimen. A specimen of zirconium was examined by this method with interesting results, which are not yet interpreted. The data typically obtained are shown in Fig. 4.5. The shear zones were seen as a general increase of intensity over background for this particular orientation on the x-ray diffraction equipment. Such changes in intensity as a function of specimen rotation and translation should provide information on the variation of the texture along the length of the specimen. The sharp intensity peaks observed in Fig. 4.5 are thought to be caused by large

[7]D. O. Hobson, Fuels and Materials Development Program Quart. Progr. Rept. June 30, 1966, ORNL-TM-1570, pp. 41–43.

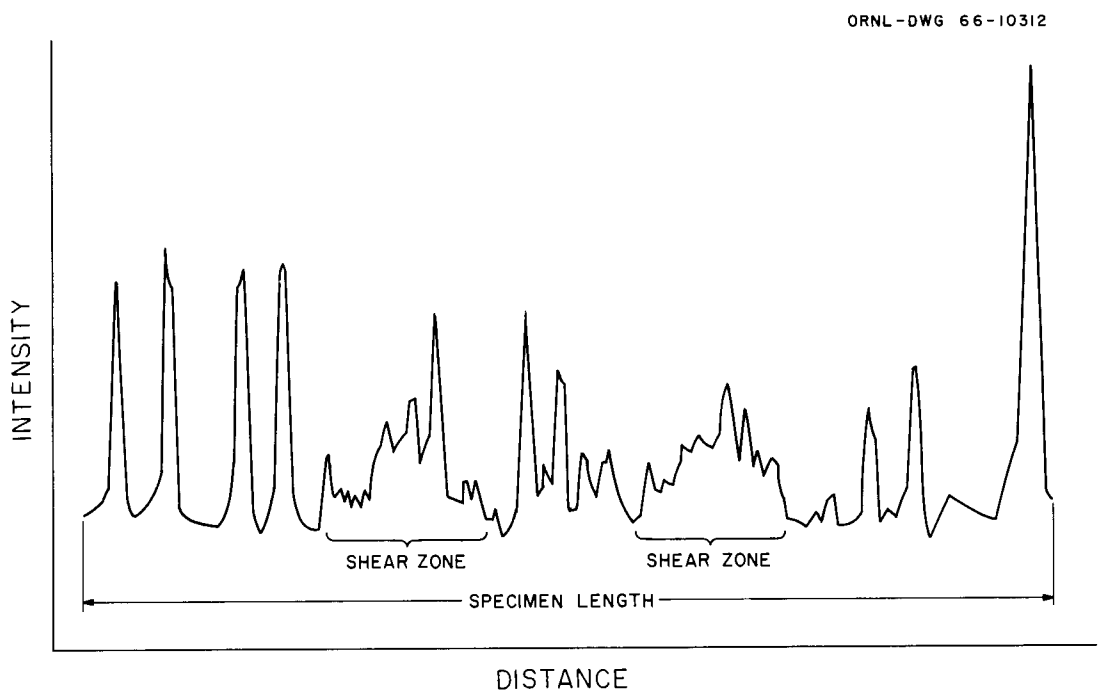

Fig. 4.5. X-Ray Intensity Trace on Translation Across Shear Zone on a Polycrystalline Specimen of Zirconium.

[redacted]

grains in the specimen being oriented just right for Bragg reflection in the very narrow beam that was used. Attempts to rotate the specimen about two axes, one parallel to the translation direction and the other parallel to the width direction of the specimen, showed that the narrow beam became skewed relative to the rotated specimen, causing it to become out of focus. If the beam slits can be rotated with the specimen, this difficulty can be resolved and the data necessary for determination of the crystallographic orientation of the material in the shear zone can be obtained. Suitable modifications of the equipment are under way.

An electrical-discharge cutting machine has been constructed for cutting the shear specimens from single-crystal stock. The shear plane and shear direction can be made to be on any desired crystallographic plane and in any direction lying in that plane. Single-crystal specimens are now being cut for determination of the shear stresses required to cause several of the known deformation systems to operate.

The mechanical stage of the polarizing microscope has been modified to permit electrical readout of linear specimen translation. This will allow a determination of the change of basal plane trace angle through the shear zone by use of the polarizing microscope and an x-y recorder. Visual examination of sheared specimens of zirconium has shown that the texture is heavily banded in the starting stock, and that this banding can be followed through the shear zone. The measurements will give information (not complete, unfortunately) on the amount and direction of texture change as a function of position relative to the shear zone of the specimen.

Optical Properties of Zirconium Alloys

L. T. Larson[8] M. L. Picklesimer

We have previously shown[9,10] that the tilt with respect to the normal to the surface of the specimen of the basal pole of any grain in a polycrystalline specimen of zirconium can be determined to a precision of about 3° by measurements of the optical property called the "angle of rotation, A_r." When this measurement is combined with that of the determination of the angular position of the basal plane trace,[9] the position of the basal pole in space can be determined by three simple measurements made with a polarized light metallurgical microscope on a single surface of the specimen. The necessary data, A_r vs angle of basal pole tilt at several wavelengths of light, obtained on a single-crystal sphere of iodide zirconium have been previously reported.[10] The reasons for the study and some of the uses of the technique were discussed earlier.[11]

Such data have now been determined for a single-crystal spherical specimen of Zircaloy-2 and are presented in Fig. 4.6. The smooth curves were calculated from the experimental measurements as a best fit to the equation,

$$A_r = a \sin^2 \alpha \qquad (1)$$

---

[8]Consultant from the University of Tennessee.

[9]L. T. Larson and M. L. Picklesimer, "Determination of the Basal-Pole Orientation in Zirconium by Polarized-Light Microscopy," Trans. Met. Soc. AIME 236, 1104–1106 (1966).

[10]L. T. Larson and M. L. Picklesimer, Fuels and Materials Development Program Quart. Progr. Rept. June 30, 1965, ORNL-TM-1200, pp. 36–39.

[11]L. T. Larson and M. L. Picklesimer, Fuels and Materials Development Program Quart. Progr. Rept. Sept. 30, 1964, ORNL-TM-960, pp. 41–43.

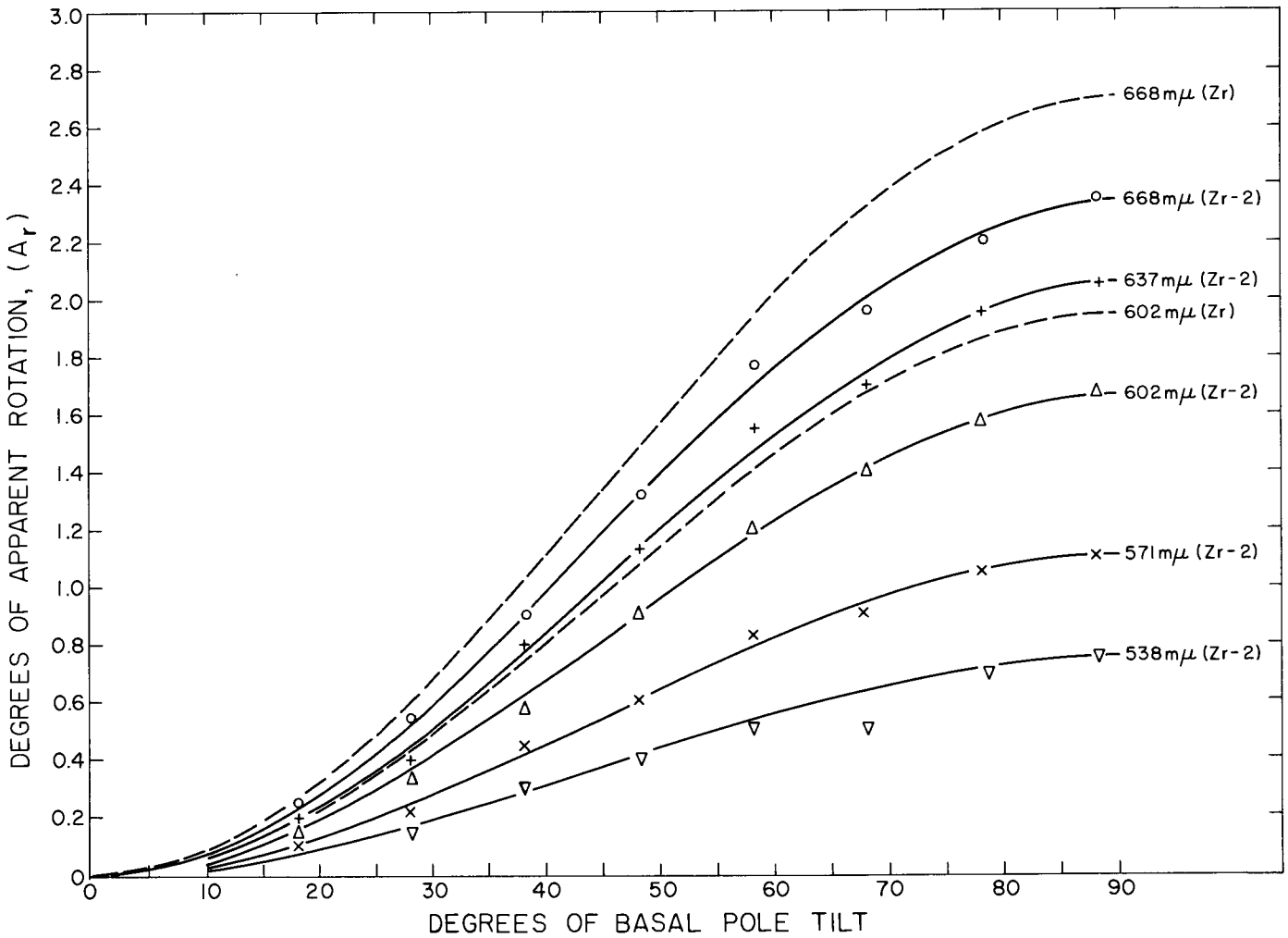

Fig. 4.6. Apparent Angle of Rotation, A_r, vs Basal Pole Tilt at Several Wavelengths of Light for Single-Crystal Zircaloy-2.

where

A_r = apparent angle of rotation,

a = a constant dependent on the wavelength of the illuminating light, and

α = angle of basal pole tilt from the optical axis of the microscope (or the normal to the surface of a flat specimen).

All attempts to find a simple, precise mathematical relationship between the constants, "a", and the wavelengths of light have failed.

These data now allow the use of the polarized light microscope to determine microtexture and texture gradients in the Zircaloy-2 and Zircaloy-4 tubing being studied in that portion of the program concerned with the anisotropy of mechanical properties of Zircaloy-2 in biaxial stress. The construction and operation of the basal pole figure plotter for such determinations were discussed in an earlier report of this series.[12] These studies are now under way.

Some of the A_r data reported previously for iodide zirconium[9,10] are also presented in Fig. 4.6 for comparison to the data for Zircaloy-2. The decrease in A_r at any given value of basal pole tilt in any chosen wavelength of monochromatic light for Zircaloy-2 from that for iodide zirconium indicates the sensitivity of the measurement to the alloy content of the material. Since the angle of rotation, A_r, can be measured at the present time to a precision of 0.05° of angle, a grain of Zircaloy-2 can be readily distinguished from one of zirconium if the basal pole orientations of both are known. The differences in A_r at given basal pole tilts at the longer wavelengths indicate that it may be possible to determine chemical composition in binary alloys by such measurements. This then leads to the possibility that we may be able to detect and measure at least semiquantitatively the partitioning of an alloying element between the oxide and the metal surface immediately beneath an oxidized or corroded specimen by quantitative microscopy.

---

[12]M. L. Picklesimer, Fuels and Materials Development Program Quart. Progr. Rept. March 31, 1966, ORNL-TM-1500, pp. 48–50.

The data reported in Fig. 4.6 for Zircaloy-2 and that for zirconium reported elsewhere[9,10] were taken with a microscope having its illuminating mirror at 45° to the optical light path of the microscope. The correction factor for that data, required to calculate the true angle of rotation, is approximately 6/5, varying somewhat with wavelength of the light. If the polarizing microscope to be used for such measurements should have the new Smith illuminating system (mirror at 22 1/2° to the optical light path), a correction factor of about 21/20 is required. Thus, if such an illuminating system is used, the data reported must first be decreased by about 5/6, and then multiplied by 21/20 to obtain a set of apparent angle of rotation data suitable for a microscope having the Smith light system.

Oxide Film Studies

J. C. Banter

The detection of phosphate ion in anodic oxide films formed on zirconium in solutions containing this ion[13] suggested that other ions might also be incorporated in the films formed in other anodizing solutions. Therefore, we measured the infrared transmission spectra of films formed on zirconium specimens in the following, commonly used, aqueous anodizing solutions: 1% KOH, 0.5 M H_2SO_4, 0.5 M $(NH_4)_3BO_3$, saturated H_3BO_3, 0.5 M citric acid, 0.5 M lactic acid, and 0.5 M oxalic acid. Spectra of films formed in 0.5 M K_2CrO_4, 0.5 M $K_2Cr_2O_7$, 0.5 M KNO_3, and 0.25 M Na_2MoO_4 were also examined.

The spectrum for the film formed in K_2CrO_4 is shown in Fig. 4.7. The two absorption bands near 3- and 6-μ wavelengths are characteristic of stretching in the O-H bond in water, indicating a hydrated oxide film. These same bands appeared in the spectra of films formed in $K_2Cr_2O_7$ and KNO_3. Apparently, appreciable amounts of water are

[13] J. C. Banter, Fuels and Materials Development Program Quart. Progr. Rept. March 31, 1966, ORNL-TM-1500, p. 52.

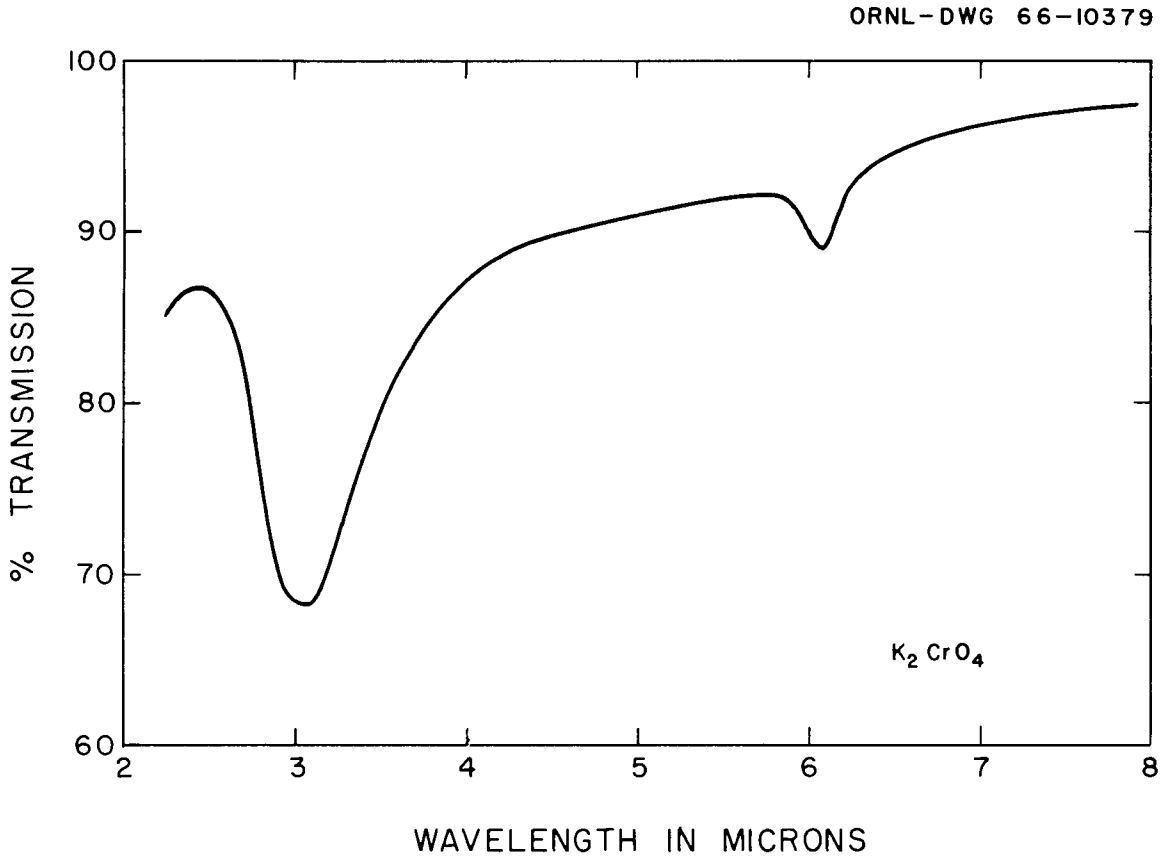

Fig. 4.7. Transmission Spectrum of Anodic Oxide Film Formed on Zirconium in 0.5 M K_2CrO_4.

incorporated in anodic films formed in strong oxidizing agents. However, no indication was found in these spectra of other incorporated ions.

Spectra of two of the other films are shown in Fig. 4.8. The absorption band at 14.3 μ in both spectra is due to ZrO_2 and the apparent bands below 3 μ are simply minima resulting from optical interference effects in the films. The absorption band at 9 μ in the spectrum of the film formed in H_2SO_4 is characteristic of sulfate ion, indicating the presence of this ion in the film. The two bands at 6.4 and 7.2 μ in the spectrum of the film formed in oxalic acid are typical of those arising from the resonance between the two possible C = O bonds in the carboxylate ion structure and indicate that oxalate ions were incorporated in the film. Similar double bonds were seen in

[redacted]

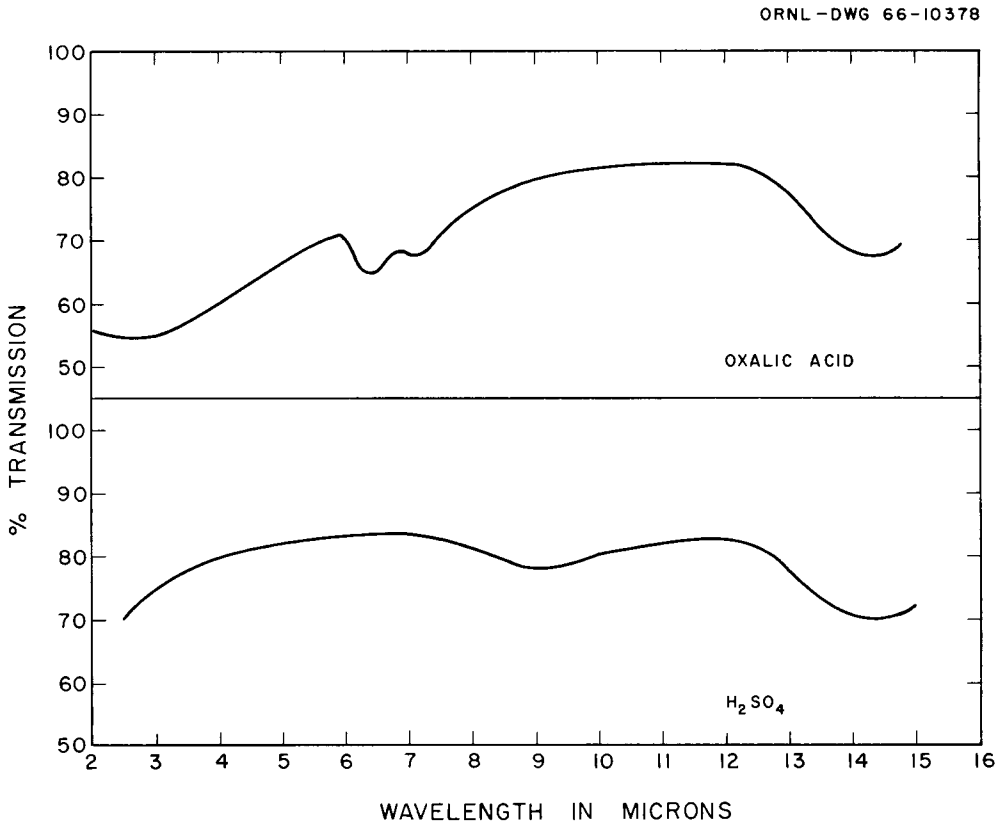

Fig. 4.8. Transmission Spectra of Anodic Oxide Films Formed on Zirconium in 0.5 M H_2SO_4 and 0.5 M Oxalic Acid.

the spectra of films formed in citric and lactic acid, thus citrate and lactate ions are also incorporated in the films. No absorption bands, other than that attributable to ZrO_2, appeared in the spectra of films formed in KOH, $(NH_4)_3BO_3$, H_3BO_3, and Na_2MoO_4. These films, then, appeared to be free of incorporated ions.

Duplicate specimens were anodized at the same voltage in several of the above solutions as well as in 1% KOH, 0.5 M H_3PO_4, and the organic solution previously mentioned.[13] The thicknesses and electrical conductivities of the resulting films were measured and compared. The data are given in Table 4.2. It is obvious that all films with incorporated ions were much thinner than those having none. The average electrical conductivity of films with no incorporated ions is about 35% higher than that for films with incorporated ions. Thus, the incorporated ions tend to limit both the film growth and the electrical conductivity of the films.

[redacted]

[redacted]

Table 4.2. Thicknesses and Electrical Conductivities of Anodic Oxide Films Formed at 100 v on Zirconium in Various Anodizing Solutions

Anodizing Solution	Film Thickness,[a,b] A		Film Conductivity (ohm^{-1} cm^{-1}) × 10^{14}	
	Specimen 1	Specimen 2	Specimen 1	Specimen 2
Organic	1780	1736	1.50	1.68
0.5 M H_3PO_4	1801	1775	1.89	1.69
0.5 M H_2SO_4	1646	1653	1.64	1.72
1% KOH	2675	2675	2.50	2.40
0.5 M $(NH_4)_3BO_3$	2360	2360	2.19	2.24
0.5 M oxalic acid	1603	1580	1.50	1.59
0.5 M citric acid	1806	1819	2.05	1.98
0.25 M Na_2MoO_4	2588	2588	2.39	2.26

[a] ±15 A estimated.

[b] Anodizing voltage was reset to 100 from zero for every specimen. Therefore the difference in film thickness between duplicate specimens is primarily due to lack of precision in setting the voltage.

Growth of oxide films on zirconium is generally believed to proceed by the diffusion of oxygen in the form of oxide ions through the film toward the metal-oxide interface with a counter diffusion of oxide ion vacancies and electrons away from that interface.[14] If the incorporated anions are held in fixed positions in the oxide films because of their large size, they would create a negative space charge which could serve as a barrier to the diffusion of both oxygen ions and electrons through the film, thereby limiting the rate of growth of the film. This model for the effect of the incorporated ions is also in agreement

[14] J. P. Pemsler, J. Electrochem. Soc. 112, 447 (1965).

[redacted]

with the previously observed fact[13] that films formed in KOH solutions dissolve into the base metal much more rapidly upon vacuum annealing then do those formed in H_3PO_4 solutions.

We plan to study the effects of incorporated ions more quantitatively with the vacuum system designed for use with the spectrophotometer. After replacing a defective valve, we successfully completed leak testing of this system, and are currently fitting standard flanges with the necessary specimen mounts, heaters, and other associated electrical equipment necessary to perform this work.

(NOTE: Dr. Banter is no longer with ORNL, having accepted a position with Florida Atlantic University, Boca Raton, Florida. This research will not continue unless a research contract can be negotiated with him at Florida Atlantic University.)

Properties of High-Purity Zirconium

J. C. Wilson

Anisotropy of Oxidation in Zirconium

Oxidation of single-crystal spheres of zirconium showed the anisotropy of oxidation in air and 500°C steam.[15] We have begun detailed studies on certain orientations (initially, on $\{0001\}$, $\{10\bar{1}0\}$, $\{11\bar{2}0\}$, and $\{10\bar{1}5\}$) to determine the characteristics of the localized, accelerated oxidation ("pustules") that occur generally on the more slowly oxidizing orientations and on, or adjacent to, hydride precipitates. Over 100 single-crystal plates have been cut for this study, but difficulties have been encountered in obtaining uniform oxidation over the specimen surface. This problem is of little concern with spherical specimens.

---

[15] J. C. Wilson, Fuels and Materials Development Program Quart. Progr. Rept. June 30, 1966, ORNL-TM-1500, pp. 42–47.

An improved steam corrosion apparatus has been built to prevent condensate reaching the specimen surface. The new apparatus will also allow uninterrupted tests to be run for a period of weeks so that oxidation in steam can be carried out past breakaway.

From the limited data obtained so far on flat single-crystal surfaces, we have observed that:

1. The accelerated oxidation at hydrides is orientation dependent (with respect to the metal substrate). The accelerated oxidation is most noticeable at hydrides on surface orientations having the slower oxidation rates.

2. The accelerated oxidation occurs on both chemically and electrochemically polished surfaces. Since there is an attack of hydrides during chemical polishing, but not during electropolishing, the acceleration is likely due to the presence of the hydrides — not to surface geometry in their neighborhood.

3. Not all hydrides, even on a single, slowly oxidizing orientation, cause accelerated oxidation. Superficially, accelerated oxidation is associated primarily with the larger hydrides, 1 μ or thicker in size.

5. SINTERED ALUMINUM PRODUCTS DEVELOPMENT

G. M. Adamson, Jr.

Sintered aluminum products (SAP) material has been designated as the construction material for the fuel rods and pressure tubes of the Heavy-Water Organic-Cooled Reactor (HWOCR).

Our program is to study the problems and parameters associated with primary billet fabrication. The purpose of these studies is to arrive at a more reliable and consistent product having the strength of a commercial 10 wt % Al_2O_3-SAP alloy. General process steps of importance are feed-powder characterization, dispersion preparation, and consolidation. The progress of our program during the last three months is summarized in the following report.

Powder Characterization

G. L. Copeland W. R. Martin

Table 5.1 lists the characteristics of the five atomized powders included in our ball-milling studies. The average particle size of the powders range from 3.5 to 12 μ with the oxide content ranging from 0.2 to 0.7%. Two powders were atomized in air and three in helium. Those powders atomized in helium were generally more spherical in shape.

In addition to the atomized powders, two commercial lithographic aluminum flake powders, which were in the ball-milled condition as received, have been studied. These were Alcoa 552 and Alcan Metal Products MD-3100. Both products are nonleafing, have a nominal flake thickness of about 0.5 μ and contain about 6% oxide. The Alcoa 552 contains 0.6% Fe and the MD-3100 contains 0.3% Fe. The iron is present mainly as inclusions picked up during ball milling.

Preliminary studies on the effects of alloy additions on the properties of SAP were initiated using filings from commercial aluminum alloys. This technique was used because of the expense and long lead times involved in aluminum alloy powder procurement.

The three alloys studied are 5052, 5154, and 5056 which contain 2.5, 3.5, and 5.2% Mg, respectively. Magnesium was chosen as the

Table 5.1. Characteristics of Spherical Aluminum Powders Used as SAP Starting Material

Grade	Manufacturer	Average Size (μ)	Surface Area (m^2/g)	Oxide Content (%)	Crystallite Size (A)	Atomizing Medium
Albron 101 (−325 mesh fraction)	Alcoa	12				Air
MD X-65	Alcan Metal Products	6.5	0.754	0.3	790	Air
VMP H-3	Valley Metallurgical Processing Corporation	3.5	0.996	0.4	1050	Helium
VMP H-5	Valley Metallurgical Processing Corporation	6	0.803	0.7	910	Helium
VMP H-10	Valley Metallurgical Processing Corporation	10	0.594	0.2	910	Helium

alloying element mainly because of its high solubility and large atomic size difference (good solid-solution strengthening). The alloys were available in sheet or wire form and were filed into powder using a continuous band file. Type 1100 aluminum was included to provide base-line data.

Dispersion Preparation

W. R. Martin C. F. Leitten, Jr.

We have, in general, considered three methods of dispersion preparation. These are (1) ball milling, (2) controlled oxidation, and (3) mechanical blending. The first two were selected for further investigation at ORNL. These investigations have indicated that ball milling is the most logical approach to be used for industrial production of SAP-like materials today.

Ball Milling (G. L. Copeland)

To date, ball milling has been done in 10-in.-diam by 10-in.-long aluminum mill jars. The batch size has been 300 g for most of the work. The characteristics of the starting powders used are listed in Table 5.1. The particle size and shape, over the range covered in Table 5.1, do not appear to affect milling characteristics. All the starting powders discussed in the preceding section were ball milled early in the milling studies program. They were nearly all milled in aluminum jars without internal lifter bars and with aluminum balls. The exception is H-5 powder, some of which was milled as above and some in mills with lifter bars using aluminum or stainless steel balls.

Lubricants used were stearic acid, oleic acid, and silicone in a varsol vehicle. In addition, silicone was used as a vehicle and lubricant. Based on the results obtained in the early work, the following process has been selected for scale-up. Wet milling in a varsol medium will be used, as it gives a more homogeneous product with less carbon contamination than does the dry-milling "jelly-roll" process.

Stearic acid was chosen as the lubricant. Of the three investigated, it gives the lowest oxide content-to-surface area ratio. Thus, for a given oxide content, a thinner flake is produced. Steel balls will be used, since they give a more uniform and more reproducible product than the lighter aluminum balls. Magnetic separation will be used to remove the objectionable large iron inclusions picked up during the milling. The starting powder shape and size (within the less than 20-μ nominal size range investigated) does not appear to significantly affect the final product. Thus, air-atomized, −100 mesh powder will be used since it is the least expensive of the powders investigated.

Equipment is presently being procured that will enable the production of 50-lb lots by a process representative of a production-scale process. The ball mill will be 36 in. in diameter and 16 in. long. The diameter is the critical dimension for milling action. Thus, it is expected that this mill will be representative of a much longer, production-size mill. The slurry removed from the mill will be filtered with a pressure filter to remove the majority of the varsol. The approximately 85% solid filter cake will then be dried in a rotary vacuum dryer at about 320°F or higher. This removes the vehicle but leaves the remaining stearates on the surface of the powder. A high-temperature vacuum anneal of either the powder or the cold-pressed billets will be used to stabilize the oxide and remove the stearates remaining from the lubricant.

Six consecutive batches run under identical conditions yielded oxide contents of 11.0, 11.2, 11.4, 11.4, 10.9, and 10.7% after 10-hr milling in the 10-in.-diam mills with steel balls. The standard deviation of these batches is about the same as the standard deviation of the analysis for oxide contents in this range. This indicates the process is highly reproducible for this size batch.

Controlled Oxidation of Aluminum Powders (W. B. King[1] and R. L. Heestand)

Two approaches to the controlled oxidation of aluminum powders are being investigated. In the first, distilled water is added to the powder

[1]Consultant from the University of Miami.

to give the desired amount of hydrate. This is then converted to oxide by heating in vacuum at 600°C. The oxide formed in this manner retains the shape of fan-like platelets characteristic of the alpha monohydrate. Material in 300-g quantities and containing from 5 to 22% oxide was prepared and extruded. Strength results obtained on 12 and 22% oxide material indicate behavior characteristic of material produced by conventional preparation, that is, high strength and low ductility. Lower oxide content material has not been extruded.

In the second method the powder is heated to 550°C in vacuum and held for 18 hr to convert residual oxide and hydrates to ceramic-grade oxide. Oxygen is then introduced into the system at the reduced pressure to produce the desired oxide content. The pyrophoricity of the powder was of concern, but the combination of stabilizing the powder by conversion of the residual oxide and allowing the reaction to proceed at reduced pressures minimizes the explosion hazard.

Examination of the oxidized powders by electron microscope shows the oxide layers to be smooth with no fan-like growths as experienced with hydrate conversion. X-ray diffraction indicates the oxides to be mixtures of gamma, eta, chi, and delta forms. The broad band at 4.5 A, which is said to characterize amorphous hydrated material, was not found on any of the patterns.

Strength results of extruded material containing 9.4% oxide again show characteristics similar to conventional SAP material.

The above methods of preparation should give good control of oxide content and follow a more predictable route to the formation of ceramic-grade oxides. Results on the strength and ductility to date show no improvement over existing processes and indicate that further treatment prior to consolidation is necessary.

Powder Consolidation

M. M. Martin D. L. Turner
G. L. Copeland

The primary purpose of consolidation is to put SAP powder in a convenient geometric shape for subsequent extrusion while retaining

and/or converting the oxide to a stable form of predictable morphology. The direct extrusion of powder is not practical, since the bulk density is about 0.1% that of the extruded rod. Previous work at ORNL has centered around cold- and vacuum hot-pressing of flake powder, usually containing less than the specified 10 wt % Al_2O_3.

The powders listed in Table 5.1 were prepared for mechanical property testing using the techniques described below.

The ball-milled powder was pressed into 2-in.-long by 2-in.-diam billets using a vacuum hot-pressing operation. This pressing consists of heating the powders to 600°C and holding for 2 hr followed by pressing at about 2.2 tsi, all under a vacuum of $< 10\ \mu$. This results in a billet density of at least 95% of theoretical.

One billet each of the VMP H-5 and 101 powders was cold pressed and then vacuum annealed at 600°C for 20 hr.

Prior to hot extrusion each billet was preheated for about 60 min in air. Preheat temperatures used for the atomized powder billets were 500 and 600°C. The billets were then inserted into the extrusion chamber, which was maintained at about 440°C, and extruded immediately. Thus, the actual temperature of the billet during extrusion could have been as low as the 440°C chamber temperature.

Reduction ratios of 20:1 and 30:1 were accomplished using shear dies. The effects of hot swaging the rod after a 20:1 extrusion were studied on four grades of powder. These rods were reheated for 10 to 15 min between swaging passes.

In the case of the commerically milled aluminum flake powders, the as-received powder was vacuum hot pressed into the 2-in.-diam by 2-in.-long billets and hot extruded as outlined above. Various billet preheat temperatures and extrusion ratios were used. The powders made from aluminum alloy filings were vacuum hot pressed and hot extruded at 30:1 into rods after ball milling.

The objective of a current series of consolidation experiments is to evaluate six distinct processes for producing SAP extrusion billets from Al–6.6 wt % Al_2O_3 alloy flake powder. Figure 5.1 is a schematic diagram of the various fabrication routes under investigation. Important procedures held constant for the screening test include

ORNL DWG. 66-12560

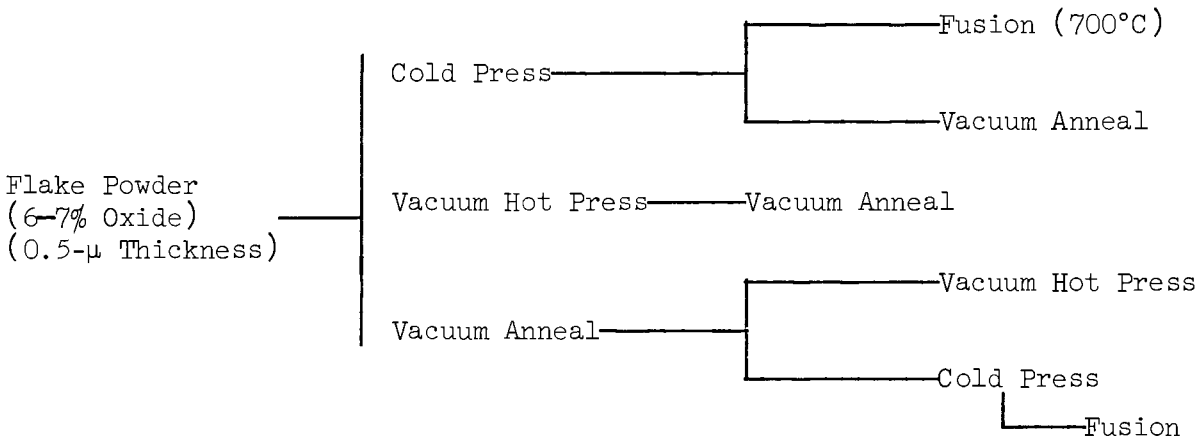

Fig. 5.1. Possible Processes for Fabricating SAP Extrusion Billets.

(1) 30-to-1 reduction ratio, (2) 436°C billet temperature immediately prior to extrusion, (3) billets 78% of theoretical density, and (4) vacuum anneal treatment(s) totalling 20 hr at 600°C to convert the oxide to a "stable" form. Since the constant parameters may not represent the optimum conditions, the process that yields superior mechanical properties at 450°C and a strain rate of 0.0002 in./in. will be optimized for the specified Al–10 wt % Al_2O_3 alloy flake powder.

Evaluation of Product

W. R. Martin C. F. Leitten, Jr.

Standard techniques were used to evaluate the SAP produced and procured by ORNL. These include metallography, electron microscopy, x-ray diffraction, chemical analysis, nondestructive testing techniques, and mechanical properties measurements.

High-Temperature Stability of Alloy After Extrusion (G. L. Copeland)

Several alloys produced during this program have developed internal fissures and microcracks after heating in air for several hours at 680°C. This effect has been investigated by Hansen and Adolph[2] who related the occurrence of internal fissures (above 500°C) and blisters (above 610°C)

[2]N. Hansen and E. Adolph, The Effect of Heat Treatments on the Structural Stability of Sintered Aluminum Products, Risö Report No. 25 (1961).

to the hydrogen content of the alloy. They concluded that a vacuum anneal at 600°C for 20 hr reduced the hydrogen content to a level (less than 10 ppm) such that further annealing in air at 600°C produced no deleterious effects. Vacuum fusion analysis for some ORNL-produced rods indicated hydrogen contents around 3 ppm. Sections of SAP rods containing 3 to 18% oxide were annealed to determine their stability as extruded and after a vacuum treatment. The heat treatments given each rod were:

1. 20 hr at 600°C in vacuum of 5×10^{-3} torr,
2. 20 hr at 600°C in air,
3. 20 hr at 600°C in vacuum of 5×10^{-3} torr, followed by 20 hr in air at 600°C.

In addition, sections of two of the rods were annealed in air at 600°C for 118 hr.

The results were essentially the same for the three treatments. No blisters were observed on any of the samples during visual examination. The samples were examined metallographically for internal fissures. The results may be segregated into two categories.

Rods Containing 6% Oxide and made from Commercial Flake. — These materials contain 0.3 to 0.6% Fe, mostly in the form of inclusions picked up in milling. The milling lubricant was oleic acid. Rods that were extruded from vacuum hot billets (pressing involved 2 1/2 hr in vacuum at 600°C) were definitely unstable during the heat treatments, as shown in Fig. 5.2. Numerous large cracks occurred that were easily visible at 1×. However, if either the starting powder or the pressed billet was vacuum annealed for 20 hr at 600°C to stabilize the oxide, the extruded rods were stable during heat treatment, as illustrated in Fig. 5.3. The stable rods contained no cracks or fissures, even after heating in air at 600°C for 118 hr. The iron inclusions underwent a transformation during the heat treatment, probably to $FeAl_3$. Very careful metallographic polishing was required to prevent loss of this new phase. The particles were transformed about 50% after 40 hr at 600°C and were almost completely transformed after 118 hr.

Rods Made from ORNL-Milled Flake. — These were 3 and 6% oxide rods made from flake milled with a silicone lubricant, and 10 and 18% oxide rods made from flake milled with stearic acid lubricant. These rods

[redacted]

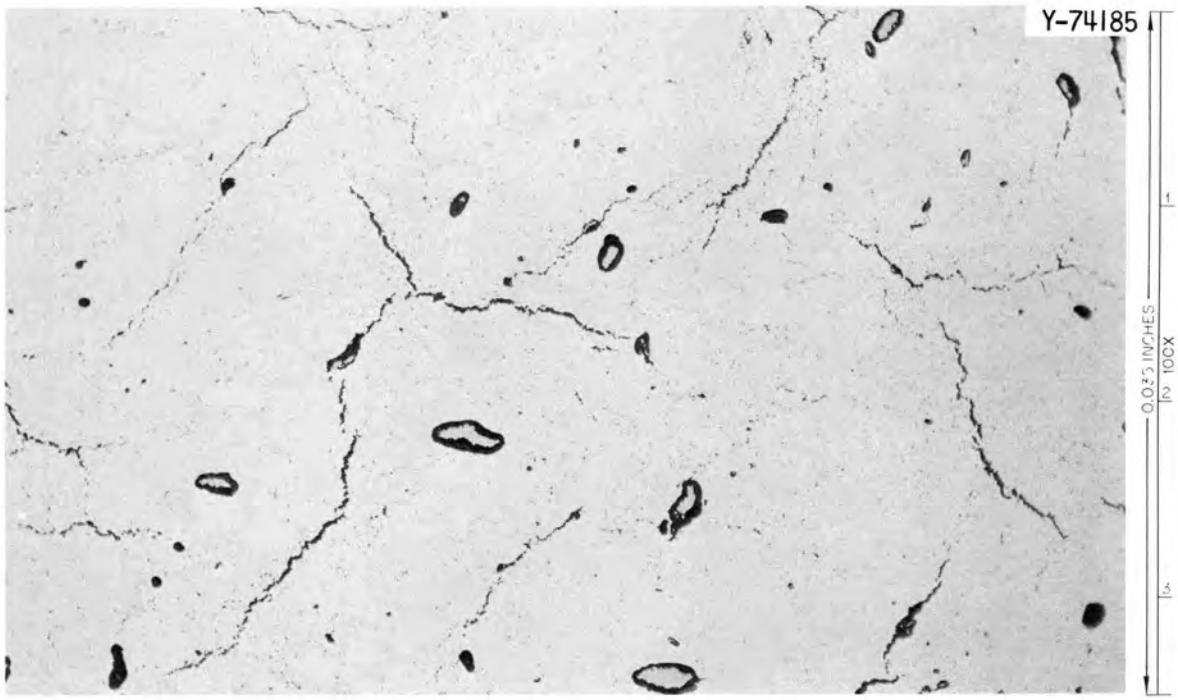

Fig. 5.2. SAP-81 Rod Containing 6% Oxide Made from Commercial Flake, which was Vacuum Hot Pressed for 2 1/2 hr at 600°C and Extruded. Extruded rod was annealed in air for 20 hr at 600°C. Transverse section. As polished.

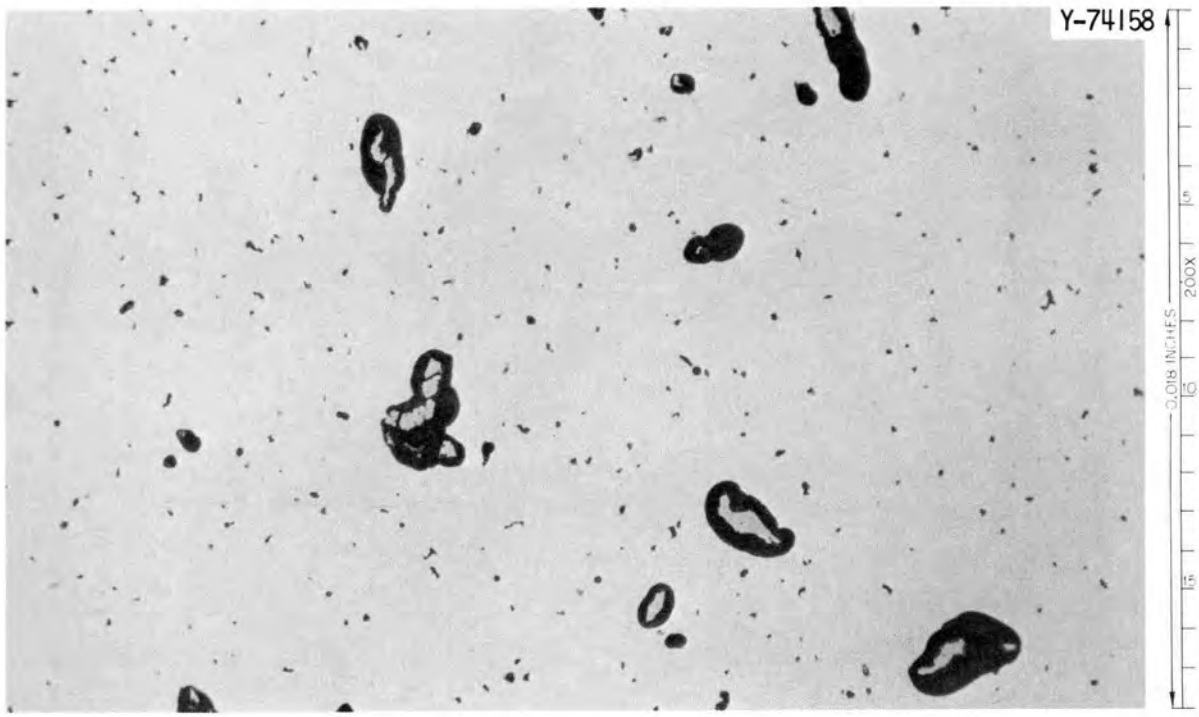

Fig. 5.3. SAP-73 Rod Made from Commercial Flake, which was Pressed and Vacuum Annealed for 20 hr at 600°C Prior to Extrusion. The Iron inclusions have partially transformed during annealing. Transverse section. As polished.

[redacted]

contained less than 0.1% Fe with no large inclusions. These rods were structurally stable during the heat treatments with no cracks and very few fissures formed. The extrusion billets were prepared by vacuum hot pressing with 2 1/2 hr in vacuum at 600°C.

Further work is in progress to identify the transformed phase around the iron particles and to determine if iron content or milling lubricant is significant in the high-temperature behavior of the extruded alloy. The lower hydrogen contents of these alloys and the similar behavior in air and in vacuum indicate a mechanism different from that investigated by Hansen and Adolph.[2]

Identification of the Oxide Species in Extruded SAP Rods (J. E. Spruiell)

An attempt has been made to identify the oxide species in extruded SAP rods. The approach has been to concentrate the oxide phases by dissolving the aluminum matrix in warm concentrated HCl. The solids remaining after digestion of the extruded sample are recovered by centrifuging. These solids are washed several times in warm water to remove any $AlCl_3 \cdot 6\ H_2O$ that may have formed during the digestion process. The remaining solids are dried at 70°C and examined by making Debye-Sherrer x-ray diffraction patterns from them.

It has been possible to obtain excellent Debye-Sherrer patterns, which indicate that the oxides leached from SAP extruded rods by the above technique consist of a mixture of η and χ aluminum oxides. There appears to be a considerably larger fraction of η than of χ. These results are in agreement with the results of previous investigators.[3]

A control test has shown that β aluminum trihydrate ($Al_2O_3 \cdot 3\ H_2O$) dissolves in concentrated HCl. Thus, if it were present in the SAP rods, it would be removed with the aluminum matrix in the above digestion technique. This may be true of other hydrates also. Although no x-ray diffraction lines inconsistent with either η or χ have been

---

[3]J. Dejace, EURATOM's Scientific Activities. ORGEL Program — Experimental Studies, EUR 1830.e, Part II, pp. 60–62, European Atomic Energy Community (EURATOM), Brussels, 1964.

observed in x-ray patterns of bulk SAP samples (except lines corresponding to Al_4C_3), it cannot at present be definitely said that a small smount of hydrate does not exist in the extruded SAP rods. A method for determining whether any hydrate occurs in extruded SAP rods is being explored. This method consists of a quantitative determination of the amount of oxide leached from the samples by the above technique and a comparison of these results to the total aluminum oxide content in the rods, as determined by the standard analytical technique.

Mechanical Properties Evaluation (D. G. Harman)

Properties of SAP Made From Atomized Powders. — Short-time tensile properties of rod extruded from the five grades of atomized powder listed in Table 5.1 are shown in Tables 5.2 through 5.6. Table 5.7 lists the data on swaged rod.

The oxide content given in the tables refer to analyses made on the extruded rods. Milling lubricants, extrusion ratios, and billet preheat temperatures are included.

It is apparent that the several variables involved are not adequately treated for any firm conclusions. Certain trends among the five powders are evident and can be used for some cursory comparisons.

The high-temperature strength of SAP from Alcoa's Albron 101 powder was consistently on the low side (with respect to oxide content). Valley Metallurgicals' H-3, H-5, and H-10 were all at an approximately identical higher strength level. Alcan Metals' MD X-65 was on the high strength side which was probably due in part to the lubricant used as will be pointed out below. At oxide levels of $< 4\%$, SAP from 101 grade powder showed the highest ductility (percent total elongation). There was appreciable scatter in the ductility data with no other trends being evident with respect to powder grade.

The effects of milling conditions and lubricants can best be appraised by considering the data on a single powder grade. The VMP H-5 data listed in Table 5.5 are the most appropriate for this comparison.

Table 5.2. Short-Time Tensile Properties of SAP Rod Extruded from Ball-Milled and Vacuum Hot-Pressed Albron 101 Aluminum Powder

Material	Reduction Ratio	Billet Preheat Temperature (°C)	Milling Medium	Strain Rate (min^{-1})	Test Temperature (°C)	Yield Strength, psi		Ultimate Tensile Strength (psi)	Elongation, %	
						0.02%	0.2%		Uniform	Total
SAP-35 1% Al_2O_3	20:1	500	Varsol + 1% stearic acid	0.02	25–29	9,850	12,160	16,170	13.2	24.5
				0.02	450	3,620	4,280	4,380	0.8	15.7
SAP-36 1% Al_2O_3	20:1	500	Varsol + 1% stearic acid	0.02	25–29	8,580	12,620	17,730	14.2	22.8
				0.02	450	5,590	5,920	5,920	0.6	7.6
				0.002	450	4,300	5,290	5,370	0.7	4.1
SAP-107 2.3% Al_2O_3	30:1	500	Silicone	0.02	25–29	14,790	19,150	24,320	12.3	20.8
				0.02	450	5,590	6,410	6,410	0.4	8.7
				0.002	450	4,280	4,720	4,980	0.6	5.2
				0.0002	450	4,260	4,510	4,680	1.2	2.2
SAP-112 2.5% Al_2O_3	30:1	500	Varsol + 3% stearic acid	0.02	25–29	14,520	18,700	23,130	11.2	23.7
				0.02	450	4,940	5,930	6,010	0.5	9.5
				0.002	450	4,950	6,100	6,350	0.7	4.4
				0.0002	450	4,430	4,840	6,070	1.1	2.6
SAP-108 3.8% Al_2O_3	30:1	500	Silicone	0.02	25–29	11,170	17,700	26,470	12.5	21.0
				0.02	450	7,220	7,790	7,790	0.6	8.9
				0.002	450	5,000	5,820	5,910	0.7	4.9
				0.0002	450	5,380	5,790	5,960	0.4	2.1
SAP-165 5.3% Al_2O_3	30:1	500	Varsol + 3% stearic acid	0.02	25–29	12,800	15,860	21,060	14.5	25.4
				0.02	450	5,340	6,250	6,410	1.2	10.5
				0.002	450	5,350	6,090	6,180	1.2	5.7
				0.0002	450	4,930	5,920	6,170	0.6	2.7
SAP-133[a] 6.0% Al_2O_3	30:1	500	Varsol + 3% stearic acid	0.02	25–29	17,310	22,210	29,140	8.9	18.6
				0.02	450	7,760	9,270	9,440	0.5	2.7
				0.002	450	6,750	7,980	8,150	0.5	1.4
				0.0002	450	5,920	7,360	7,950	0.8	1.2
SAP-30[b] 8.8% Al_2O_3	16:1	600	Varsol + 1% stearic acid	0.02	25–29	25,060	30,820	36,980	3.9	14.2
				0.02	450	11,640	13,440	13,770	0.7	2.2
				0.0002	450	10,490	11,720	11,970	0.7	1.0
SAP-29[b] 9.5% Al_2O_3	16:1	600	Varsol + 1% stearic acid	0.02	25–29	25,060	30,980	37,390	7.8	15.0
				0.02	450	10,990	13,530	14,100	1.0	2.3
				0.0002	450	9,750	10,870	11,330	0.6	0.8

[a]Cold press plus 20 hr vacuum anneal at 600°C.

[b]Swaged to rod.

Table 5.3. Short-Time Tensile Properties of SAP Rod Extruded from Ball-Milled and Vacuum Hot-Pressed MD X-65 Aluminum Powder[a]

Material	Extrusion Ratio	Milling Medium	Strain Rate (min^{-1})	Test Temperature (°C)	Yield Strength, psi		Ultimate Tensile Strength (psi)	Elongation, %	
					0.02%	0.2%		Uniform	Total
SAP-71	20:1	Varsol +	0.02	25–29	17,720	24,160	29,680	11.8	19.2
2.5% Al_2O_3		3% oleic acid	0.02	450	7,490	9,220	9,260	0.55	4.5
			0.002	450	5,600	8,310	8,930	0.91	3.3
			0.0002	450	5,600	7,580	8,240	0.7	1.5
SAP-109	30:1	Varsol +	0.02	25–29	15,860	19,560	25,880	13.4	18.5
1.7% Al_2O_3		3% oleic acid	0.02	450	6,060	6,880	6,960	1.0	7.6
			0.002	450	5,740	6,480	6,570	0.8	4.4
			0.0002	450	5,340	6,240	6,330	0.9	3.8
SAP-65	20:1	None[b]	0.02	25–29	8,720	11,110	15,970	16.3	29.0
1.2% Al_2O_3			0.02	450	2,140	2,630	2,800	3.8	39.2
			0.002	450	1,150	1,680	1,970	2.3	21.5

[a]Billet preheat temperature, 500°C.

[b]Vacuum hot-pressed as-received powder.

[redacted]

Table 5.4. Short-Time Tensile Properties of SAP Rod Extruded from Ball-Milled and Vacuum Hot-Pressed VMP H-3 Aluminum Powder[a]

Material	Extrusion Ratio	Milling Medium	Strain Rate (min^{-1})	Test Temperature (°C)	Yield Strength, psi		Ultimate Tensile Strength (psi)	Elongation, %	
					0.02%	0.2%		Uniform	Total
SAP-59	30:1	Varsol +	0.02	25–29	17,720	21,430	27,620	4.6	17.8
2.8% Al_2O_3		1% stearic	0.02	450	8,430	9,510	9,510	0.4	4.5
		acid	0.002	450	7,790	8,860	9,030	0.7	3.3
			0.0002	450	6,840	8,410	8,780	0.6	2.3
SAP-110	30:1	Silicone	0.02	25–29	17,230	21,250	26,830	8.2	15.4
1.8% Al_2O_3			0.02	450	6,610	7,680	7,680	0.4	6.8
			0.002	450	5,370	6,130	6,180	0.8	3.3
			0.0002	450	4,760	5,660	5,820	1.0	2.4
SAP-114	30:1	Silicone	0.02	25–29	17,370	21,260	28,040	10.0	16.9
2.1% Al_2O_3			0.02	450	6,250	7,070	7,190	0.8	10.8
			0.002	450	5,620	6,610	6,770	1.0	6.0
			0.0002	450	5,420	6,570	6,730	0.6	2.5
SAP-70	20:1	Silicone	0.02	25–29	13,150	19,470	26,130	9.8	17.7
2.7% Al_2O_3			0.02	450	5,520	7,080	7,410	1.0	4.5
			0.002	450	5,360	6,440	6,770	1.3	2.6
			0.0002	450	4,370	5,360	6,060	1.1	1.4
SAP-118	30:1	Varsol +	0.02	25–29	22,600	28,500	37,310	6.7	11.2
6.0% Al_2O_3		10% sili-	0.02	450	9,280	10,520	10,690	0.6	2.6
		cone	0.002	450	8,610	10,170	10,420	0.9	1.9
			0.0002	450	7,650	9,400	10,140	1.1	1.5
SAP-122	30:1	Varsol +	0.02	25–29	25,470	33,360	44,370	9.7	14.5
7.3% Al_2O_3		2.5% sili-	0.02	450	10,370	12,510	12,920	0.7	3.2
		cone	0.002	450	9,570	11,460	11,870	0.8	2.2
			0.0002	450	7,260	10,230	11,210	1.2	1.4
SAP-67	20:1	None[b]	0.02	25–29	12,970	14,490	17,780	11.1	20.8
0.8% Al_2O_3			0.02	450	3,040	3,620	3,780	1.7	37.0
			0.002	450	1,810	2,630	2,880	2.5	22.1

[a]Billet preheat temperature, 500°C.

[b]Vacuum hot-pressed as-received powder.

[redacted]

[redacted]

Table 5.5. Short-Time Tensile Properties of SAP Rod Extruded from Ball-Milled and Vacuum Hot-Pressed VMP H-5 Aluminum Powder[a]

Material	Extrusion Ratio	Milling Medium	Strain Rate (min^{-1})	Test Temperature (°C)	Yield Strength, psi		Ultimate Tensile Strength (psi)	Elongation, %	
					0.02%	0.2%		Uniform	Total
SAP-111	30:1	Silicone	0.02	25–29	17,280	21,650	26,750	8.4	16.4
1.7% Al_2O_3			0.02	450		5,510	5,600	0.5	6.1
			0.002	450	5,090	5,910	5,990	0.7	3.2
			0.0002	450	4,590	5,330	5,330	1.0	1.2
SAP-146	30:1	Varsol +	0.02	25–29	21,270	25,150	27,620	9.3	17.4
		1% stearic	0.02	450	8,480	9,710	9,800	0.9	4.8
		acid	0.002	450	7,750	9,150	9,320	0.9	3.3
			0.0002	450	7,780	8,610	9,020	0.6	1.9
SAP-135[b]	30:1	Silicone	0.02	25–29	17,840	23,900	31,780	8.6	10.5
3.6% Al_2O_3			0.02	450	6,730	7,730	7,880	0.4	3.3
			0.002	450	5,670	6,750	6,850	0.5	1.7
			0.0002	450	5,280	6,430	6,840	0.6	1.0
SAP-143	30:1	Varsol +	0.02	25–29	18,400	25,250	32,500	9.1	14.4
6.0% Al_2O_3		1% stearic	0.02	450	7,340	10,560	11,740	0.9	3.6
		acid	0.002	450	10,550	12,090	12,330	0.6	1.5
			0.0002	450	9,750	11,650	11,890	0.9	1.5
SAP-101	30:1	Varsol +	0.02	25–29	24,800	31,000	38,500	7.6	11.5
7.2% Al_2O_3		3% oleic	0.02	450	9,410	11,810	13,460	1.2	3.0
		acid	0.002	450	10,720	12,780	13,190	0.9	2.0
			0.0002	450	6,760	12,200	12,530	1.2	1.7
SAP-145	30:1	Varsol +	0.02	25–29	28,100	35,700	46,940	7.8	11.1
9.5% Al_2O_3		1% stearic	0.02	450	14,630	16,760	16,930	0.6	2.1
		acid	0.002	450	13,180	15,490	15,730	0.5	1.3
			0.0002	450	9,910	13,880	14,620	0.6	1.0
SAP-144	30:1	Varsol +	0.02	25–29	28,800	35,000	44,200	6.2	10.0
8% Al_2O_3		1% stearic	0.02	450	13,380	15,860	17,010	0.9	2.2
		acid	0.002	450	12,410	14,480	15,630	0.9	1.4
			0.0002	450	10,880	13,610	14,510	0.8	1.1
SAP-120	30:1	Varsol +	0.02	25–29	23,000	29,000	39,800	10.3	14.2
6.8% Al_2O_3		10% silicone	0.02	450	8,920	10,260	10,840	0.9	2.8
			0.002	450	7,940	9,170	10,400	1.0	2.3
			0.0002	450	8,140	8,560	9,570	0.8	1.7
SAP-121	30:1	Varsol +	0.02	25–29		32,920	41,730	8.2	13.1
9.2% Al_2O_3		1.5% stearic	0.02	450	12,440	14,350	14,680	0.7	2.4
		acid	0.002	450	11,250	13,020	13,420	0.7	2.0
			0.0002	450	10,780	12,270	12,770	1.2	1.5
SAP-117	30:1	Varsol	0.02	25–29	25,680	34,630	43,250	6.4	9.3
10.0% Al_2O_3			0.02	450	11,750	13,720	14,050	0.6	2.2
			0.002	450	10,320	12,700	13,190	0.6	1.5
			0.0002	450	8,140	11,750	12,330	0.7	1.1
SAP-65	20:1	None[c]	0.02	25–29	11,110	12,180	18,520	11.7	21.8
0.9% Al_2O_3			0.02	450	1,500	2,420	3,230	3.1	36.9
			0.002	450	1,770	2,280	2,490	2.6	16.7

[a]Billet preheat temperature, 500°C.

[b]Cold pressed and vacuum annealed.

[c]Vacuum hot-pressed as-received powder.

[redacted]

Table 5.6. Short-Time Tensile Properties of SAP Rod Extruded from Ball-Milled and Vacuum Hot-Pressed VMP H-10 Aluminum Powder[a]

Material	Milling Medium	Strain Rate (min^{-1})	Test Temperature (°C)	Yield Strength, psi		Ultimate Tensile Strength (psi)	Elongation, %	
				0.02%	0.2%		Uniform	Total
SAP-128 3.4% Al_2O_3	Varsol + 3% stearic acid	0.02	25–29	19,180	23,290	29,470	8.3	15.3
		0.02	450	7,570	8,890	9,140	0.8	5.1
		0.002	450					
		0.0002	450	6,730	7,880	8,210	0.9	2.4
SAP-138 2.9% Al_2O_3	Varsol + 3% stearic acid	0.02	25–29	21,020	25,560	30,500	6.9	16.2
		0.02	450	7,930	9,910	10,010	0.5	4.8
		0.002	450	7,380	9,190	9,600	0.9	3.0
		0.0002	450	6,630	8,280	8,450	0.6	2.0
SAP-139 6.2% Al_2O_3	Varsol + 3% stearic acid	0.02	25–29	25,020	29,900	37,490	8.2	12.4
		0.02	450	9,680	10,990	11,910	0.8	2.9
		0.002	450	8,860	10,500	11,150	0.9	2.5
		0.0002	450	8,220	10,680	11,180	0.6	0.9
SAP-137 7.1% Al_2O_3	Varsol + 2.5% silicone	0.02	25–29	24,300	31,250	39,800	8.6	13.9
		0.02	450	10,040	11,000	11,750	1.1	3.3
		0.002	450	10,500	11,410	11,490	0.6	2.2
		0.0002	450	8,640	10,070	10,410	0.6	1.2
SAP-136 4.7% Al_2O_3	Varsol + 3% stearic acid	0.02	25–29	21,340	24,490	28,950	6.0	7.7
		0.02	450	6,780	8,190	9,350	0.8	3.1
		0.002	450	6,980	8,500	8,710	0.3	0.9
		0.0002	450	6,140	8,030	8,180	0.5	0.7

[a]Extrusion ratio, 30:1; billet preheat temperature, 500°C.

Table 5.7. Swaging Effects Study on ORNL Ball-Milled Powder Vacuum Hot-Pressed at 600°C[a]

Material	Fabrication History	Strain Rate (min^{-1})	Test Temperature (°C)	Yield Strength, psi		Ultimate Tensile Strength (psi)	Elongation, %	
				0.02%	0.2%		Uniform	Total
SAP-71 MD-X-65 2.5% Al_2O_3	As extruded 20:1	0.02	25–29	17,720	24,160	29,680	11.8	19.2
		0.02	450	7,490	9,220	9,260	0.55	4.5
		0.002	450	5,600	8,310	8,930	0.91	3.3
		0.0002	450	5,600	7,580	8,240	0.70	1.5
	Extruded and swaged[b]	0.02	25–29	15,470	21,400	30,210	11.0	18.7
		0.02	450	7,740	9,510	10,040	1.1	4.9
		0.002	450	7,250	9,650	10,310	0.84	2.8
		0.0002	450	5,920	8,050	8,710	1.4	2.0
SAP-56 VMP H-10 9.5% Al_2O_3	As extruded 20:1	0.02	25–29	22,840	33,640	44,680	7.0	9.5
		0.02	450	10,220	14,180	15,250	0.77	2.1
		0.002	450	8,820	13,030	13,930	0.80	1.4
		0.0002	450	7,980	11,680	12,750	0.70	1.0
	Extruded and swaged[b]	0.02	25–29	23,870	33,330	44,280	7.0	11.5
		0.02	450	11,870	15,340	17,890	1.2	2.9
		0.002	450	10,240	13,460	15,690	1.0	1.9
		0.0002	450	9,560	11,620	12,370	0.82	1.2
SAP-58 101(−325 mesh) 9% Al_2O_3	As extruded 20:1	0.02	25–29	18,770	27,410	34,490	5.9	14.9
		0.02	450	7,740	10,450	11,070	1.7	2.3
		0.002	450	5,430	9,050	10,030	1.1	1.9
		0.0002	450	7,490	8,630	9,200	0.70	0.9
	Extruded and swaged[b]	0.02	25–29	19,750	26,750	34,400	7.7	15.6
		0.02	450	8,570	11,300	11,790	0.77	2.1
		0.002	450	7,830	9,810	10,470	1.1	1.4
		0.0002	450	5,350	8,480	9,220	0.79	0.8
SAP-70 VMP H-3 2.7% Al_2O_3	As extruded 20:1	0.02	25–29	13,150	19,470	26,130	9.8	17.7
		0.02	450	5,520	7,080	7,410	1.0	4.5
		0.002	450	5,360	6,440	6,770	1.3	2.6
		0.0002	450	4,370	5,360	6,060	1.1	1.4
	Extruded and swaged[b]	0.02	25–29	16,900	20,780	31,490	9.3	16.9
		0.02	450	5,260	7,400	7,930	1.5	8.7
		0.002	450	4,940	7,080	7,570	1.1	3.8
		0.0002	450	4,610	6,170	6,910	1.0	2.1

[a]Billet preheat temperature, 500°C.

[b]Extrusion followed by 500°C swaging with 1.9:1 reduction in 10% passes.

The material SAP 101 that was milled with oleic acid as a lubricant showed 30% higher strengths at that oxide level than those milled with stearic acid or silicone (not considering those milled with lifter bars). This agrees with the MD X-65 milled in oleic acid from Table 5.3. These two powders are very similar in starting characteristics and should be expected to behave similarly. There was no strength difference between those milled with stearic acid and silicone.

The incorporation of lifter bars in the ball mill increased the high-temperature strength of VMP H-5 SAP by about 30%. This effect was obtained by using either the aluminum or stainless steel balls.

One VMP H-5 SAP rod (SAP-135) was hot extruded from a cold-pressed billet. Compared to those extruded from the vacuum hot-pressed billets this rod exhibited lower high-temperature strength and ductility. This was also true with the SAP rod from the cold-pressed Albron 101 billet (Table 5.2).

Those VMP H-5 powders milled with stearic acid showed the highest ductility while those milled with silicone showed the lowest. This was not consistently true with the other grades of powder.

In addition to these milling studies, the effects of swaging were studied on the MD X-65, Albron 101, VMP H-3, and VMP H-10 grades of powder. After hot extrusion at a 20:1 reduction ratio, the rods were further reduced 2.8:1 by swaging. The swaging was carried out at 500°C in 10% passes with a 10-to-15-min reheat between passes.

The high-temperature strength and ductility were improved for three of the four powder grades. These increases were observed for all three strain rates studied. The finer size VMP H-3 grade showed the greatest average increase in both strength and ductility (13 and 63%, respectively). The Albron 101 showed some increase in high-temperature strength, but no increase in ductility. The room-temperature properties of all four grades were not appreciably affected by the hot swaging.

Properties of SAP Made From Commercially Milled Aluminum Flake Powders. — A relatively large scatter in strength data for MD-3100 SAP was obtained which seems to be related to the as-pressed billet density; the lower billet densities resulting in the higher strengths. This

relationship is illustrated in Fig. 5.4 with the ultimate tensile strength plotted against the billet density. The data shown are from 450°C tensile tests conducted at the 0.02 min^{-1} strain rate. The same relationship is shown by data from the other strain rates.

A large portion of the scatter noted at the high-density end of the curve can be accounted for by considering the extrusion conditions; that is, the higher extrusion ratios provide higher strengths. A possible relationship is that shown in Fig. 5.5. These data were collected at the 0.02 min^{-1} strain rate at 450°C. Table 5.8 lists the MD-3100 data.

Four of the MD-3100 rods from Table 5.8 were studied for strength variation along their entire length. Specimens from these rods were tensile tested at 0.0002 min^{-1} (1%/hr) strain rate at 450°C. A linear variation of significant magnitude was noted in all four rods. These data are included as Fig. 5.6 and show strength increases as high as 40% along the rod length. The ductility data were consistent for each rod and showed no dependence on position. One rod (SAP-53) showed a linear decrease in strength along its length. As indicated in the figure, this

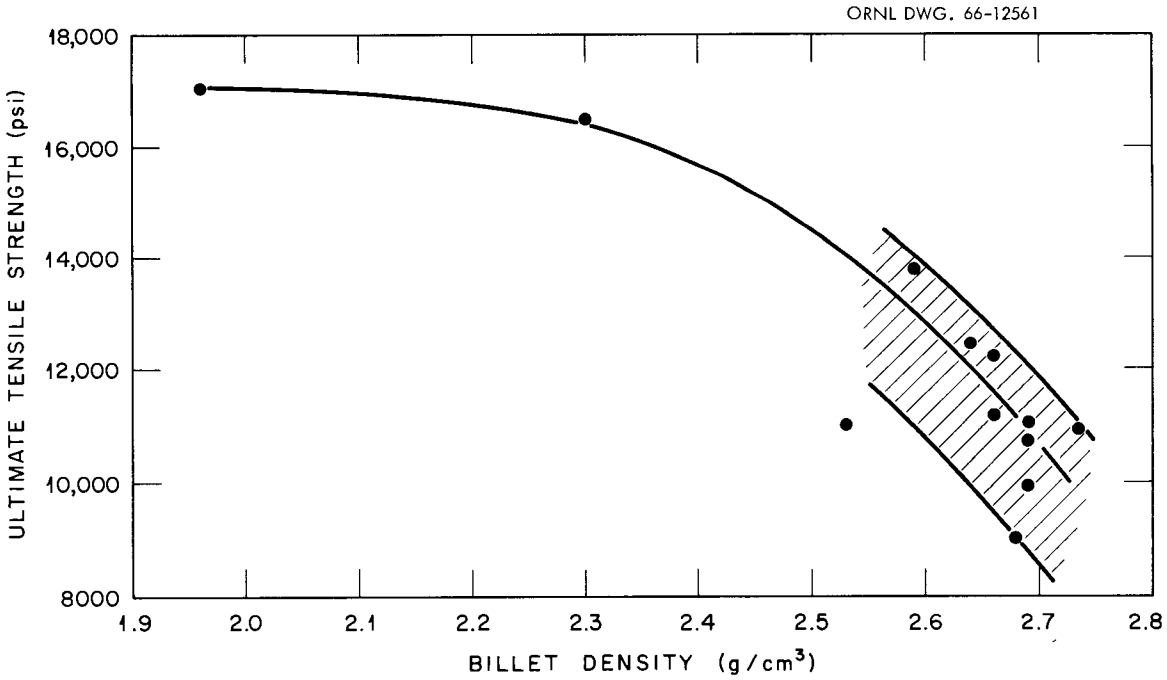

Fig. 5.4. Ultimate Tensile Strength as a Function of Hot-Pressed Billet Density. Tensile tests at 450°C and 0.02 min^{-1} VHP MD-3100 powder (approx 6% oxide).

[redacted]

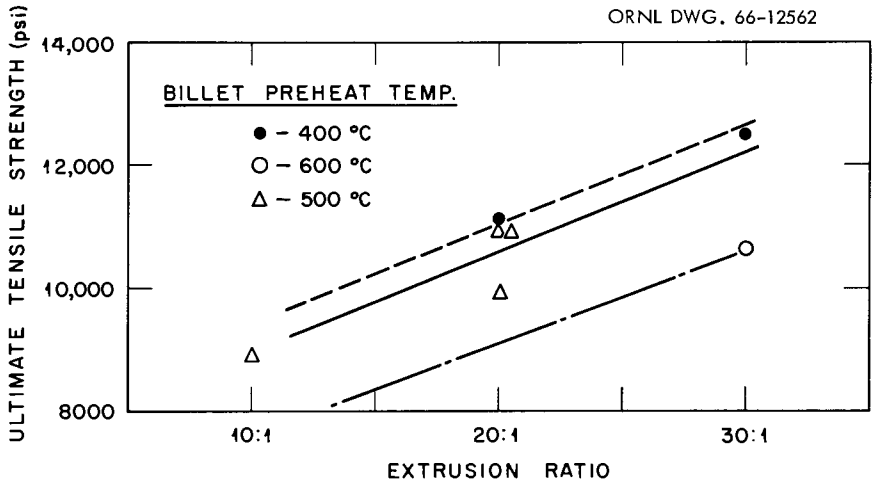

Fig. 5.5. Ultimate Tensile Strength vs Extrusion Ratio for VHP MD-3100 Billets with Densities above 2.6 g/cm^3. Tensile Tests at 450°C and 0.02 min^{-1}.

rod was extruded from a billet that was inserted in a 6061 aluminum can. This was done to accommodate the extrusion of the 2-in.-diam SAP billets in a 3-in.-diam extrusion chamber. Also, this rod could have been mislabeled as to which was the nose end.

We do not know what causes this variation but there are some significant variables that could be changing continuously during the extrusion process:

1. the billet temperature – probably decreases,
2. the extruded rod density – probably increases,
3. the amount of deformation locally,
4. changing flow pattern breaks up oxide particle agglomerates,
5. aluminum-to-oxide interface bonding,
6. the extruded rod texture.

These areas are being explored by posttest measurements on the tensile specimens. Density, texture, and electron transmission work is under way.

Properties of Alcoa 552 SAP. – Two studies were conducted on Alcoa 552 SAP: an extrusion study on vacuum hot-pressed billets and a vacuum treatment study using various treatment routes between powder and extruded rod.

[redacted]

Table 5.8. Extrusion Condition Study on Premilled MD-3100 Powder Vacuum Hot-Pressed at 600°C

Material	Extrusion Ratio	Billet Preheat Temperature (°C)	Strain Rate (min^{-1})	Test Temperature (°C)	Yield Strength, psi		Ultimate Tensile Strength (psi)	Elongation, %	
					0.02%	0.2%		Uniform	Total
SAP-43 ~ 6% Al_2O_3	20:1	400	0.02	25–29	18,740	26,620	36,980	8.1	11.9
			0.02	450	7,420	10,880	11,130	1.0	2.7
			0.002	450	7,170	8,660	9,320	0.84	1.4
			0.0002	450	5,760	7,000	7,900	0.65	0.8
SAP-44 ~ 6% Al_2O_3	30:1	400	0.02	25–29	20,700	28,550	39,570	7.8	11.4
			0.02	450	10,860	12,180	12,430	0.66	2.4
			0.002	450	7,590	9,560	10,220	1.05	1.2
			0.0002	450	6,260	7,410	9,050	0.68	0.7
SAP-53 ~ 6% Al_2O_3	20:1	500	0.02	25–29	17,870	26,470	37,800	9.7	13.3
			0.02	450	8,550	10,600	10,970	0.59	3.3
			0.002	450	7,250	8,590	9,470	1.02	1.7
			0.0002	450	6,260	7,990	8,640	0.64	1.4
SAP-45 ~ 6% Al_2O_3	20:1	600	0.02	25–29	26,430	28,690	39,160	8.2	11.1
			0.02	450	10,880	13,440	13,770	0.52	2.5
			0.002	450	8,390	10,940	11,430	0.73	1.3
			0.0002	450	7,330	9,710	10,290	0.56	0.7
SAP-52 ~ 6% Al_2O_3	30:1	600	0.02	25–29	10,060	25,470	35,990	10.5	13.4
			0.02	450	8,310	10,210	10,620	1.1	2.7
			0.002	450	6,580	7,990	8,560	1.05	1.3
			0.0002	450	6,250	7,730	8,300	0.75	0.8
SAP-39[a] ~ 6% Al_2O_3	10:1	400	0.02	25–29	23,100	32,180	46,040	6.9	8.8
			0.02	450	11,710	15,750	16,490	0.70	1.6
			0.002	450	8,480	11,930	12,350	0.73	1.2
			0.0002	450	9,470	11,190	11,520	0.67	0.7
SAP-131[a] ~ 6% Al_2O_3	20:1	500	0.02	25–29	20,020	30,150	43,920	8.2	9.3
			0.02	450	12,230	16,120	17,020	0.9	1.7
			0.002	450	11,480	14,640	15,060	0.5	1.1
			0.0002	450	11,630	13,450	13,610	0.25	0.3

[a]Low-density billet.

[redacted]

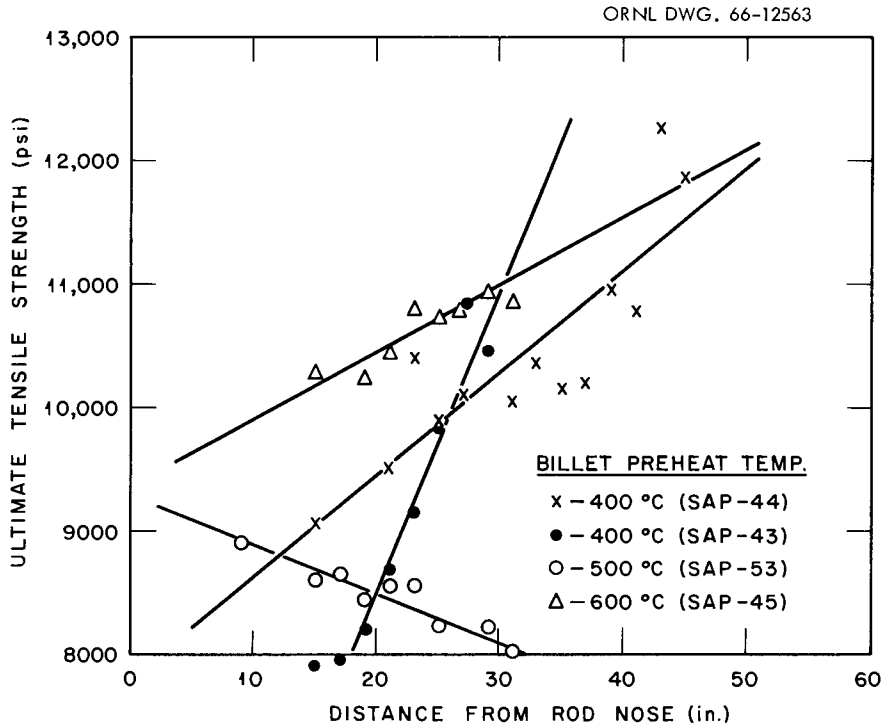

Fig. 5.6. Ultimate Tensile Strength vs Distance Along Extrusion for Vacuum Hot-Pressed MD-3100. Fabricated as shown in Table 5.8. Tensile tests at 450°C and 0.0002 min^{-1} (1%/hr).

The results of these two studies are shown in Tables 5.9 and 5.10. We feel that the high inclusion content of SAP made from this grade of powder is the dominant factor as these two studies were fairly inconclusive. The material did show good high-temperature strength; but this was accompanied by low ductility values. The vacuum hot press followed by a 600°C anneal (SAP-76) did show enhanced ductility at the slow strain rates.

Properties of SAP Made from Special Materials. – The mechanical properties of the rods made from ball-milled filings of the different aluminum alloys are shown in Table 5.11. The 1100 aluminum filings milled to a high oxide content (14%) and showed excellent strength at all test conditions. The ductility was as low as that expected for a commercial SAP of similar oxide content.

All three magnesium-bearing SAP rods showed enhanced room temperature strength. This is due to the effective solid solution strengthening

[redacted]

Table 5.9. Vacuum Treatment Sequence Study on Premilled Alcoa 552 Flake Powder

Material	Extrusion Ratio	Billet Preheat Temperature (°C)	Billet Treatment	Strain Rate (min^{-1})	Test Temperature (°C)	Yield Strength, psi		Ultimate Tensile Strength (psi)	Elongation, %	
						0.02%	0.2%		Uniform	Total
SAP-64 ~ 6% Al_2O_3	20:1	500	Vacuum hot pressed	0.02	25–29	26,040	31,890	41,900	8.2	14.2
				0.02	450	11,740	14,670	15,190	0.88	1.6
				0.002	450	11,320	13,810	14,150	0.56	1.1
SAP-76 ~ 6% Al_2O_3	20:1	500	Vacuum hot pressed then vacuum annealed 17 1/2 hr at 600°C	0.02	25–29	19,820	28,080	37,570	8.0	11.2
				0.02	450	8,940	11,450	11,770	0.59	1.6
				0.002	450	8,700	10,440	10,610	0.59	1.6
				0.0002	450	5,950	8,180	8,920	0.76	1.3
SAP-73 ~ 6% Al_2O_3	15:1	500	Cold pressed, then vacuum annealed 20 hr at 600°C	0.02	25–29	24,350	31,490	41,310	6.4	8.6
				0.02	450	10,950	12,470	12,640	0.47	1.6
				0.002	450	8,960	10,980	11,070	0.49	1.0
				0.0002	450	7,150	9,480	9,980	0.49	0.7
SAP-89 ~ 6% Al_2O_3	20:1	400	Vacuum annealed then vacuum hot pressed	0.02	25–29	23,420	30,570	40,100	8.7	11.6
				0.02	450	10,320	13,100	13,270	0.5	1.3
				0.002	450	10,480	12,450	12,780	0.5	0.8
				0.0002	450	4,920	8,940	9,840	0.6	0.6

Table 5.10. Extrusion Condition Study on Premilled Alcoa 552 Flake Powder Vacuum Hot Pressed at 600°C

Material	Extrusion Ratio	Billet Preheat Temperature (°C)	Strain Rate (min^{-1})	Test Temperature (°C)	Yield Strength, psi		Ultimate Tensile Strength (psi)	Elongation, %	
					0.02%	0.2%		Uniform	Total
SAP-96 ~ 6% Al_2O_3	10:1	400	0.02	25–29	15,660	28,440	40,150	6.09	8.2
			0.02	450	7,260	11,950	12,660	0.77	1.9
			0.002	450	8,810	11,200	11,530	0.55	1.2
			0.0002	450	7,570	10,540	11,360	0.51	0.7
SAP-94 ~ 6% Al_2O_3	20:1	400	0.02	25–29	22,550	30,210	40,330	6.06	9.5
			0.02	450	10,520	13,230	13,560	0.66	1.6
			0.002	450	9,890	12,450	12,780	0.62	1.3
			0.0002	450	8,720	11,360	12,260	0.76	0.9
SAP-95 ~ 6% Al_2O_3	30:1	400	0.02	25–29	21,270	29,430	38,990	6.7	10.3
			0.02	450	10,370	12,590	12,880	0.73	2.1
			0.002	450	9,230	11,950	12,240	0.70	1.4
			0.0002	450	9,880	12,100	12,590	0.66	1.0
SAP-81 ~ 6% Al_2O_3	20:1	500	0.02	25–29	15,320	29,960	41,530	7.3	8.1
			0.02	450	11,070	13,300	13,710	0.7	1.3
			0.002	450	9,850	11,410	11,830	0.55	0.6
			0.0002	450	6,400	8,480	9,470	0.65	0.7
SAP-92 ~ 6% Al_2O_3	20:1	600	0.02	25–29	19,790	27,620	37,180	7.9	10.6
			0.02	450	8,080	11,170	11,540	0.55	1.6
			0.002	450	8,310	10,370	10,700	0.55	1.3
SAP-97 ~ 6% Al_2O_3	30:1	600	0.02	25–29	17,910	26,710	37,220	8.4	11.2
			0.02	450	5,840	10,620	11,240	0.63	1.9
			0.002	450	7,890	10,020	10,350	0.52	1.5
			0.0002	450	6,250	9,860	10,520	0.51	0.9

Table 5.11. Studies on Ball-Milled Metal Filings[a]

Material	Strain Rate (min^{-1})	Test Temperature (°C)	Yield Strength, psi		Ultimate Tensile Strength (psi)	Elongation, %	
			0.02%	0.2%		Uniform	Total
SAP-129	0.02	25–29	30,890	43,410	61,520	6.5	6.5
1100 aluminum	0.02	450	16,780	17,990	20,020	0.56	0.91
14% Al_2O_3	0.002	450	12,140	15,930	16,670	0.63	0.63
	0.0002	450	9,960	14,210	15,060	0.40	0.40
SAP-119	0.02	25–29	32,180	39,150	50,580	7.5	9.2
5052 alloy	0.02	450	7,360	8,680	8,760	0.91	7.5
Al + 2.5% Mg	0.002	450	6,160	7,590	8,110	1.3	4.3
10% oxide	0.0002	450	5,880	7,060	7,660	1.3	3.0
	0.0002[b]	450	5,650	6,690	6,860	1.53	2.50
	0.0002[c]	450	3,870	5,600	6,260	1.3	2.4
SAP-147	0.02	25–29	25,550	33,930	48,580	6.6	6.7
5154 alloy	0.02	450	6,780	7,850	8,610	2.6	7.4
Al + 3.5% Mg	0.002	450	5,730	6,870	7,240	2.2	5.8
6% oxide	0.0002	450	4,950	6,440	6,930	2.3	3.8
	0.0002[b]	450	5,110	6,180	6,350	2.1	3.7
SAP-148	0.02	25–29	25,060	31,430	51,280	8.5	8.9
5056 alloy	0.02	450	2,570	3,060	3,400	4.6	20.1
Al + 5.2% Mg	0.002	450	2,150	2,490	2,820	3.8	8.5
5% oxide	0.0002	450		1,880	2,620	4.5	6.2

[a]Filings milled in varsol + 3% stearic acid and vacuum hot pressed at 600°C; billet preheated at 600°C and extruded at 30:1 ratio.

[b]After aging 70 hr at 450°C.

[c]After aging 70 hr at 450°C and 14.5 hr at 550°C.

of the magnesium addition. Inferior strengths were displayed by these alloys at 450°C, the strength decreasing with increasing magnesium content. This is explained by the increasing milling resistance of the alloyed matrix. The interoxide distance is directly related to the thickness of the milled flake.

The most significant property of these alloys is their good high temperature ductility. This is especially significant at the slow strain rates. Both the uniform and the total elongation values increase with increasing magnesium content.

The uniform elongation as measured in a tensile test is a measure of the work hardening coefficient of the material. Also, this uniform elongation is often an indication of the amount of strain expected during the first stage of creep.

Plasma-Arc Deposition. — The Linde Division of Union Carbide Corporation has prepared for us three SAP tube shells by the plasma-arc deposition process. The tube shells were approximately 80% dense and ranged in oxide content from 2 to 5%.

The tube shells were heated to 500°C for 1 hr and extruded into thin wall tubing. This apparently led to oxide pickup as the extruded tubes contained 6 to 8% Al_2O_3.

The tubes were machined to concentric tubing with the inside surface honed and the outside surface machined to a high luster. Some of these were then sliced into specimen blanks allowing both longitudinal and transverse tensile testing.

The results of the tensile tests are shown in Table 5.12. Room- and elevated-temperature burst tests are planned. One room-temperature burst test already conducted agrees with the transverse strength and ductility.

Microstructural Evaluation (D. G. Harman and K. Farrell)

Microstructures of SAP Made from Atomized Powders. — Because of the fine microstructure of SAP the electron microscope is required for meaningful microstructure studies. Thin foils were prepared from the extruded rod for electron transmission observation.

Table 5.12. Short-Time Tensile Properties of SAP Tubing Prepared by the Plasma-Arc Process

Material	Specification Orientation	Strain Rate (min^{-1})	Test Temperature (°C)	Yield Strength, psi 0.2%	Ultimate Tensile Strength (psi)	Elongation, % Uniform	Elongation, % Total
Linde Tube 1 6.91% Al_2O_3	Longitudinal	0.02	25–29	21,310	29,090	3.8	3.9
		0.02	450	7,050	7,760	0.6	1.3
		0.002	450	6,140	6,590	0.6	0.6
	Transverse	0.02	25–29	26,740	30,220	3.3	3.4
		0.02	450	6,440	6,820	0.6	0.6
Linde Tube 2 5.77% Al_2O_3	Longitudinal	0.02	25–29	24,410	30,590	7.2	7.2
		0.02	450	7,450	8,180	1.2	1.5
		0.002	450	7,080	7,430	0.6	0.6
	Transverse	0.02	25–29	21,110	28,150	2.8	2.8
		0.02	450	3,030	3,030	0.2	0.2
		0.002	450	5,480	5,480	0.2	0.2
Linde Tube 3 7.68% Al_2O_3	Longitudinal	0.02	25–29	23,500	30,500	7.8	9.8
		0.02	450	7,830	7,980	0.6	1.9
		0.002	450	6,820	7,160	0.8	1.3
	Transverse	0.02	25–29	21,820	28,410	8.6	9.8
		0.02	450	5,840	6,300	1.2	1.8
		0.002	450	4,930	5,340	0.4	0.6

The effects of different milling conditions were studied using SAP rods from the H-5 powder. The results can then be correlated with the mechanical properties of these rods.

Microstructures of H-5 SAP rods from four different milling processes are shown in Fig. 5.7. Relative to their respective oxide contents, these rods are shown in order of decreasing strength. This decreasing strength can be associated with the increasing distance between oxide particles or groups of particles.

Rods from VMP H-3 (SAP-122) and VMP H-10 (SAP-137) milled in silicone with about the same oxide content as the similarly milled H-5 powder shown in Fig. 5.7 were examined and found to show the same structure.

Figure 5.8 shows the structure of SAP made from H-3 powder that was milled to 3% oxide in stearic acid. This uniform oxide distribution was seen in all low-oxide rods examined.

Microstructures of SAP Made from Commercially Milled Powders. — Typical microstructures of SAP extruded from these two powder grades as revealed by the optical microscope are shown in Figs. 5.9 and 5.10. These magnifications do not show individual oxide particles but can show stringering, porosity, and inclusions. The high inclusion content of the Alcoa 552 renders it unsatisfactory for organic cooled applications. In contrast the MD-3100 shows a low inclusion content (see Fig. 5.10).

Thin film transmission pictures of the Alcoa 552 SAP are shown in Fig. 5.11. The improved oxide distribution resulting from an extended vacuum treatment prior to extrusion is evident. This improved microstructure probably accounts for the better high-temperature ductility.

Microstructures of SAP Made from Alloy Filings. — The microstructure of the 5.2% Mg alloy is shown in Fig. 5.12. The undeformed matrix shows the poor oxide distribution with "banding" evident. The deformed matrix shows the dislocation tangles usually shown by the parent 5056 alloy. The dislocation tangles result from extensive work hardening.

[redacted]

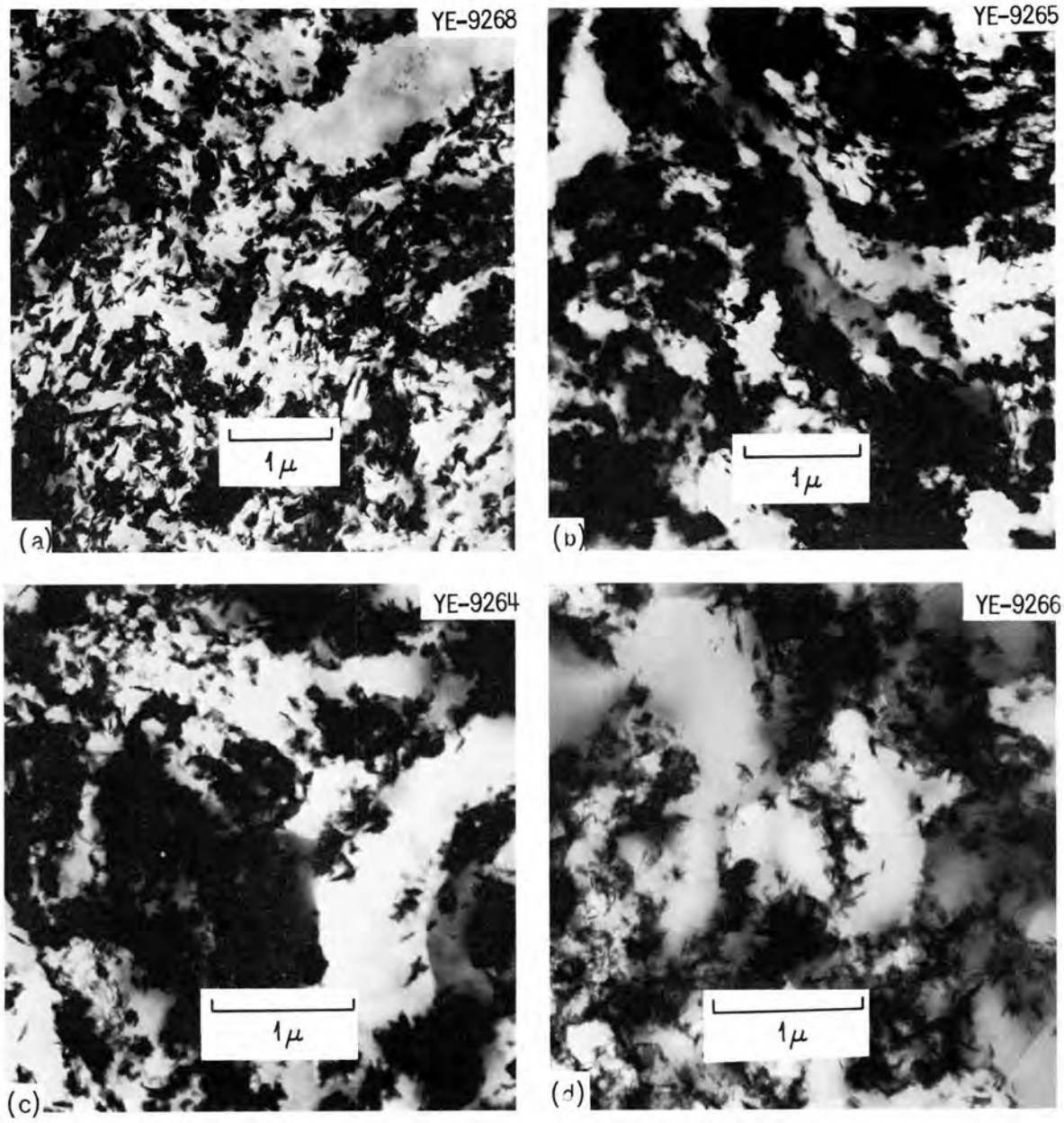

Fig. 5.7. Microstructure of SAP Extruded from Ball-Milled VMP H-5 Powder. In order of decreasing strength (a) 8.0% oxide milled in stearic acid with lifter bars, (b) 7.2% oxide milled in oleic acid, (c) 9.2% oxide milled in stearic acid, and (d) 6.8% oxide milled in silicone.

[redacted]

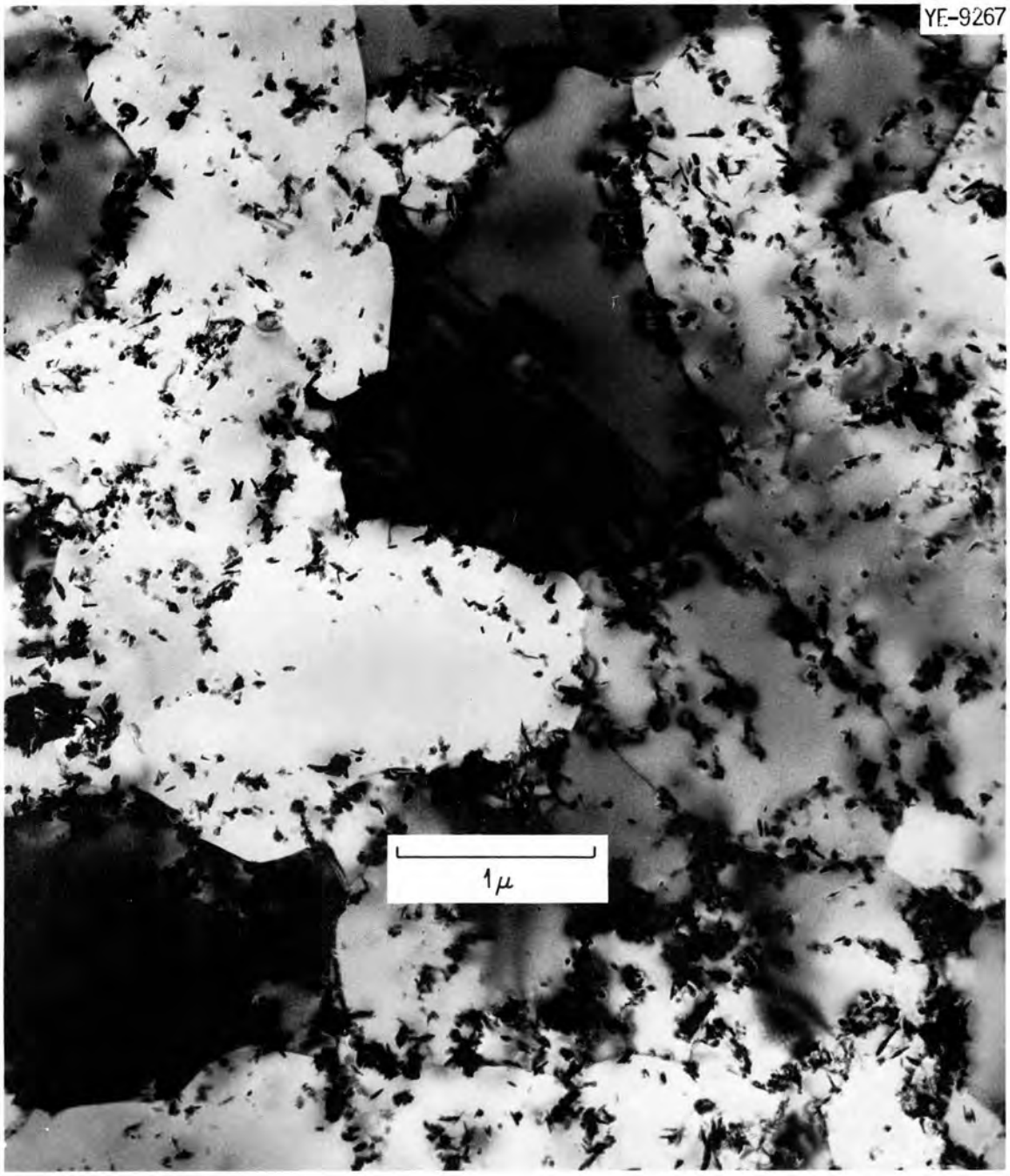

Fig. 5.8. Microstructure of SAP Extruded from Ball-Milled VMP H-3 Powder with 3% Oxide.

[redacted]

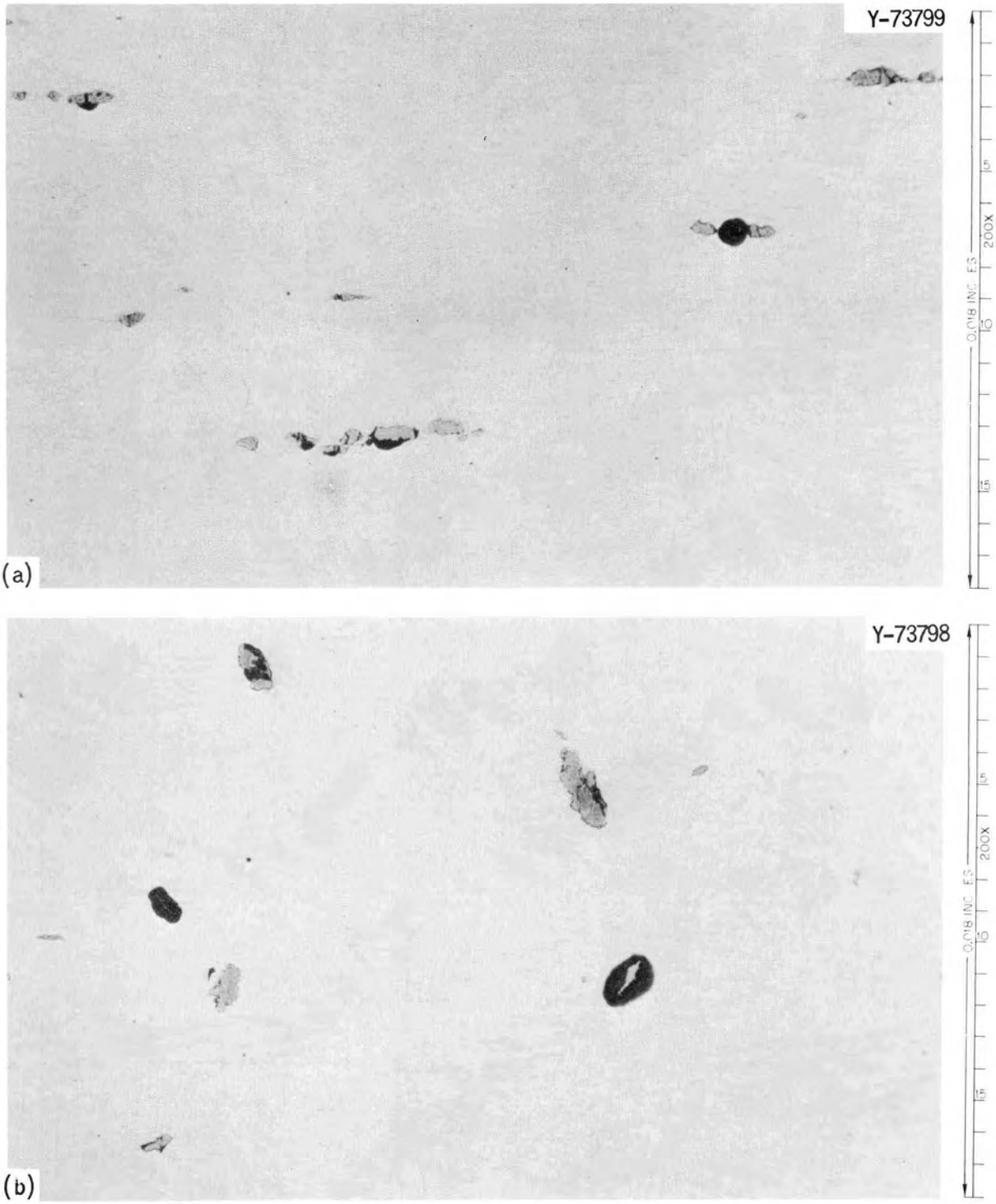

Fig. 5.9. Typical Microstructure of SAP Extruded from Vacuum Hot-Pressed Alcoa 552 Powder. (a) Longitudinal Section. (b) Transverse Section.

[redacted]

[redacted]

Fig. 5.10. Typical Microstructure of SAP Extruded from MD-3100 Powder with Approximately 6% Oxide. Longitudinal Section.

Microstructures of SAP Made by Plasma-Arc Deposition. — The tubes show a stringered microstructure with a few small inclusions. Transmission electron microscopy shows a grain size ranging from one-fourth to several microns with the oxide distributed in the grain boundaries.

Nondestructive Testing Development (J. Luquire[4] and H. Whaley)

We are making feasibility studies on several possible methods for rapidly determining the dimensions of SAP flake material.

The first approach to the problem was an electrical one. An attempt was made at determining the effect on the capacitance of a parallel plate capacitor when a SAP particle was placed between its plates. Theoretical calculations were made with the assumptions that the field between the plates was uniform before the introduction of

[4]Consultant from the University of Tennessee.

[redacted]

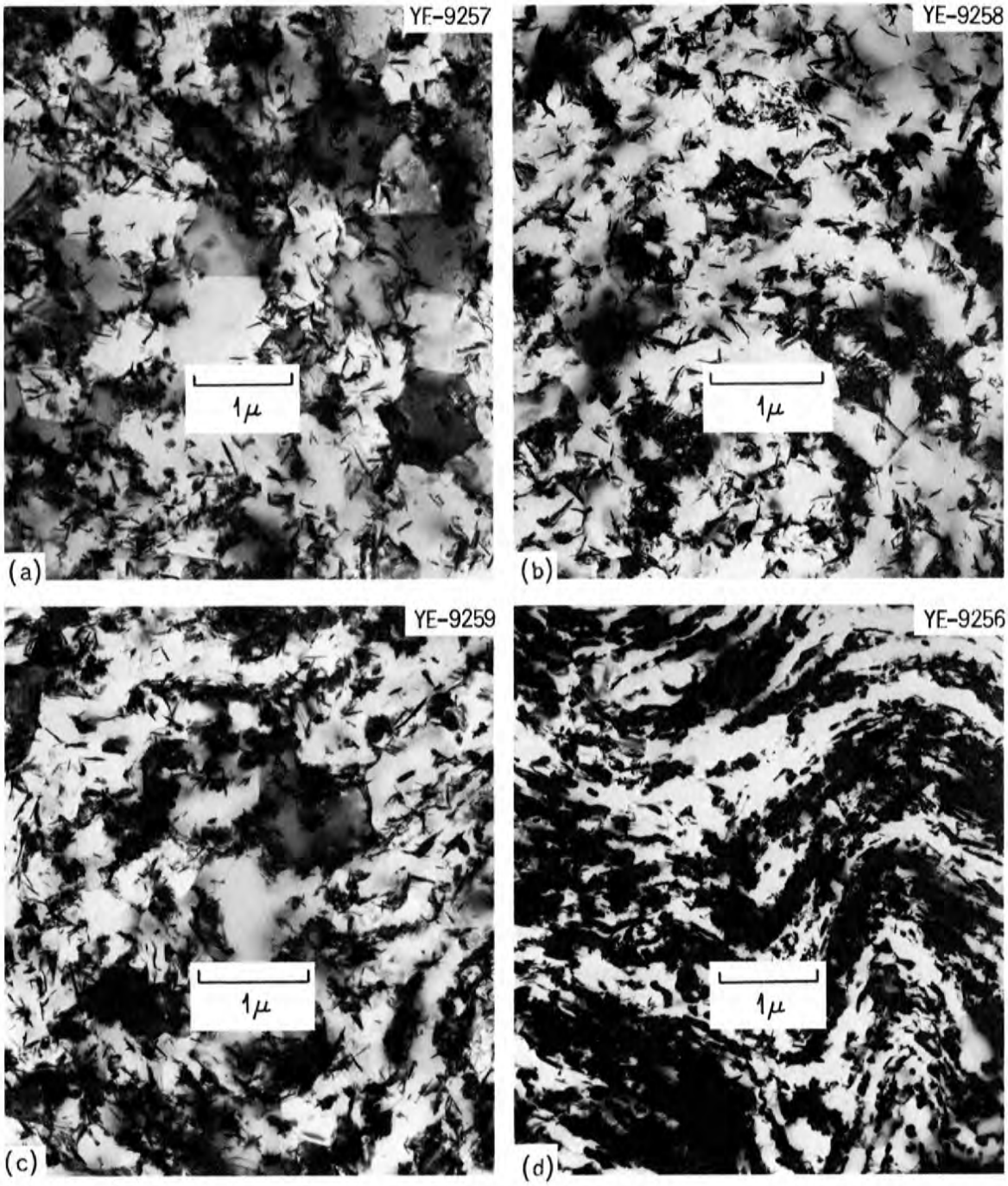

Fig. 5.11. Effect of Vacuum Treatments. Electron microscopy of SAP prepared from Alcoa 552 powder with approximately 6% oxide. (a) SAP-73 cold pressed then vacuum annealed. (b) Vacuum hot pressed then vacuum annealed. (c) Vacuum annealed then vacuum hot pressed. (d) Vacuum hot pressed.

[redacted]

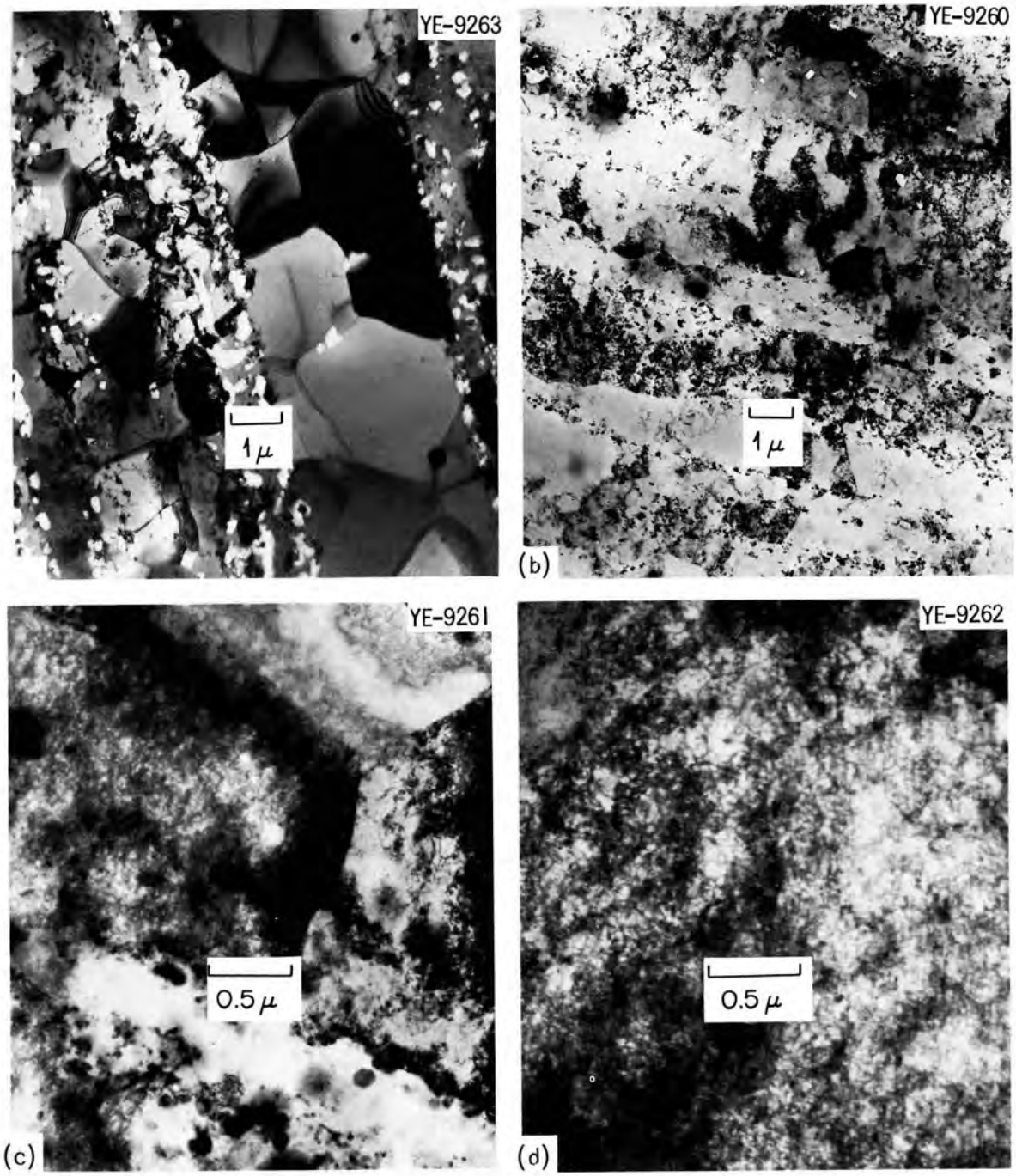

Fig. 5.12. Effect of Deformation on the Microstructure of Al + 5.2% Mg SAP. (a) Undeformed. 16,700×. (b) Deformed. 15,000×. (c) Deformed. 32,500×. (d) Deformed. 57,500×.

[redacted]

the particle and that the particle was an infinitely thin disk. A large scale mockup was then built to check the theoretical calculations. With this apparatus it was found that an aluminum disk was attracted to the plate to which it was originally closer. This problem was remedied by applying an alternating potential to the capacitor plates. It was then found that with a large enough potential difference between the plates the disk would orient itself with a diameter parallel to the field lines, which was as the theoretical calculations predicted for a direct potential. The disagreement of experiment with theory is obviously due to the false assumptions made in the theoretical calculations.

Next, irregularly shaped objects were placed between the plates, and it was found that the long dimensions of the objects oriented themselves parallel to the field lines. At this point, it was decided that better approaches to the problem could be made, since any capacitance change would depend, not only on the size and shape of the particles, but also on the orientation of the particle in the field that could not be effectively controlled.

The most recent approach has been from the standpoint of the effect of size and shape on the terminal velocity of the particles in air. With a few simplifying assumptions, theoretical calculations predict that for flakes the terminal velocity depends upon the $n^{\underline{th}}$ power of the thickness, with $n = 1/2$ or 1. The two values of n arise from the fact that one may assume the drag term in the equation of motion to vary as the velocity to the first power or to the second power. On the basis of these calculations, construction of a settling device was begun. As an aid in designing this apparatus, the terminal velocities of these particles were measured using the Millikan Oil Drop apparatus. When this was done, it was found that an estimated 10% of the smaller particles remained suspended in air. Furthermore, the particles, which were thought to be electrically neutral, were found to be charged both positively and negatively. In addition to the terminal velocities of the SAP particles, the terminal velocities of larger spherical particles were also measured.

The principles of operation of the device are simple. The particles are introduced into a horizontally moving column of air. The point of

introduction is at the upper boundary of the column, which has a square cross section. The particles move horizontally in the air column and very quickly attain the velocity of the moving air. As the particles move horizontally, gravitation causes them to settle at the bottom of the column. Since the thicker particles fall faster, they will reach the bottom first, while the thinner particles move farther in a horizontal direction before settling at the bottom. Thus, at the lower boundary of the column there is a spread of particles, with the thickness of a particle at a particular point being proportional to the distance between that point and the point of introduction.

Although in principle the mechanism is simple, in actual practice some difficult problems arise. One specific problem is that of dispersion of the particles for introduction into the column. Several methods of dispersion were attempted, including the use of nozzles and a Wright Dust Feed. A mechanical sifter was also tried; however, these methods all proved unsatisfactory for various reasons. Finally, a dispersion mechanism, utilizing a circular brush suspended above the powder and rotated at 26,000 rpm, was developed. Thus far this mechanism has proved quite satisfactory as it produces virtually 100% dispersion of the particles.

In addition to the problem of dispersion, there is that of obtaining uniform air flow in the column. At first, the flow was found to be quite turbulent with the turbulence being dependent upon the flow velocity. However, the turbulence was essentially eliminated by allowing the air to pass through baffles, constructed from ordinary drinking straws. By placing a baffle at each end of the column, uniform flow was obtained. With the solution of this problem complete, there remains only the problem of obtaining a relatively small flow velocity.

6. WELDABILITY OF NICKEL-BEARING ALLOYS

G. M. Slaughter

A new program has been initiated to determine the effects of specific elements, individually and combined, upon the cracking behavior and mechanical properties of welds in nickel-bearing alloys. This program has as its ultimate goal the understanding of the metallurgical considerations influencing cracking in welds in these alloys so that sufficient control can be placed over the materials and joining methods to minimize difficulties of this type.

Much of the effort in this reporting period has been aimed at procuring high-purity raw materials and at fabricating special alloys for weldability testing both at Rensselaer Polytechnic Institute under subcontract and at ORNL. Studies directed toward determining the influence of typical minute flaws such as microfissures and microporosity upon the mechanical properties of nickel-bearing alloy welds also were started.

Special Alloy Fabrication

D. A. Canonico R. E. McDonald
W. J. Werner

Raw materials for special alloy fabrication were purchased on the basis of highest purity obtainable at reasonable cost and with acceptable delivery dates. Table 6.1 shows the certified analyses of melting stock currently being used.

The Incoloy 800 composition (Fe–32.5 Ni–21.0 Cr, wt %) was chosen for the first series of special alloys fabricated in view of its current importance for a variety of fuel element and nuclear steam generator applications. Variations in aluminum and titanium contents within the fairly wide range permitted by ASTM were incorporated. These two minor element additions were selected for initial study because of their probable (but undetermined) major influence on weldability, mechanical properties, and aging response. Table 6.2 lists the alloy compositions selected and one-half of them have been processed.

Table 6.1. Certified Analyses of Melting Stock

Impurity Element	Impurity Content of Melting Stock, wt %		
	Fe	Cr	Ni
C	0.005	0.014	0.01
Si		0.007	0.0006
P		0.001	
S	0.004	0.014	
Fe		0.11	0.0006
Cr			0.0003
Cu		0.0005	< 0.001
Pb		0.0013	
Al		0.004	
N	0.001	0.014	
O		0.033	
H		0.0003	
Mn			< 0.001
Co			0.0005

Table 6.2. Special Alloy Compositions

Special Alloy Number	Nominal Composition, wt %				
	Ni	Cr	Al	Ti	Fe
Incoloy 800-1	32.5	21.0	0.00	0.00	bal
Incoloy 800-2	32.5	21.0	0.15	0.15	bal
Incoloy 800-3	32.5	21.0	0.38	0.38	bal
Incoloy 800-4	32.5	21.0	0.60	0.60	bal
Incoloy 800-5	32.5	21.0	0.38	0.15	bal
Incoloy 800-6	32.5	21.0	0.38	0.60	bal
Incoloy 800-7	32.5	21.0	0.15	0.38	bal
Incoloy 800-8	32.5	21.0	0.60	0.38	bal

The elemental components of the special alloys were consolidated by inert-atmosphere arc melting in a double-wall furnace with a tungsten electrode. The resultant 1/2-in.-diam by 12-in.-long ingots were welded into longer cylindrical electrodes for vacuum consumable melting. The ingots of these special alloys were extruded and hot-swaged or hot-rolled to the final desired forms of 3/8-in.-diam rod and 1/2-in. plate.

Weldability Studies

VARESTRAINT Testing Performed Under Subcontract at Rensselaer Polytechnic Institute (W. F. Savage, C. D. Lundin)[1]

The weldability of nickel-bearing alloys is being investigated using the VARESTRAINT test developed at Rensselaer.[2] This VAriable RESTRAINT test, which is new and relatively inexpensive, permits the evaluation of base-metal weldability as well as the determination of the effect of a particular welding process and associated welding variables on hot cracking. The testing procedure is shown in Fig. 6.1. A weld is deposited from left to right, as indicated, using any combination of process, joint geometry, and welding parameters of interest. As the arc passes the point marked A in Fig. 6.1, a massive, pneumatically actuated loading yoke bends the specimen downward suddenly to conform to the radius of curvature of top surface of the removable die block, B. Meanwhile, the arc travels steadily onward and is subsequently interrupted in the runoff area at C.

From the geometry of the system, the nominal value of the suddenly applied, augmented-tangential strain in the outer fibers of the test specimen can be calculated as follows

$$\text{augmented-tangential strain} = \epsilon_t = t/2R$$

where t = specimen thickness and R = radius of curvature of die block.

---

[1]Department of Materials Engineering, Rensselaer Polytechnic Institute, Troy, N. Y. Subcontract is funded jointly with BONUS Core II Superheater R and D.

[2]W. F. Savage and C. D. Lundin, "The Varestraint Test," Welding J. (N.Y.) 44(10), 433-s–442-s (1965).

[redacted]

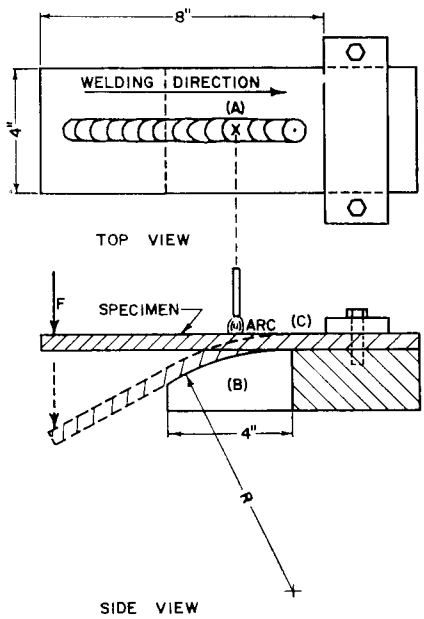

Fig. 6.1. Simplified Sketch of the Operation of the VARESTRAINT Testing Device. (Rensselaer Polytechnic Institute drawing).

Therefore, by substituting a die block with the appropriate radius of curvature, any desired augmented strain can be applied to the weldment at any predetermined instant during weld deposition. Since the magnitude of the augmented-tangential strain is independent of the welding parameters, the effect of welding process, weld composition, and other parameters influencing the microstructural features of the weldment can be isolated from the mechanical effect of externally imposed restraint.

Standard 1/2- × 2- × 12-in. test specimens of commercial heats of Inconel 600, Incoloy 800, and Hastelloy X were tested and evaluated in the initial part of the program. The chemical analyses of the materials are shown in Table 6.3, while the tungsten-arc welding conditions are given at the top of page 95.

[redacted]

Table 6.3. Chemical Analyses of Alloys Studied

Alloy	Heat Number	Chemical Composition, wt %													
		C	Mn	Fe	Co	Ni	Cr	W	Mo	S	Si	Cu	Al	Ti	P
Inconel 600	NX 6794	0.02	0.16	6.7		77.6	15.3			0.007	0.21	0.03	0.29	0.30	0.008
	NX 8206	0.04	0.21	6.6		77.6	15.2			0.007	0.21	0.05	0.07	0.62	0.008
Incoloy 800	HH 1786A	0.04	0.87	45.5		31.5	20.5			0.007	0.57	0.36	0.22	0.41	0.010
	HH 6733A	0.08	0.92	42.7		33.4	21.0			0.007	0.52	0.57	0.35	0.50	0.010
Hastelloy X	2868	0.10	0.60	18.5	1.7	bal	21.7	0.62	9.0	0.004	0.35	0.03	0.30	0.01	0.014
	2865	0.11	0.60	18.0	1.7	bal	22.2	0.57	8.8	0.004	0.29	0.05	0.15	0.01	0.015

Arc current:	340 ± 10 amp
Arc voltage:	11.5 to 12
Arc travel speed:	4 1/2 ipm
Shielding gas:	Argon 35 cfh
Electrode:	1/8 in. 2% thoria, ground to a conical tip with a 90° included angle
Arc length:	0.090 in., measured cold
Polarity:	Straight

Figure 6.2 is a comparison of the generalized sensitivity to hot cracking for the three types of material studied. The data points shown in this figure were obtained by averaging the results (at equivalent augmented strain) of the tests on both heats of the same material. It should be noted from this figure that the cracking threshold (minimum augmented strain to cause cracking) is 1/3% for Hastelloy X and 1/4% for both Inconel 600 and Incoloy 800, indicating a superior hot-cracking resistance for the Hastelloy X material at low strain levels. However, this superiority is lost at all higher levels of augmented strain with Inconel 600 exhibiting a pronounced superiority over both Hastelloy X and Incoloy 800 at augmented-strain levels of 1/2, 1, and 2%. Thus it appears that the commercial Inconel 600 exhibits the greatest overall hot-cracking resistance of the three materials studied and that commercial Hastelloy X and Incoloy 800 are roughly equivalent in hot-cracking behavior.

The average maximum crack length at 2% augmented strain is approximately 50 mils for the Inconel 600 material while the average maximum crack length for the Incoloy 800 and Hastelloy X is in the range of 150 to 180 mils. In general, the maximum crack length at 2% strain has been found to be directly proportional to the range of temperature in which the material is sensitive to hot cracking. Thus the Inconel 600 material exhibits a smaller hot-cracking temperature range than either the Incoloy 800 or Hastelloy X material.

The bar graphs in Fig. 6.3 permit comparison of the heat-to-heat behavior of the materials studied on the basis of the total crack

[redacted]

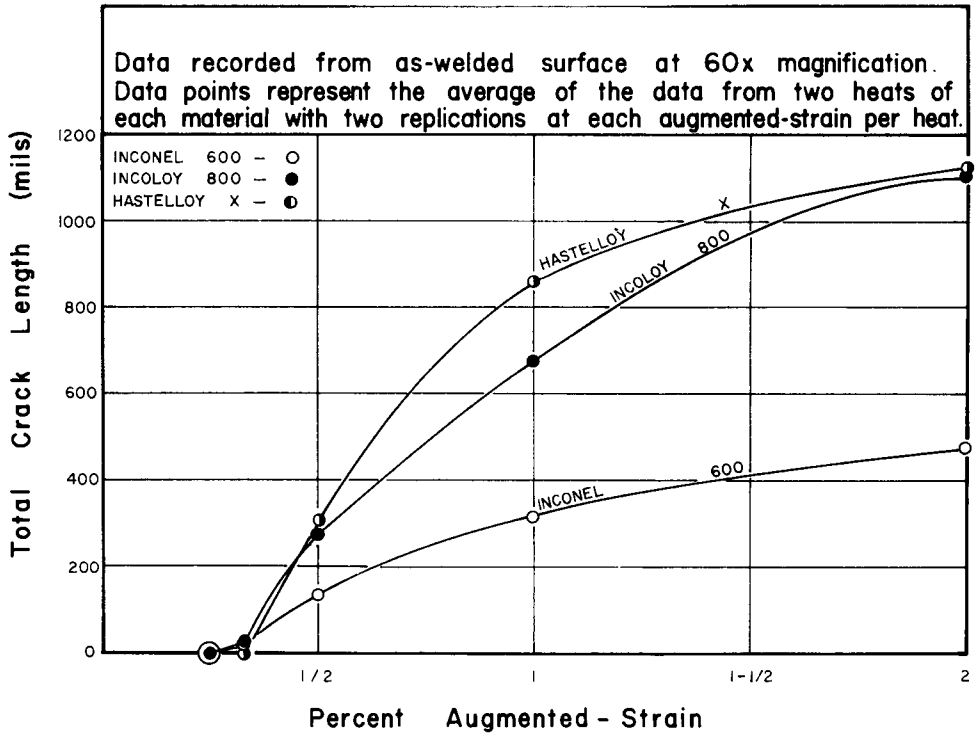

Fig. 6.2. Plot of Total Crack Length vs Percent Augmented Strain. (Rensselaer Polytechnic Institute drawing).

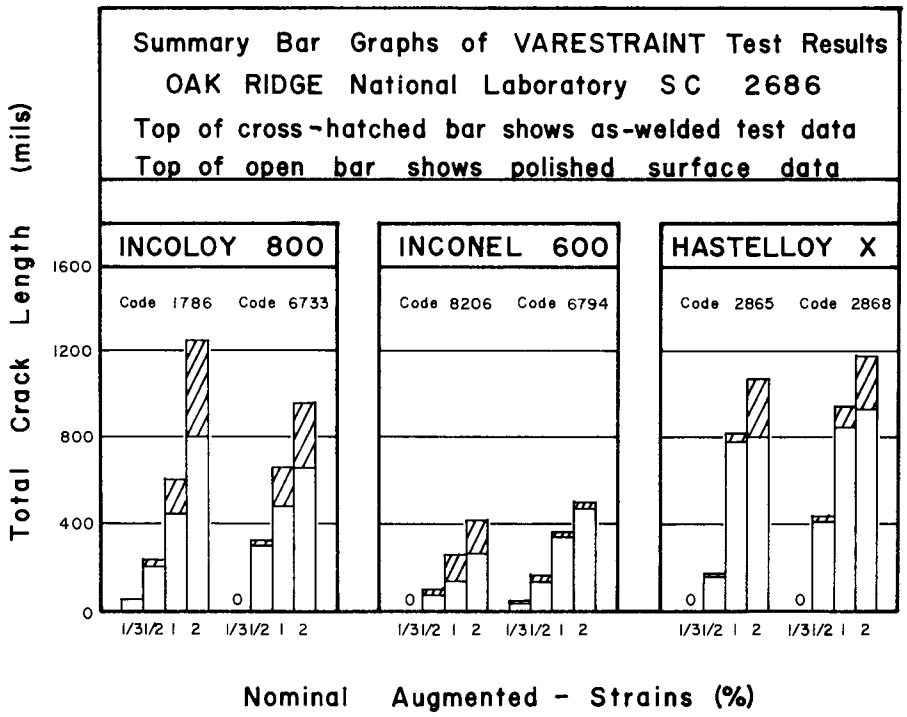

Fig. 6.3. Summary Bar Graphs of VARESTRAINT Test Results. (Rensselaer Polytechnic Institute drawing).

[redacted]

length at equivalent augmented strain. It can be seen from this figure that heat NX 8206 of Inconel 600 is superior to heat NX 6794 at all levels of augmented strain. The two heats of Incoloy 800 tested exhibit similar hot-cracking sensitivity. Heat 1786 showed slightly less cracking than did heat 6733 at 1/2 and 1% augmented strain, while heat 6733 appears to be slightly superior at 1/3 and 2% augmented strain.

Metallographic examination of the polished and etched surface of the VARESTRAINT specimens revealed that the hot cracks formed during testing were invariably confined to the grain boundaries or substructure boundaries produced during solidification. Figure 6.4 shows the appearance of typical fusion-zone hot cracks in Hastelloy X. The relationship between the hot cracks and the solidification substructure can be clearly seen in this figure.

Heat-affected-zone hot cracks were noted only in specimens subjected to a level of 2% augmented strain. Figure 6.5 shows the appearance of a typical hot crack of this type.

All heat-affected-zone cracks were intergranular in nature and were confined to a narrow region (not more than 2 to 3 grain diameters wide) parallel to the fusion line.

Since heat-affected-zone cracking was observed only in specimens that experienced 2% augmented strain and the number of specimens available was not sufficient for testing at higher augmented strain levels, no attempt was made to rate the materials on the basis of heat-affected-zone cracking alone.

The metallographic evaluation of these samples is continuing, and VARESTRAINT testing of experimental alloy compositions vacuum-melted at ORNL is under way.

Hot-Ductility Testing (D. A. Canonico, W. J. Werner)

Each alloy composition will be subjected to hot-ductility tests[3] at ORNL in the Duffer's Gleeble.[4] This test measures the mechanical

---

[3]E. F. Nippes *et al.*, "An Investigation of the Hot-Ductility of High Temperature Alloys," Welding J.(N.Y.)34(4), 183–85 (1955).

[4]Duffers Associates, Inc., Troy, New York.

[redacted]

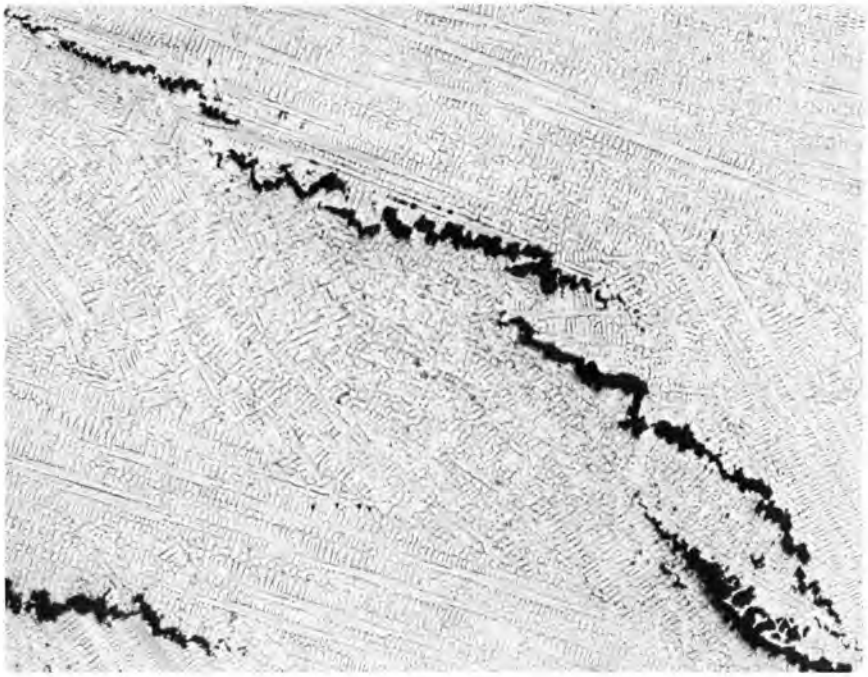

Fig. 6.4. Typical Fusion-Zone Hot Cracking in Hastelloy X. There is an obvious relationship between the hot cracks and the solidification substructure. Etchant: 10% oxalic acid-electrolytic. 100×. (Rensselaer Polytechnic Institute photomicrograph)

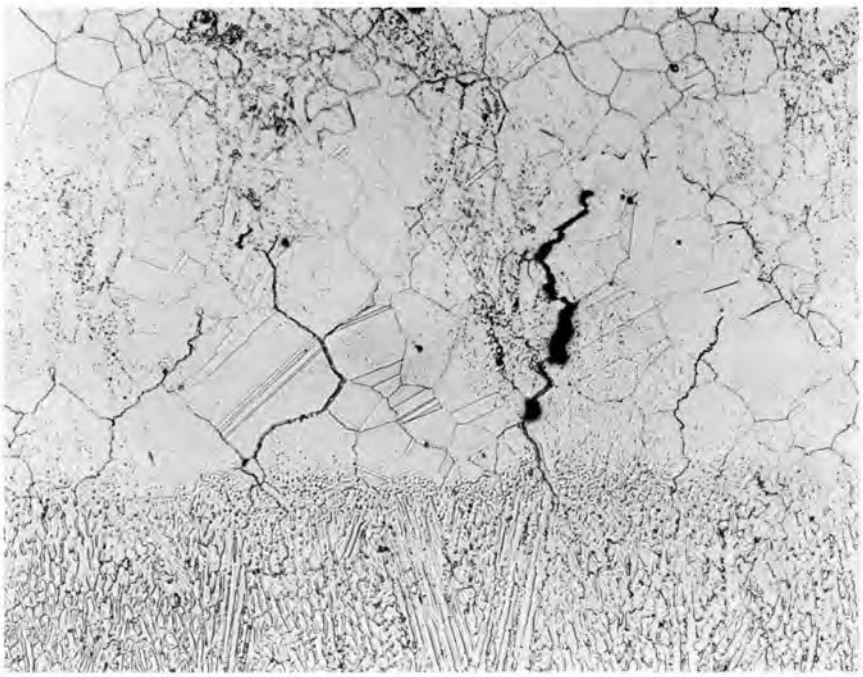

Fig. 6.5. Typical Intergranular Heat-Affected-Zone Hot Crack in Hastelloy X. Etchant: 10% oxalic acid-electrolytic. 100×. (Rensselaer Polytechnic Institute photomicrograph)

[redacted]

properties of heat-affected zones at high temperature and, therefore is a useful test for general welding behavior. For example, the ability of the weld heat-affected zone to withstand stresses without cracking is an indication of suitable weldability.

Influence of Flaws on Properties of Nickel-Bearing Alloys (D. A. Canonico, R. W. Swindeman)

A study is under way to determine the influence of occasional minute flaws, such as microfissures or microporosity, upon the low-cycle fatigue properties of welds in nickel-bearing alloys. The conventional tensile test has been shown to be quite insensitive to weld defects;[5,6] however, preliminary tests at ORNL suggest that failure in fatigue tests was associated with microscopic weld flaws. Some of the initial results of this study are reported here.

Figure 6.6 is a photograph of the fracture surface of a fatigue specimen machined from a stainless steel weld that was tested at 1200°F at a strain level of 0.006 in./in. The failure in this specimen is in weld metal and was initiated at two microscopic defects: A (a surface flaw) and B (an internal flaw). Three other flaws (C, D, and E), which are not failure initiation sites, also can be seen. It has not been established when these noncontributory flaws were generated.

The effect of very small defects on fatigue life is also under study. Figure 6.7 shows the comparative behavior of a weld containing these flaws and sound base metal. The weld specimens were postheat treated in hydrogen at 1010°C to improve their overall fatigue behavior.[7] It is evident that the effects of the flaws are nebulous. The base metal and weld both had about the same life.

---

[5]J. W. Bradley and R. B. McCauley, "The Effects of Porosity in Quenched and Tempered Steel," Welding J.(N.Y.) 43(9), 408-s–414-s (1964).

[6]D. J. Logan, "Effect of Tungsten Inclusions on the Efficiency of Aluminum Alloy Weldments," paper presented at National Fall Meeting, American Welding Society, St. Louis, Missouri, October 3–6, 1966.

[7]D. A. Canonico and R. W. Swindeman, Metals and Ceramics Div. Ann. Progr. Rept. June 30, 1966, ORNL-3970, pp. 189–90.

[redacted]

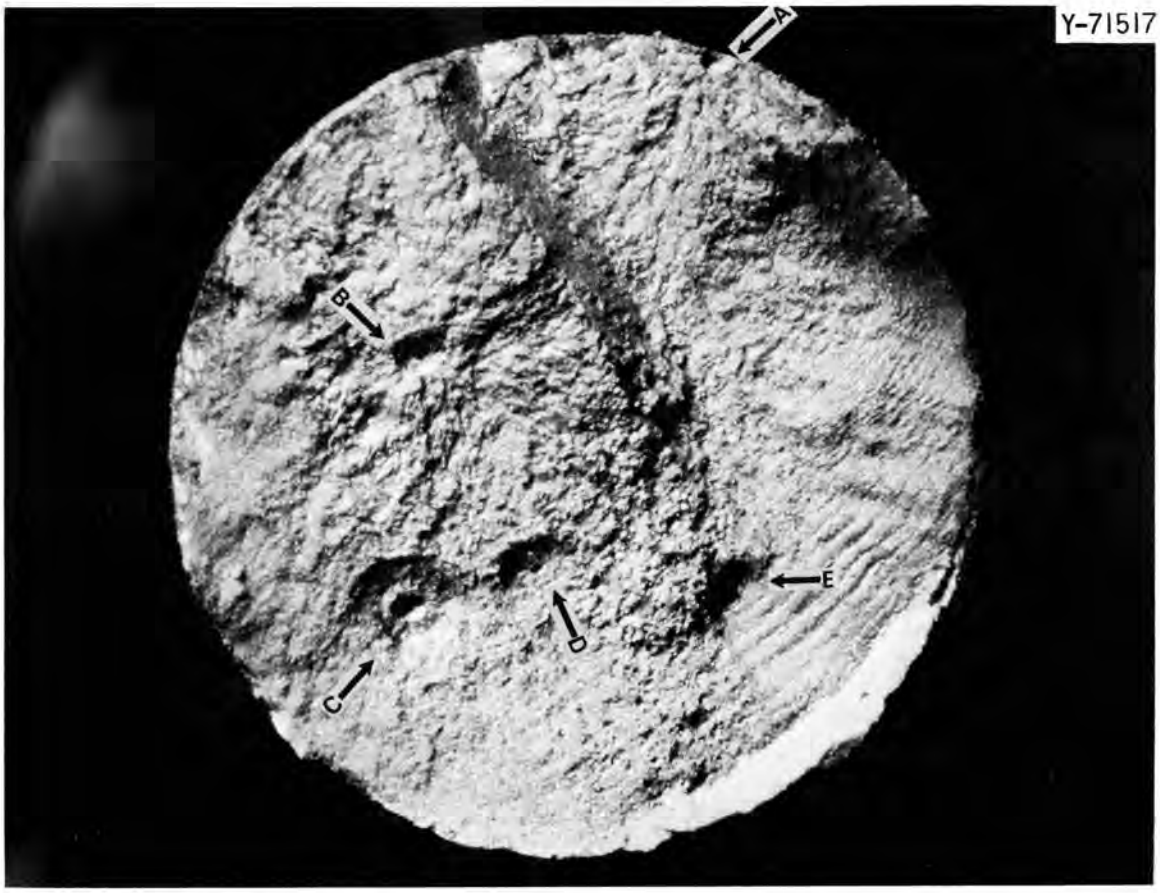

Fig. 6.6. Fracture Surface of a Fatigue Specimen from a Stainless Steel Weld. The failure initiated at microscopic flaws A and B. Non-contributory flaws C, D, and E are evident also. 16×.

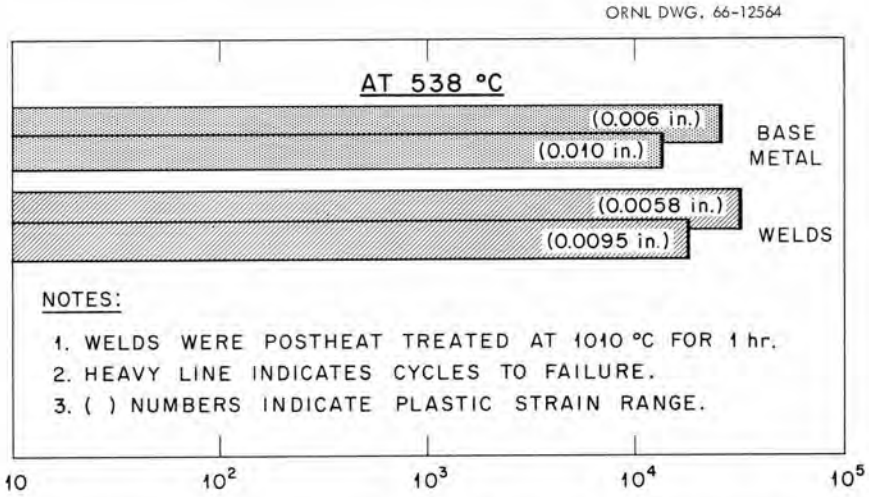

Fig. 6.7. Comparative Fatigue Life of Base Metal and Welds at Two Strain Levels. The welds were postweld heat-treated to improve their general fatigue behavior.

[redacted]

[redacted]

This technique for producing and evaluating microscopic defects in weld metal will be pursued. We will attempt to use nondestructive methods to detect initiation of flaws during the fatigue tests.

[redacted]

[redacted]

PART II.

REACTOR CHEMISTRY DIVISION

[redacted]

[redacted]

FISSION-GAS RELEASE AND PHYSICAL PROPERTIES OF FUEL MATERIALS DURING IRRADIATION

R. M. Carroll R. B. Perez[1]
J. G. Morgan O. Sisman

A hollow-cylinder specimen of single-crystal UO_2 is being irradiated for the purpose of measuring thermal conductivity and fission-gas release during irradiation. In these experiments the specimen is oscillated sinusoidally in the reactor so as to oscillate the neutron flux and thus oscillate the fission rate in the specimen in a sinusoidal manner. The specimen temperature, measured by axial thermocouples, will also oscillate in response to the changing fission power. The base specimen temperature can be controlled by air cooling the outside of the specimen capsule.

Fission-Gas Release

The second-approach mathematical model for fission-gas release has been placed in computer code. Fission-gas release measurements have been made during six series of temperature and fission-rate oscillations for the purpose of testing the codes. We are in the process of developing the methods for converting the data tapes into the parameters to fit into the model. No results have been obtained as yet.

Thermal Conductivity of UO_2 During Irradiation

The general principle of thermal conductivity during irradiation by use of the oscillation technique was explained previously.[2] Namely, the heat production of the UO_2 single-crystal specimen is oscillated by moving the specimen capsule in a sinusoidal motion in the reactor neutron flux. The fission rate, and thus the heat production within the specimen, responds instantaneously to the change of neutron flux;

---

[1]Consultant from the University of Florida.

[2]R. M. Carroll, J. G. Morgan, R. B. Perez, and O. Sisman, Fuels and Materials Development Program Quart. Progr. Rept. June 30, 1966, ORNL-TM-1570, pp. 85–95.

[redacted]

however, the temperature does not. If the oscillations are so rapid that the temperature does not have time to reach its maximum value, then the amplitude of the temperature oscillations will decrease as the oscillation frequency increases. The time delay or phase shift between the neutron flux oscillations and the resultant temperature oscillations will also change with frequency. The phase shift and amplitude relation of the temperature oscillations of the specimen in comparison to the neutron-flux oscillations at various frequencies will both yield data to determine the thermal conductivity of the specimen.

We are evaluating some data obtained while the specimen was at three different neutron-flux levels and three temperatures at each neutron flux. The evaluation is still not complete but we can see some rather definite trends. The thermal conductivity is lowered by increasing the fission rate at a given temperature. The change of thermal conductivity with temperature does not follow the same pattern as for UO_2 measured out-of-reactor. That is, nonirradiated UO_2 has a thermal conductivity that decreases as the temperature increases, at least when the temperature is below 1200°C. During irradiation, the thermal conductivity increases with temperature up to about 900°C, then decreases with further increase in temperature.

The main purpose of the thermal conductivity experiments was to see if fissioning in the fuel would have an effect on thermal conductivity. It is known that accumulated radiation damage can lower the thermal conductivity of various ceramic materials.[3] However, part of the radiation damage will be annealed during irradiation at elevated temperatures. It seems likely that if the accumulated radiation damage can lower the thermal conductivity of UO_2 then the simultaneous damage-annealing process will also lower the conductivity. We were able to test this concept by irradiating at different fission rates while the specimen temperature was controlled over the same temperature range. We found that increases in fission rate invariably resulted in a decrease of thermal conductivity.

---

[3]B. Lustman, "Irradiation Effects in Uranium Dioxide," p. 471 in Uranium Dioxide: Properties and Nuclear Application, ed. J. Belle, Naval Reactors, Division of Reactor Development, USAEC, Washington, 1961.

Our measurements of thermal conductivity are consistent with the concept that disorder lowers the thermal conductivity. When the temperature of the specimen is changed (for example from 600 to 700°C) while at a constant fission rate, two different processes would be in competition to determine the change of thermal conductivity: (a) the conductivity of the undamaged matrix would decrease as the temperature was increased and (b) the increased temperature would raise the conductivity by reducing the accumulated radiation damage. When the temperature is increased from 600 to 700°C the thermal conductivity increases because annealing the radiation damage is the dominant process. At temperatures higher than about 900°C the equilibrium amount of damage is small enough so that the change in conductivity caused by the increase in temperature will result in a net lowering of the conductivity.

In searching for the effect of simultaneous fissioning on thermal conductivity, it was necessary to cover a wide range of fission rates and temperatures. Thus, data are scanty in the temperature regions where the thermal conductivity reaches a maximum. We are now obtaining additional data in this temperature region (700 to 1000°C).

General Theory

We would like to correct several errors in the previous report.[4] A change in the boundary conditions used to derive the thermal conductivity transfer function has resulted in a change in the expression P_o. Using the correct boundary condition stated in Eq. (17) (ref. 5), results in a change in Eq. (14) (ref. 6). It should read:

$$P_o = \frac{2}{(\alpha a)\, J_1(\alpha a)\left[1 + \left(\frac{J_o(\alpha a)}{J_1(\alpha a)}\right)^2\right] \omega_c} .$$

[4]R. M. Carroll, J. G. Morgan, R. B. Perez, and O. Sisman, Fuels and Materials Development Program Quart. Progr. Rept. June 30, 1966, ORNL-TM-1570, pp. 88–93.

[5]Ibid., p. 89

[6]Ibid., p. 88.

This in turn corrects expression (30) (ref. 7) to read:

$$(\alpha a)\ J_1(\alpha a)\left[1 + \left(\frac{J_0(\alpha a)}{J_1(\alpha a)}\right)^2\right] = \frac{2}{P_0\omega_c} \quad .$$

In all expressions containing ρ, with the exception of the definition of η, the ρ should be replaced with ψ (phase shift).

Thermocouple Transfer Function

The thermocouple measuring the temperature of the sample during the in-reactor experiment has in itself a temperature response lag. In order to determine the thermocouple response as a function of frequency and temperature, we started a series of bench experiments in which the period of oscillation was varied between 14 and 925 sec at an amplitude of 40°C. It soon became evident that this was a very time-consuming experiment both from the standpoint of operation and data analysis.

We now are determining thermocouple response characteristics by the use of a pulse method. Here the temperature of the thermocouple is raised very rapidly from temperature A to temperature B and the resulting approach curve to the new equilibrium temperature analyzed. A spring-driven plunger assures us that the elapsed time that the thermocouple travels between the two temperature points in the furnace is very small. Thus from one properly executed pulse test the same information can be obtained as that from an entire series of direct frequency response tests, because the pulse excites the system with all frequencies at once. The desired frequency response is extracted by appropriate methematical processing of the output data. For these tests we use the "millisadic facilities" of the Instrumentation and Controls Division;[8] relaying, by telephone lines, our output data into magnetic

---

[7] Ibid., p. 93.

[8] R. K. Adams, Instrumentation and Controls Div. Ann. Progr. Rept. Sept. 1, 1964, ORNL-3782, p. 78

tape through a digital converter. As many as 400 data points per second can be recorded but usually not this many are required. From the magnetic tape, the information is recorded on punched cards for computer analysis. A code using the derivations by E. M. Grabbee et al.[9] is used to extract the frequency response and phase angle data.

Modification of Experimental Procedure

Because of the successful application of the pulse method to determine thermocouple response, we are modifying our in-reactor experiment to use this technique also. Our savings in time for execution and data analysis will be even greater because of the longer cycle periods required. An auxiliary displacement system is being constructed that will allow the sample to be moved quickly over a small increment of flux and temperature. Continuous position and temperature readout will be transmitted to the "millisadic facility" during the pulse and resulting temperature change.

Response of UO_2 to Electrical Potentials

We have previously described the unusual electrical responses from the UO_2 specimen when an experiment was performed to see how electrical fields would affect fission-gas release.[10] In summary, we found that when an electrode located inside a hollow cylinder of single-crystal UO_2 was given a direct-current potential in relation to a foil surrounding the specimen, the specimen would somehow store and slowly release electrical energy. During the time the energy was stored, a spurious emf was induced in nearby thermocouples to such an extent that the temperature recorders were often driven off-scale.

---

[9] E. M. Grabbee, S. Ramo, and D. E. Wooldridge, Handbook of Automation, Computation, and Control, vol. 1, Wiley, New York, 1958.

[10] R. M. Carroll, J. G. Morgan, R. B. Perez, and O. Sisman, Fuels and Materials Development Program Quart. Progr. Rept. June 30, 1966, ORNL-TM-1570, pp. 75–95.

We were concerned about two aspects of this phenomenon, the spurious temperature indications from the capsule and the nature of the energy storage. Especially, we were concerned that spontaneous potentials could result in false temperature indications. The reactor safety personnel were also concerned about possible false temperature measurements and, with their cooperation, the experiment alarm system was disconnected from the reactor setback during the test intervals (otherwise the spurious signals would result in a reactor setback).

From the tests we have concluded that the thermocouples do give the correct temperature indications if there has been no external electrical potential applied to the specimen within the previous several days. We have been able to apply potentials to the specimen and still observe the spurious emf more than 24 hr later. The direction of the emf depends on the polarity of the initial charge. The time required for the spurious emf to die off depends on the time-voltage product of the initial charge, and grounding one leg of the thermocouple had no apparent effect.

The observations from our tests are summarized below.

1. The electrical storage and response of the system are not affected by the polarity of the electrical field except that the polarity of the specimen changes with that of the field.

2. The atmosphere surrounding the specimen has no effect. The same electrical responses were obtained with a vacuum as with a helium atmosphere.

3. The temperature of the UO_2 had no apparent effect on the electrical response over temperatures ranging from 200 to 1150°C.

4. The fission rate in the UO_2 had no apparent effect on the electrical response.

5. The length of time required for the electrical response to die off was proportional to the time-voltage product of the initial charge. We did not discover the upper limits of this response, but the effects of a 10-v potential applied for 5 min could be detected for more than 24 hr.

6. Grounding all the wires leading into the system did not affect the time required for the response voltage to drain off.

[redacted]

From the above observations we can conclude that the UO_2 single crystal is responsible for the electrical storage rather than any capacitive effects in the capsule or ion collection from the gas. Some out-of-reactor experiments are planned to try to ascertain the reasons for these effects.

[redacted]

PART III.

SOLID STATE DIVISION

IRRADIATION EFFECTS ON ALLOYS AND STRUCTURAL MATERIALS

D. S. Billington, M. S. Wechsler, and J. T. Stanley

The major emphasis of research in the Radiation Metallurgy Section is the study of radiation-hardening and radiation embrittlement in the bcc metals and alloys. These metals have in common the tendency toward low-temperature brittleness which can be characterized by the ductile brittle transition temperature. The increase in ductile-brittle transition temperature upon irradiation is of concern in reactor technology because of the possible catastrophic failure of reactor pressure vessels in service. The work described in this report shows the influence of metallurgical variables, i.e. internal structure such as grain boundaries and distribution of various phases as determined by heat treatment, in determining the response of a steel to irradiation hardening. Of course this is a very complex problem and in order to study certain aspects it is necessary to work with somewhat simpler systems than pressure vessel steel. High purity iron polycrystalline specimens and high purity niobium single crystals are being used to study dislocation motion and interaction with radiation produced defects. Since the interaction of interstitial impurities with radiation produced defects may play an important role in radiation hardening mechanisms, studies of these interactions are being made.

Radiation Effects on Pressure-Vessel Steels

R. G. Berggren W. J. Stelzman
T. N. Jones

Previous reports showed that synthetic heat-affected-zone samples of ASTM A-212B steel may have a considerably higher ductile-brittle transition temperature than the base plate,[1] that the radiation-induced increase in transition temperature was approximately the same for base

[1] R. G. Berggren, W. J. Stelzman, and T. N. Jones, "EGCR Pressure-Vessel Surveillance Program," Radiation Metallurgy Section Solid State Division Progress Report, August, 1965, ORNL-3878, p. 62.

plate and heat-affected-zone samples,[2,3] and that the post-irradiation thermal recovery of transition temperature differed for base plate and heat-affected-zone samples.[3]

Plates from three heats of ASTM A-212B, carbon-silicon steel are being studied. Two of these plates are from heats (A-2110 and A-2056) used in fabrication of the EGCR pressure vessel. The chemical compositions of these three plates are almost identical (Table 1). All three plates were aluminum treated according to fine-grain practice, normalized at 1625-1675°F, water spray cooled to 500°F, and stress relieved at 1200-1250°F. Differences in tensile properties (Table 1) and Charpy V-notch transition temperature (Table 2, lines 1, 4, and 7) are probably due to variations in heat treatment of the plates since micrographs of these plates show differences in ferrite grain size. Samples from each of the three plates were subjected to one of several weld heat-affected-zone

[2] R. G. Berggren, M. S. Wechsler, and T. N. Jones, "Brittle Fracture of Irradiated Structural Metals," Solid State Division Annual Progress Report, October 31, 1963, ORNL-3213, p. 39.

[3] R. G. Berggren, W. J. Stelzman, and T. N. Jones, "Radiation Effects on Pressure-Vessel Steels," Radiation Metallurgy Section Solid State Division Progress Report, February, 1966, ORNL-3949, p. 2.

Table 1. Mill Report on Three ASTM A-212 Grade B Steel Plates

SSD Item No.	147	156	157
Heat No.	15900	A-2110	A-2056
Thickness	4 in.	2 3/4 in.	2 3/4 in.
Carbon	0.25%	0.25	0.27
Manganese	0.74	0.72	0.70
Phosphorus	0.013	0.015	0.012
Sulphur	0.025	0.034	0.032
Silicon	0.20	0.19	0.20
Yield Strength	50,800 psi	50,000 psi	45,200 psi
Ultimate Tensile Strength	83,300 psi	80,500 psi	75,900 psi
Elongation in 2"	28%	30%	28%

[redacted]

Table 2. Simulated Weld Heat-Affected Zone Thermal Cycles for ASTM A-212 Grade B Steel Specimens. Welding Parameters Simulated by Weld Heat-Affected-Zone Thermal Cycles and Ductile-Brittle Transition Temperature (DBTT) for ASTM A-212B Steel Samples.

Material (SSD Item No.)	Energy Input (joules/in)	Welding Parameters Peak Temp. (°F)	Cooling Rate at 1300°F (°F/sec)	Cooling Rate at 1000°F (°F/sec)	DBTT at 20 ft-lb (°C)
147 (Base plate)	--	--	--	--	−20
147-4B HAZ	50,000[a]	2400	83.4	43.8	−18
147-2B HAZ	100,000[a]	2400	31.9	13.6	60
156 (Base plate)	--	--	--	--	−9[c]
156-2 HAZ	95,800[b]	2400	50.0	22.0	7
156-3 HAZ	145,500[b]	2400	23.5	9.5	8
157 (Base plate)	--	--	--	--	5
157-2 HAZ	95,800[b]	2400	50.0	22.0	40[c]
157-3 HAZ	145,500[b]	2400	23.5	9.4	42[c]

[a]Energy input-thermal cycle data for 1 in. plate. Specimens from 4 in. plate given same thermal cycles.

[b]Energy input-thermal cycle data for 2 in. plate. Specimens from 2 3/4 in. plate given same thermal cycle.

[c]Reported by Rensselaer Polytechnic Institute.

[d]All specimens post-heat treated 1150°F for 4 hrs.

[redacted]

thermal cycles as presented in Table 2. All samples were given a "stress-relief" heat treatment after the thermal cycling treatment. The resulting ductile-brittle transition temperatures are also presented in Table 2. The resulting microstructures are presently being studied by light and electron microscopy.

Several irradiation experiments have been completed since the last report[3] and the results of these experiments and those previously reported are presented in Table 3 and Figure 1. In the previous report approximate fast neutron doses were reported. Dosimetry data are now available and are used in the present report. Two irradiation experiments have been completed in the ORR and testing is in progress, two experiments are presently in the ORR, one experiment is ready for insertion in the ORR, and two experiments are presently being built for exposure in the ORR.

The results on the effect of fast neutron dose and irradiation temperature on Charpy V-notch transition temperature of ASTM A-212 Grade B base plate and heat-affected-zones are presented in Table 3. The similarities in the transition temperature shifts for specimens of base plate and heat-affected-zones irradiated at 70°C is again shown. A similar comparison for irradiation at higher temperatures is not possible with the data presently available. However, the data do show that for irradiation temperatures of 260°C and above, the radiation-induced transition temperature shift was less than for lower temperature irradiations.

The effect of post-irradiation annealing on the transition temperature, yield strength, and ultimate tensile strength of base plate specimens (SSD Item No. 15) irradiated at various temperatures is shown in Figure 1. Additional data on tensile properties of this steel are presented in Table 4. For these specimens there was little or no recovery of the radiation-induced transition temperature shift for annealing temperatures below 300°C. This is in contrast with previously reported results[3] for base plate and heat-affected zone specimens from a different heat of ASTM A-212 Grade B steel irradiated at 70°C. In this case considerable recovery of the transition temperature shift was observed after two hour anneals at 300°C. Apparently the different response to post-irradiation annealing is due to the different irradiation temperatures,

Table 3. Effect of Irradiation Temperature and Dose on Charpy V-Notch Ductile-Brittle Transition Temperature of ASTM A-212 Grade B Base Plate and Heat-Affected-Zone Specimens

SSD Item No.		147	147	147	156	156	157
Thermal Cycle		None	4B	2B	2	3	None
Cooling Rate at 1000°F			44°F/sec	14°F/sec	22°F/sec	9.4°F/sec	
Irradiation Temp. (°C)	Dose (E > 1 Mev)	DBTT at 20 ft-lb, (°C)					
	(x 10^{18} n/cm^2)						
--	0	-20	-18	60	7	8	5
70	5	62					
70	7	82		150			
70	8		80	172			
70	9	97					
70	10		92				
233	9						93
260	6	38					
277	11						55
280	7	18					
321	9			72			
360	10		-5				23
440	8				2		
471	10	3					
474	9					15	

[redacted]

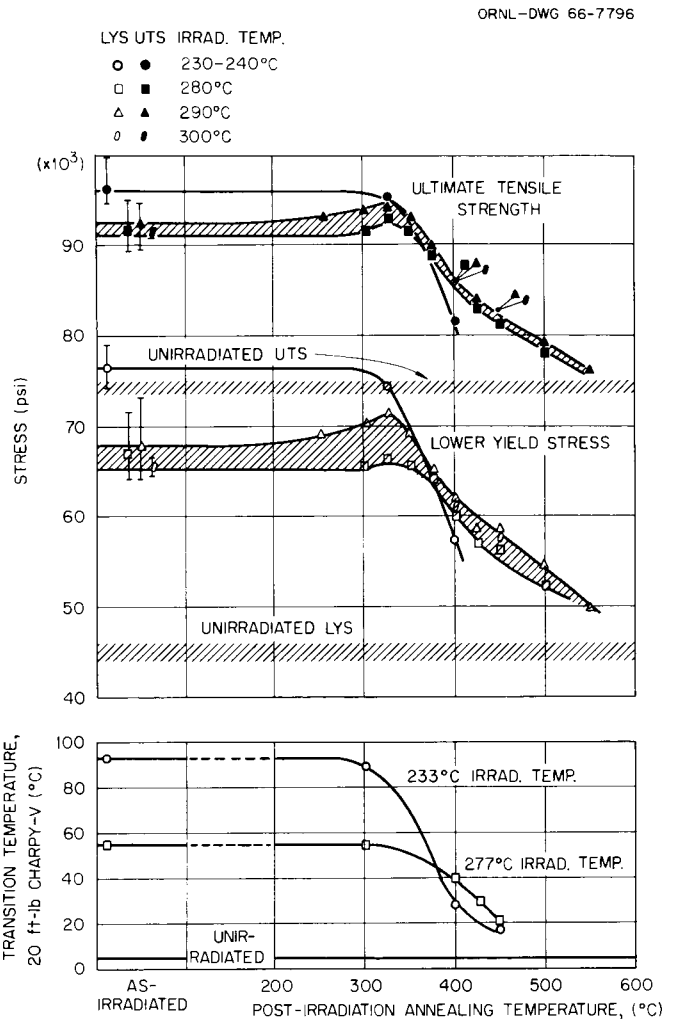

Fig. 1. Effect of Post-Irradiation Annealing on the Ultimate Tensile Strength, Lower Yield Stress and Charpy-V Notch Transition Temperature of ASTM A-212B Steel (SSD Item No. 157) Irradiated to 4 - 11 x 10^{18} neutrons/cm^2 (E > 1 Mev).

since, as shown in Figure 1, there is a general trend towards higher temperatures for recovery of tensile properties and transition temperature for specimens irradiated at higher temperatures.

Neutron Dosimetry

Neutron dosimeters used in these experiments include cobalt, cadmium-shielded cobalt, nickel, cadmium-shielded nickel, and iron. Because of the low melting point of cadmium, we were unable to use cadmium-shielded

[redacted]

Table 4. Tensile Properties of Irradiated ASTM A-212 Grade B, Carbon-Silicon Steel and Effect of Post-Irradiation Annealing. (SSD Item 157)

Fast Neutron Dose (E > 1 Mev)	Irradiation Temperature (°C)	Post-Irradiation Anneal Temp. (°C)	Post-Irradiation Anneal Time (min)	Lower Yield Stress (ksi)	Ultimate Strength (ksi)	Fracture[a] Strength (ksi)	Uniform[b] Elongation (%)	Total[c] Elongation (%)
($\times 10^{18}$ n/cm^2)								
0	R.T.	--	--	44.9	73.8	60.2	18	25
0	R.T.	--	--	44.8	73.6	59.0	22	25
0	R.T.	250	100	45.6	74.2	59.6	20	23
0	R.T.	250	1420	44.8	73.8	60.0	20	24
0	R.T.	325	100	43.8	74.5	58.4	21	27
0	R.T.	325	1420	45.1	74.7	58.5	21	28
0	R.T.	375	100	45.2	74.4	60.0	19	22
0	R.T.	425	25	45.9	74.4	58.4	21	24
0	R.T.	425	100	45.9	74.8	61.0	21	26
0	R.T.	425	1420	45.6	73.0	59.2	20	27
0	R.T.	500	100	45.9	73.4	57.8	20	24
0	R.T.	550	125	45.9	73.3	57.3	21	29
4	290	--	--	64.1	89.5	73.0	14	20
4	290	--	--	67.4	93.1	75.9	14	18
4	290	300	1420	64.4	89.8	72.1	14	18
4	290	550	100	50.1	76.4	61.9	19	23
4	290	550	1420	47.2	93.9	77.7	21	28
5	280	--	--	71.5	95.0	77.2	13	17
5	280	375	1420	61.2	85.5	69.5	17	21
5	280	450	100	57.8	82.2	66.4	17	24
5	280	500	100	51.9	77.9	62.7	17	22

Table 4 (Continued)

5	290	--	--	65.6	90.7	71.3	15	20
5	290	--	--	66.5	92.1	75.6	12	17
5	290	--	--	68.2	92.5	75.0	16	18
5	290	--	--	73.2	94.7	78.9	9	14
5	290	250	1420	69.8	93.2	75.2	14	18
5	290	325	25	66.0	92.2	73.7	15	20
5	290	350	25	65.6	90.4	73.8	15	19
5	290	350	1420	63.6	88.4	71.8	16	20
5	290	375	25	64.6	89.6	73.0	14	18
5	290	425	25	61.4	86.2	69.0	17	22
5	290	425	100	58.7	84.2	67.7	17	21
5	290	425	1420	56.6	81.8	66.6	17	25
5	290	450	25	56.3	81.4	66.6	16	20
5	290	450	1420	55.4	80.7	63.5	19	24
5	290	500	25	55.7	81.8	64.5	20	26
5	290	500	100	54.4	79.3	63.6	19	25
5	290	500	1420	51.8	77.8	61.9	19	27
5	290	550	25	52.1	77.7	62.4	18	28
6	230	325	1420	69.7	91.6	73.4	15	20
6	240	--	--	74.1	94.6	75.9	12	18
6	240	--	--	76.4	95.8	78.0	13	17
6	240	400	100	56.7	81.8	66.3	15	21
6	240	400	100	59.9	81.2	63.9	18	26
6	280	400	25	62.7	86.8	68.2	16	23
6	280	425	100	57.1	83.0	67.2	14	21
6	290	--	--	66.2	91.6	74.0	15	20
6	290	--	--	69.2	93.9	76.7	15	18
6	290	--	--	69.6	94.1	75.4	15	19
6	290	250	100	69.2	93.3	75.2	13	16
6	290	300	100	70.4	93.9	75.5	14	18

Table 4 (Continued)

6	290	325	100	71.6	95.3	77.2	14	18
6	290	350	100	69.3	93.3	76.8	14	17
6	290	375	100	64.8	89.7	73.5	15	19
6	290	400	100	61.8	86.0	71.3	13	19
6	290	400	1420	58.2	83.9	67.7	15	22
6	290	450	100	58.5	83.1	67.5	17	21
6	290	500	100	53.7	78.7	63.7	16	22
6	290	500	100	54.4	79.3	63.6	19	25
6	300	--	--	64.5	90.8	73.5	16	20
6	300	--	--	65.5	91.4	74.4	14	18
6	300	--	--	66.4	91.7	74.3	14	18
6	300	400	100	60.3	85.2	68.3	16	25
6	300	400	100	61.8	87.3	71.9	15	22
6	300	450	100	58.1	82.9	67.0	14	21
7	230	--	--	75.6	95.4	87.3	12	16
7	230	--	--	77.2	96.1	78.4	12	15
7	230	325	25	75.8	96.1	78.7	13	16
7	230	325	100	74.5	95.5	77.4	13	18
7	230	400	100	56.5	81.8	65.1	21	23
9	230	--	--	78.9	99.8	82.4	12	15
10	280	--	--	64.3	89.4	73.5	13	16
10	280	--	--	65.1	90.7	74.0	13	17
10	280	--	--	68.3	92.4	74.9	15	20
10	280	350	100	65.4	90.7	74.8	15	21
10	280	400	100	60.3	85.6	68.9	12	19
10	280	450	100	55.6	80.5	63.7	15	24
10	280	500	100	53.1	79.2	64.0	17	25
11	280	--	--	65.4	90.1	76.1	11	16
11	280	--	--	66.7	91.3	72.9	17	20

Table 4 (Continued)

11	280	--	--	67.5	91.3	73.7	14	17
11	280	--	--	67.6	92.1	75.5	13	19
11	280	300	100	64.5	90.6	72.7	12	18
11	280	300	100	66.7	93.1	75.4	14	21
11	280	325	100	66.7	93.0	75.6	15	19
11	280	350	100	66.1	92.7	75.5	14	22
11	280	375	100	74.2	89.0	71.7	16	20
11	280	400	100	60.1	85.3	68.4	15	21
11	280	450	100	55.9	81.4	64.8	15	22
11	280	500	100	53.4	79.0	62.8	20	23
11	290	--	--	68.3	92.4	74.7	13	18

[a]Fracture load/original area.

[b]Average elongation at maximum load.

[c]From load-elongation record.

monitors at the specimen position of the elevated temperature experiments. In elevated temperature experiments bare monitors were used at the specimen positions and both bare and cadmium shielded monitors were installed in the cool region of the experiments, 1 1/8 inches behind the specimens. Results from bare nickel monitors were corrected for thermal neutron burn-up of ^{58}Co based on ^{60}Co results. The corrected results from the bare nickel monitors were within 2 per cent of the results of the cadmium-shielded nickel monitors. The results from the iron monitors were not consistent and are not reported. Fast neutron monitor cross sections were based on a fission spectrum since insignificant errors are expected due to deviations from a fission spectrum at the experiment location. Conversion to doses of neutrons of energy greater than 1 Mev was also based on a fission spectrum. An effective threshold cross section of 420 millibarns and threshold energy of 2.9 Mev was used for the $^{58}Ni\ (n, \gamma)\ ^{58}Co$ reaction.

Stress-Grain Size Analysis of the Ductile-Brittle Transition for Steel and Similar Metals*

R. W. Armstrong

It was shown in an earlier study[4] that, for mild steel and similar metals, an explicit equation for the ductile-brittle transition temperature, T_c, may be obtained directly from the various components of the (Hall-Petch) stress-grain size relationships experimentally observed for ductile yielding and brittle fracture. Thus, the following equation results for the tensile ductile-brittle transition:

$$T_c = \frac{1}{\beta'} \left[\ell n B' - \ell n \left\{ (k_c - k_y) + (\sigma_{oc} - \sigma^*_{oy}) \ell^{1/2} \right\} - \ell n \ell^{-1/2} \right], \quad (1)$$

---

*This study was supported at Brown University by the Advanced Research Projects Agency and at the Solid State Division of the Oak Ridge National Laboratory through a Research Participant Appointment by the Oak Ridge Associated Universities.

[4] R. W. Armstrong, "On Determining the Ductile-Brittle Transition Temperature," Phil. Mag. 9, 1063 (1964).

where the foregoing parameters are contained in the equations for the brittle fracture stress, σ_c, and the yield stress, σ_y:

$$\sigma_c = \sigma_{oc} + k_c \ell^{-1/2} \tag{2}$$

$$\sigma_y = \sigma_{oy}^* + B' \exp(-\beta' T) + k_y \ell^{-1/2} . \tag{3}$$

In these equations, β' is the exponential temperature coefficient of the temperature-sensitive part of the yield stress, B' is the stress intercept of this yield component at 0°K, k_c is the effective internal stress concentration associated with brittle fracture (the slope of the brittle fracture stress plotted versus inverse square root of grain size), k_y is the stress concentration required at the tip of a slip band for initiating further plastic flow, σ_{oc} is the stress intercept for brittle fracture at hypothetical infinite grain size, σ_{oy}^* is the temperature-independent contribution to the yield stress intercept, and ℓ is the average grain diameter.

The analysis leading to the expression for T_c has a similar basis to that proposed by Cottrell[5] and Petch[6] for the same phenomenon in their coupled theoretical analyses. Some differences do exist. The stress-grain size analysis gives a form of T_c which is completely determined without recourse to introducing the quantity specified by Cottrell and Petch as the effective surface energy of a cleavage crack. In fact, the ductile-brittle transition is proposed to occur in the stress-grain size analysis when $\sigma_y = \sigma_c$. Thus, in this analysis, the main theoretical considerations underlying the ductile-brittle transition are only those which provide a basis for understanding the terms comprising the stress-grain size equations. As an example, Stroh[7] has calculated the value of k_c from

---

[5] A. H. Cottrell, "Theory of Brittle Fracture in Steel and Similar Metals," Trans. Met. Soc. AIME 212, 192 (1958).

[6] N. J. Petch, "The Ductile-Brittle Transition in the Fracture of α-Iron: I," Phil. Mag. 3, 1089 (1958).

[7] A. N. Stroh, "A Theory of the Fracture of Metals," Advances in Phys. 6, 418 (1957).

dislocation theory and the result for several metals, particularly, iron, is in good agreement with experiment. These features have been further elaborated in the present investigation.

Figure 2 illustrates the physical reasoning which supports this application of the stress-grain size analysis to the ductile-brittle transition phenomenon. The tensile yield, compressive yield, and brittle fracture stresses have been calculated for several mild steel specimens (0.15 C) using the experimental parameters estimated from the literature as given in Table 5. The influence of grain size on T_c may be determined by comparing steels A and B in Figure 2 and Table 5. Because of the inequality, $k_c > k_y$, the transition temperature is lower for the small grain size steel. A comparison of steels A and A* shows the influence on T_c of increasing σ^*_{oy}, say, by the thermal quenching of defects in solution or by introducing defects through neutron irradiation. Irradiation by approximately 10^{20} neutrons/cm^2 could produce the change noted in σ^*_{oy}.[8] The increase in T_c for A* results in this case because the brittle fracture parameters, σ_{oc} and k_c, are unchanged by these effects.

---

[8] D. Hull and I. L. Mogford, "Ductile-Brittle Transition in Steels Irradiated with Neutrons," Phil. Mag. 3, 1213 (1958).

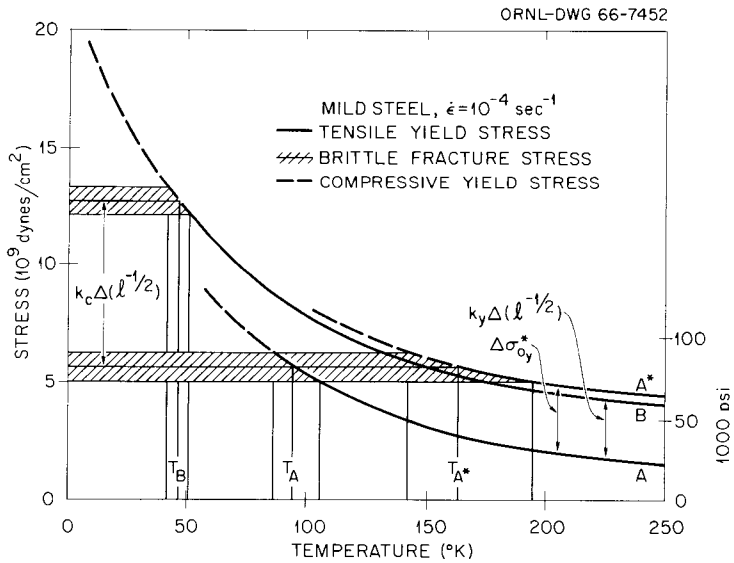

Fig. 2. Plastic Yielding and Fracture Strength of Mild Steel as a Function of Temperature.

Table 5. Hall-Petch Stress-Grain Size Constants for Mild Steel

Steel	σ_K^{-1} β'	10^8 dynes/cm^2 B'	10^7 dynes/cm$^{3/2}$		10^8 dynes/cm^2		cm$^{-1/2}$ $\ell^{-1/2}$
			k_c	k_y	σ_{oc}	σ^*_{oy}	
A	.0143	178	21 ± 1	7.3 ± 0.1	33 ± 5	3	10
B	.0143	178	21 ± 1	7.3 ± 0.1	33 ± 5	3	44.6
A*	.0143	178	21 ± 1	7.3 ± 0.1	33 ± 5	29	10

For tensile tests and Charpy notch impact tests, numerical computations have been done to show the dependence of T_c on grain size, strain rate and σ^*_{oy}. The following points are emphasized by the calculations: (1) the transition temperature measured in a notch impact test is more sensitive to grain size than that determined in a tensile test; (2) the transition temperature increases at an increasing rate with increase in σ^*_{oy}; and (3) the increase in transition temperature produced by adding to σ^*_{oy} is larger the larger the grain size of the material.

Radiation Hardening in Iron

S. M. Ohr, N. E. Hinkle, and M. S. Wechsler

In order to better understand the effect of neutron irradiation on the deformation characteristics of iron, a series of tensile tests were carried out concurrently with electron microscope observations of microstructures on neutron irradiated sheet samples of Ferrovac-E iron and zone-refined high purity iron. Small tensile samples of 1/2-inch-gage-length were prepared from cold rolled sheets of 0.01-inch-thickness. These samples were given suitable annealing treatments in vacuo to achieve a uniform grain diameter of approximately 30μ. Three experimental assemblies each containing 28 tensile samples were shielded with cadmium and were irradiated at temperatures between 55 and 90°C in the poolside facility of the ORR at a dose rate of approximately 3 x 10^{12} neutrons/cm^2

sec (E > 1 Mev). From various irradiation times a range of doses from 1.2×10^{16} neutrons/cm^2 to 2.5×10^{18} neutrons/cm^2 were obtained.

A. Tensile Tests

Figures 3 and 4 show the true stress true strain curves for neutron irradiated Ferrovac-E and zone-refined iron tested at room temperature. For the Ferrovac-E iron, a dose of only 1.2×10^{16} neutrons/cm^2 (E > 1 Mev) produced a noticeable increase in the yield and flow stresses. However, for the zone-refined iron only a slight increase in the yield stress was observed for this dose and the differences in the flow stresses as a function of strain were probably within experimental error. The following characteristics may be noticed from the stress-strain curves: 1) the yield stress has increased with increasing dose level, 2) the rate of work-hardening in the regions of uniform elongation has decreased, and 3) the samples have fractured in a ductile manner at this test temperature, i.e. through plastic instability and necking. The strain at which the instability occurs has decreased with increasing neutron dose. These observations are common to many other irradiated metals.

A close examination of the tensile curves reveals that the curves for the irradiated samples can be superimposed on the unirradiated curve by

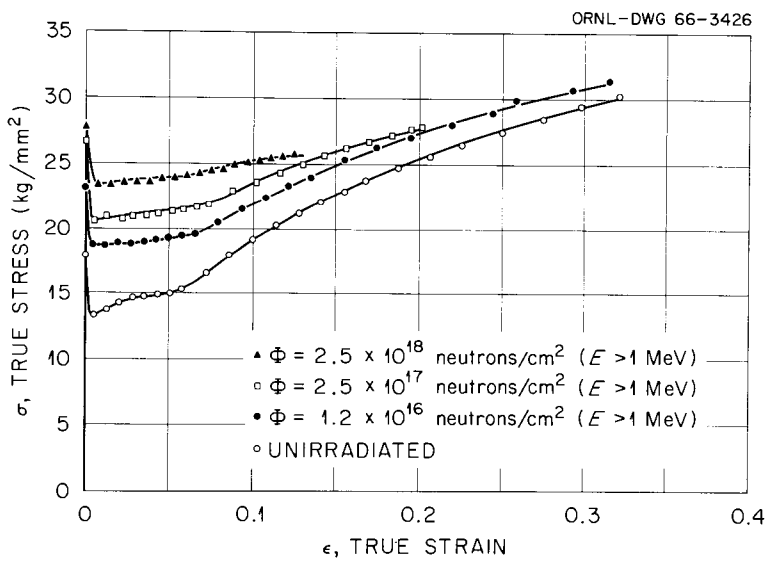

Fig. 3. True Stress-True Strain Curves of Neutron Irradiated Ferrovac-E Iron. The Grain Diameter is Approximately 30μ.

[redacted]

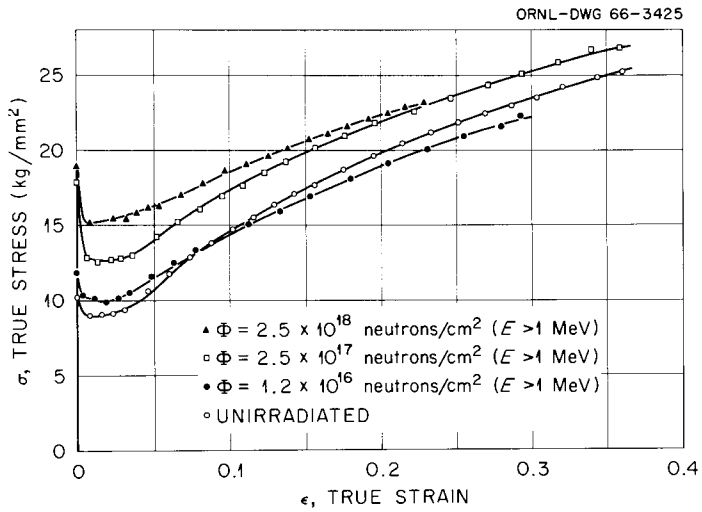

Fig. 4. True Stress-True Strain Curves of Neutron Irradiated Zone-Refined Iron (d = 30μ).

shifts to the right along the strain axis. The amount of shift necessary increases with the neutron dose. The implication of the superposition is that the neutron irradiation may be considered as being equivalent to "prestraining." To pursue the matter in a quantitative manner, we have fitted the stress-strain curves of Ferrovac-E iron past the Lüders strain in terms of a power function[9]

$$\bar{\sigma} = K(\bar{\epsilon}_o + \bar{\epsilon})^n \qquad (4)$$

where $\bar{\sigma}$ is the true stress, $\bar{\epsilon}$ is the actual true strain, $\bar{\epsilon}_o$ is an effective prestrain which gives an indication of the initial state of the matter, K is a measure of the basic strength of the material and is independent of its initial state, and n is the work-hardening exponent. For the unirradiated curve, the effective prestrain $\bar{\epsilon}_o$ is found to be zero and the values of K and n are given as 47.4 kg/mm^2 and 0.39, respectively. For the irradiated curves, the effective prestrain increases with increasing neutron doses. The values of effective prestrain are tabulated in Table 6. In

[9]W. Johnson and P. B. Mellor, p. 170 in Plasticity for Mechanical Engineers, D. Van Nostrand Co., London, 1962.

[redacted]

Table 6. The Dose Dependence of Effective Prestrain in Neutron Irradiated Ferrovac-E Iron

Dose (n/cm^2)	Effective Prestrain $\bar{\epsilon}_o$
0	0
1.2×10^{16}	0.039
2.5×10^{17}	0.067

Fig. 5 we have plotted the flow stress as a function of the total strain, i.e. the sum of the effective prestrain and the actual strain. The fit is surprisingly good and the values of K and n are not affected by irradiation. Although there are not sufficient data as yet to attach real significance, the effective prestrain $\bar{\epsilon}_o$ appears to be proportional to the neutron dose to the 1/6th power,

$$\bar{\epsilon}_o = C\Phi^{1/6} \tag{5}$$

and the line through the irradiated values extrapolates to the origin, i.e. to the unirradiated value. The representation of the dose dependence of radiation hardening in terms of the effective prestrain has an advantage over that of plotting yield stress in that the effective prestrain vanishes automatically in the unirradiated state. It eliminates, therefore, the problem of having to choose between the magnitude itself and its increment in representing the dose dependence.

The effective prestrain concept of radiation hardening has another point of support in that it predicts correctly the premature onset of plastic instability in the irradiated samples. The condition for the plastic instability may be written

$$\frac{\partial\sigma}{\partial\bar{\epsilon}} = 0 \tag{6}$$

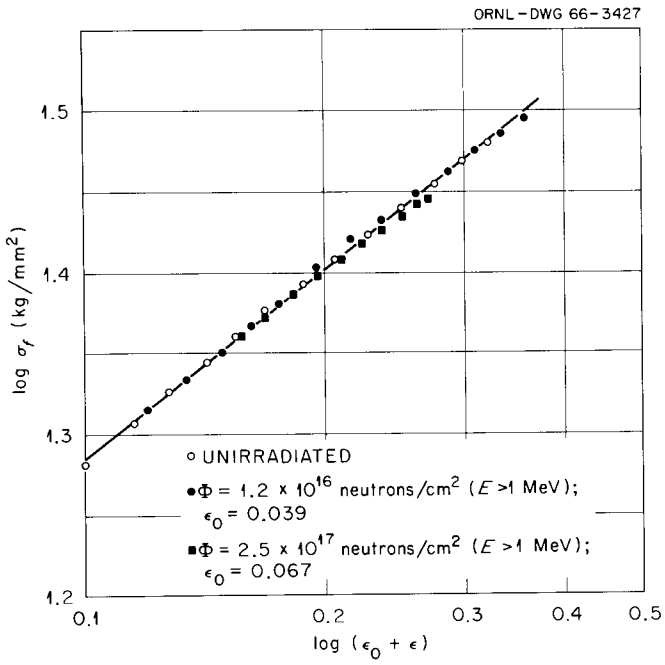

Fig. 5. Flow Stress vs Total Strain in Neutron Irradiated Ferrovac-E Iron.

where σ is the nominal stress and is related to $\bar{\sigma}$ by $\bar{\sigma} = \sigma e^{\bar{\epsilon}}$. Substituting this in Eq. 4 and applying Eq. 6, we find for the true strain at the plastic instability

$$\bar{\epsilon} = n - \bar{\epsilon}_o \quad .$$

Since n is independent of dose in the range studies (Fig. 5) and $\bar{\epsilon}_o$ increases with dose (Table 6), the strain at the plastic instability decreases with dose. This is in agreement with our experimental observation. We are in the process of extending the analyses on a quantitative basis.

B. Transmission Electron Microscopy

We have also made observations of microstructure of neutron irradiated and plastically deformed iron samples by thin film transmission electron microscopy in order to seek microstructural correlation with the tensile test results. The neutron irradiated sheet samples were plastically deformed to various amounts of strain at room temperature, electrolytically

thinned in a bath of perchloric-acetic acid, and examined in a Hitachi electron microscope operated at 100kv.

Figure 6 shows a typical microstructure observed in an early stage of deformation. In these samples, spot damage has not been seen except in the immediate vicinity of dislocation tangles. Spot damage, however, has been seen in iron samples irradiated to a dose greater than 10^{20} neutrons/cm^2.[10,11] A noticeable change in the microstructure is that

---

[10] B. L. Eyre and A. F. Bartlett, "An Electron Microscope Study of Neutron Irradiated Damage in Alpha-Iron," Phil. Mag. 12, 261 (1965).

[11] J. S. Bryner, "A Study of Neutron Irradiation Damage in Iron by Electron-Transmission Microscopy," Acta Met. 14, 323 (1966).

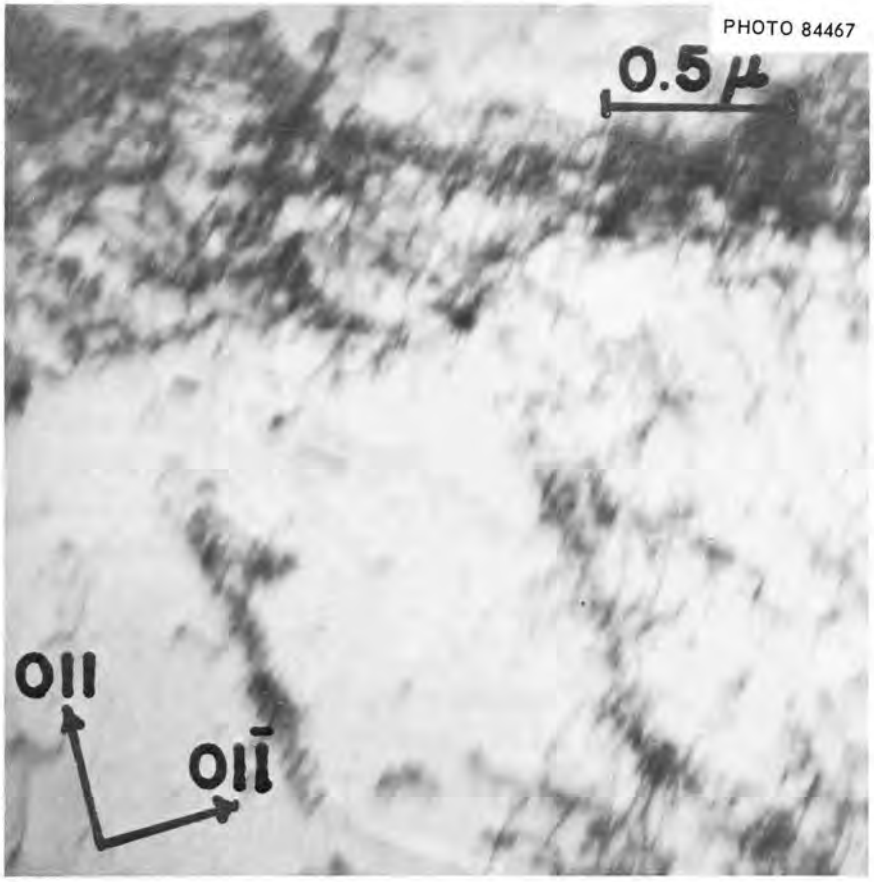

Fig. 6. Electron Micrograph Showing Deformation Structure of Neutron Irradiated Ferrovac-E Iron. Dislocations have Severely Tangled and the Cell Structure has Already Developed.

although the sample was extended only slightly, the dislocations have tangled to such an extent that the formation of a cell structure is evident. The structure corresponds to that of somewhat more heavily deformed unirradiated samples. A crystallographic analysis based on the selected area diffraction indicates that the cell walls lie along the traces of (110) or (112) slip planes.

Figure 7 shows a dark band frequently observed in the irradiated and deformed samples. The band structure has not been observed in the unirradiated samples. The dislocation content in the bands varies widely from band to band. The contrast at the band can be reversed with respect to the surrounding areas by tilting the sample, as shown in Fig. 8. From the

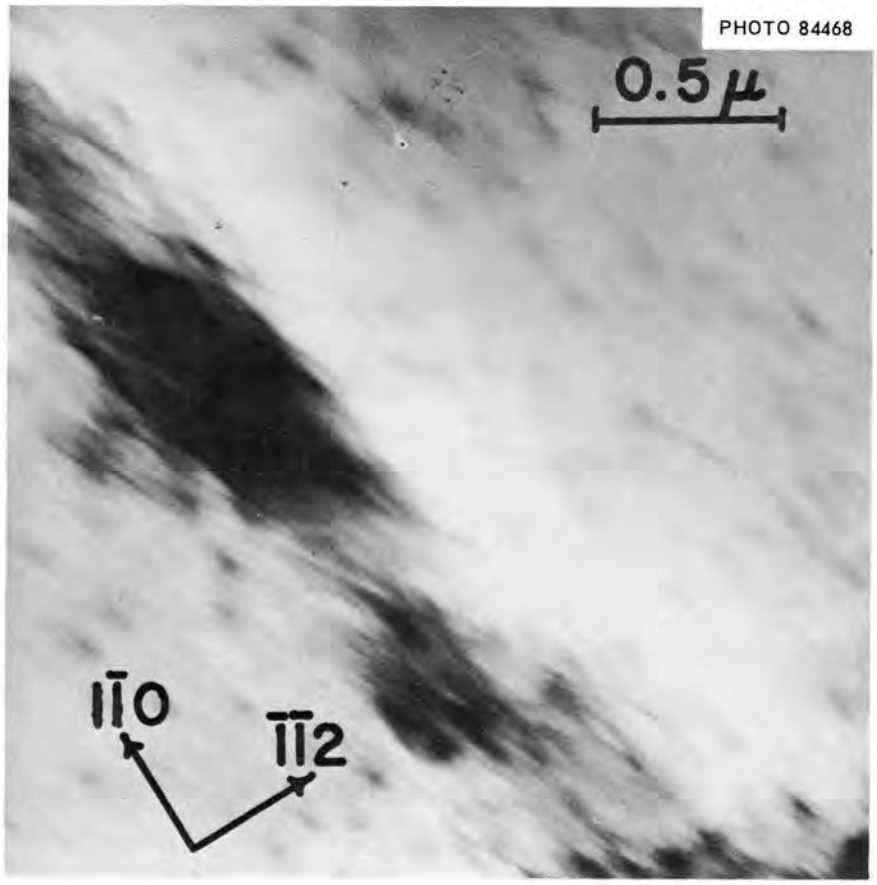

Fig. 7. A Dark Band in Neutron Irradiated and Deformed Iron. The Band Lies Along the Trace of a (112) Slip Plane. The Band is Believed to be the Dislocation Channel.

[redacted]

Fig. 8. The Same Area as Fig. 5 after Tilting a Fraction of a Degree. The Contrast at the Band is Reversed. The Contrast is Identified as a Thickness Interference Fringe.

electron diffraction patterns, the possibility of the band being a twin has been ruled out. When a thickness extinction contour is made to cross the band, the contour is found to stretch along the band indicating that the thickness of the foil is reduced somewhat in the region of the band. Since the bands are found to lie along the projected traces of the slip planes, it is concluded that the bands represent dislocation channels.[10,12] The contrast is believed to originate from the difference in foil thickness, caused by preferential thinning during polishing, that is equal to half of the extinction distance for the operating Bragg reflection.

---

[12] B. Mastell, H. E. Kissinger, J. J. Laidler, and P. K. Bierlein, "Dislocation Channeling in Neutron-Irradiated Molybdenum," J. Appl. Phys. 34, 3637 (1963).

[redacted]

C. Discussion

The results of tensile tests and the observations of microstructure by transmission electron microscopy will now be discussed briefly. The presence of dislocation channels implies that the motion of dislocations is restricted into a limited number of bands in the neutron irradiated crystals. The local plastic strain in these bands, therefore, may be substantially greater than the average strain over the sample. If the dislocations continue to move in these bands, it will create in the bands a number of areas that are rich in dislocation content and are free of radiation induced defects. It is, therefore, reasonable to expect the deformation characteristics and microstructures of an irradiated crystal to be similar to that of a prestrained unirradiated crystal. Other evidence in support of this idea is that the internal stress in the irradiated crystal, measured by a stress relaxation technique,[13] is consistently higher than the corresponding value in the unirradiated crystal. The internal stress is also found to increase with plastic strain.

The build-up of stress concentration by dislocations confined to narrow bands is one of several possible causes for the observed increase in internal stress in irradiated crystals. An elastic interaction between the moving dislocations and the stress field of the irradiation induced defects themselves can also contribute to the increase in the internal stress.[14] A model based on such an interaction, predicts an increase in stress to move a dislocation that is proportional to the maximum repulsive force exerted by the defects. An alternative approach, due to Orowan,[15] is to consider the stress necessary to bow out dislocations between two adjacent defects that are assumed to remain rigid. The increase in stress

---

[13] S. M. Ohr, N. E. Hinkle, J. M. Williams, and M. S. Wechsler, "Dislocation Dynamics in Irradiated Iron," to be in Radiation Effects in Materials, Gordon and Breach, New York, 1966.

[14] R. L. Fleischer, "Solution Hardening by Tetragonal Distortions: Application to Irradiation Hardening in F.C.C. Crystals," Acta Met. 10, 835 (1962).

[15] E. Orowan, p. 451 in Symposium on Internal Stress, Inst. Metals, London, 1948.

in this model is expected to be proportional to the line tension of a dislocation. Both of these models predict the magnitude of hardening to increase inversely to the mean spacing between the defects.

The evidence of dislocation channeling, i.e. the obliteration of defects by moving dislocations, suggests that a certain modification is necessary to these strengthening mechanisms. When the defects are absorbed by moving dislocations, a number of jogs are expected to form on the dislocations. To some of the jogs, climb may be the only possible means of motion as they are forced to follow the rest of the dislocation segment. The additional force needed to move the jogged dislocation may contribute substantially to the increase in the yield stress.[16] The observation of dislocation channels in the irradiated iron in the absence of visible spot damage suggests that the dislocation channeling is a consequence of the interaction between moving dislocations and submicroscopic point defect clusters introduced by irradiation.

Effect of the Number of Zone Passes on the Flow Stress of Niobium Single Crystals*

R. E. Reed

Recent reports[17,18] on work in progress on the purification of niobium metal have shown the effect of number of electron beam floating zone passes upon the purity of niobium. This report will describe the effect of zoning upon the tensile properties of niobium single crystals.

---

[16] N. F. Mott, "The Work Hardening of Metals," Trans. AIME 218, 962 (1960).

[17] R. E. Reed and M. S. Wechsler, "Plastic Deformation in Niobium Single Crystals," Radiation Metallurgy Section Solid State Division Progress Report for Period Ending August 1965, ORNL-3878, Jan. 1966. pp. 36-48.

[18] R. E. Reed, "The Preparation and Purification of Single Crystals of Niobium," Radiation Metallurgy Section Solid State Division Progress Report for Period Ending February 1966, ORNL-3949, May 1966, pp. 35-50.

*Work sponsored by the Research Materials Program of the A.E.C.

Experimental Procedure

The niobium used in this study came from two sources. An electron beam melted niobium ingot was obtained from Wah Chang Corp. and some niobium granules were received from DuPont Corp. The purity of the starting material and the effect of electron beam floating zone refining upon the purity have been described elsewhere.[19]

For the tensile tests, single crystals of niobium were grown at 10 cm/hr in the zone refiner at 1×10^{-6} torr vacuum. The samples were seeded so as to produce all samples in a single orientation near the center of the stereographic triangle where the Schmid factor, $\cos \lambda_o \cos \phi_o$ (λ_o and ϕ_o are the initial angles between the tensile axis and the slip direction and slip plane normal, respectively), has its maximum value of one-half.

The seeded zone refined niobium single crystal rods, 4.8mm-diameter, that were used for tensile specimens were not chemically analyzed. It was assumed that these rods would be similar in purity to those prepared in a duplicate procedure and analyzed. The present rods were cut into 3.8cm-long sections using an abrasive wheel. The sections were then centerless ground to produce a gage section 1.9-cm-long and 2.160mm in diameter with a taper of less than 0.005mm. After grinding, about 500 microns were removed from the diameter by chemical polishing in a $HF-HNO_3$ solution. This was sufficient to eliminate all signs of cold work in the Laue back-reflection patterns.

The perfection of some seeded one-pass rods of Wah Chang niobium was studied using etch pitting, Berg-Barrett x-ray topographs, Borrmann anomalous x-ray topographs, and double crystal x-ray spectrometry. The dislocation density of the as-zoned rods as indicated by etch pit counts ranged from 10^4 - 10^6 cm $^{-2}$. The majority of the dislocations were in sub-boundaries. The misorientation of these sub-boundary walls were generally less than 180 seconds. The largest sub-boundary misorientation found was 8-10 minutes. This work was reported in more detail in another paper.[20]

---

[19] R. E. Reed, "Electron Beam Floating Zone Refining of Niobium," Proceedings of the Second Internat'l Conf. on Electron and Ion Beam Science and Technology, April 17-20, 1966, New York, Gordon and Breach, to be published.

[20] R. E. Reed, T. O. Baldwin, and H. D. Guberman, "The Growth of Niobium Single Crystals with Good Crystalline Perfection," Proceedings of the Internat'l Conf. on Crystal Growth, Boston, June 20-24, 1966, Supplementary Vol. Internat'l J. Phys. Chem. Sol., Feb. 1967.

The tensile specimens were pulled in tension at room temperature at a strain rate of 1.8×10^{-4} sec^{-1}. A table model Instron tensile testing machine was used.

Results and Discussion

Figures 9 and 10 show the tensile curves for Wah Chang and DuPont niobium respectively up to 1.0 shear strain for 1, 4, and 12 pass material. Figure 11 shows resolved shear stress at the lower yield point as a function of number of passes for both starting materials. This shear stress decreases with increasing number of passes for both starting materials. The drop in the shear stress per pass decreases as the number of zoning passes increases. The DuPont niobium had the lowest shear stress of 1.19 kg/mm^2 after 12 passes.

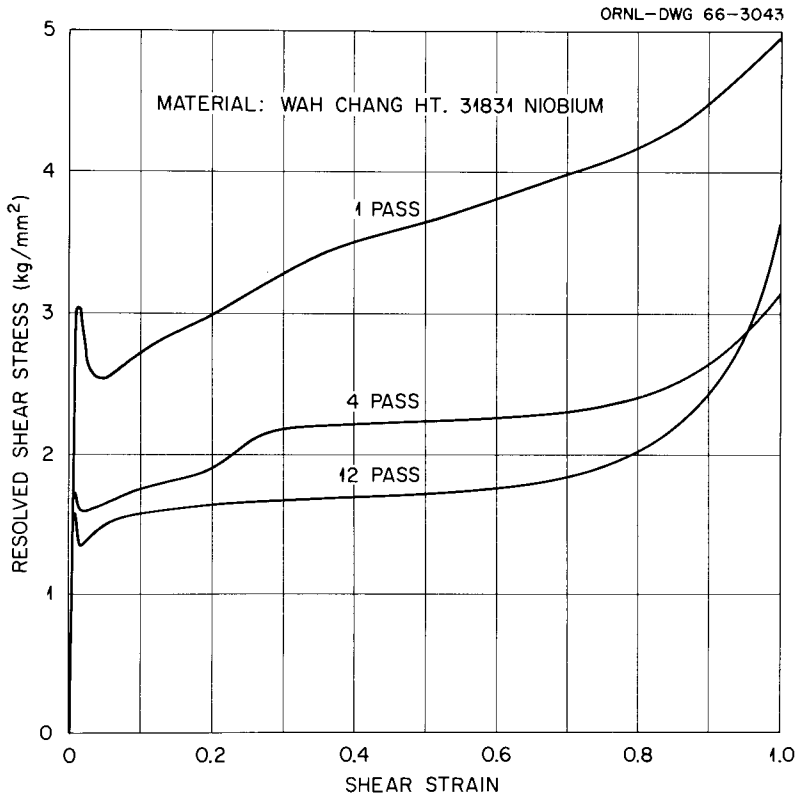

Fig. 9. Resolved Shear Stress-Shear Strain Curves for the Tensile Deformation of Niobium Single Crystals as a Function of the Number of Floating Zone Passes. Source: Wah Chang Corp.; zone speed: 10 cm/hr.

[redacted]

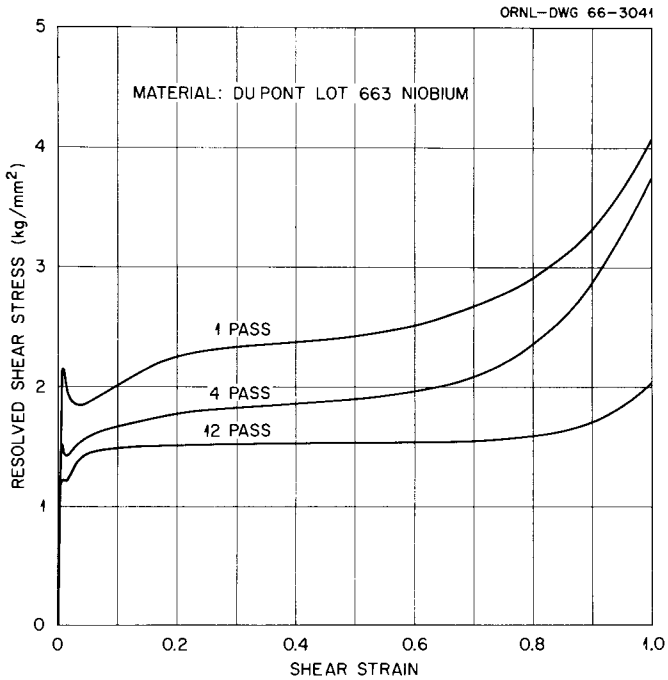

Fig. 10. Resolved Shear Stress-Shear Strain Curves for the Tensile Deformation of Niobium Single Crystals as a Function of the Number of Floating Zone Passes. Source: DuPont Corp.; zone speed: 10 cm/hr.

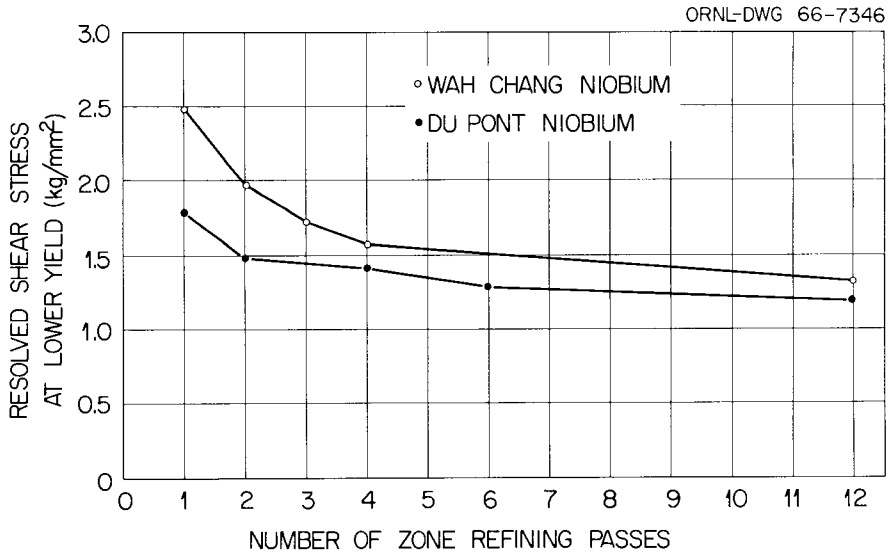

Fig. 11. Resolved Shear Stress at the Lower Yield Point as a Function of the Number of Floating Zone Passes for Niobium from Two Sources.

[redacted]

A resolved lower yield shear stress of 2.6 kg/mm^2 was reported by Votava[21] for 3 pass (at 84 cm/hr) Murex niobium with a tensile axis orientation and tensile strain rate similar to the present investigation. A Vickers hardness number of 44-48 was also indicated. His gas analysis for this material was 0.2-1.5 ppm H_2, 12-17 ppm N_2, and 10-26 ppm O_2. No other analyses were given. This material compares with one pass Wah Chang niobium zone refined at 10 cm/hr. Here, the Vickers hardness number was 42-49, the shear stress was 2.5 kg/mm^2, and the gas analysis was 24 ppm N_2, 30 ppm O_2, and 4 ppm H_2.

The Murex niobium generally has a rather high carbon content (~ 100 ppm)[22,23] and high Ta content (1200-3000 ppm)[23,24] compared to the material sources used in this study. This could explain the difference between the flow stresses reported by Mitchell, Foxall, and Hirsch[24] and those given in Fig. 11. They reported values for the resolved shear stress at the lower yield point ranging from 3.5 to 1.8 kg/mm^2 for 1 to 6 pass Murex niobium. This was obtained on material zoned in $< 5 \times 10^{-6}$ torr vacuum at 30 cm/hr for all passes except the last one which was at 12 cm/hr. The tensile axis orientation was similar to that used in this study but the strain rate was lower (4.5×10^{-5} sec^{-1}). In addition, Mitchell, Foxall, and Hirsch[24] reported that after 6 passes the niobium picked up extensive Ta and W contamination from the electron gun while the O_2, N_2, and H_2 content decreased only slightly. No carbon analyses were reported.

---

[21] E. Votava, "A New Method for the Preparation of Strain-Free Single Crystal Tensile Specimens for High Melting Point Metals and Some Results on the Plastic Deformation of Niobium Single Crystals," Phys. Stat. Sol. 5, 421-434 (1964).

[22] E. Votava, "Effect of Purity on the Mechanical Properties of Niobium," J. Less-Common Metals 9, 409-415 (1965).

[23] M. J. Leadbetter and B. B. Argent, "The Effect of Oxygen on the Mechanical Properties of Zone-Refined Niobium," J. Less-Common Metals 3, 19-28 (1961).

[24] T. E. Mitchell, R. A. Foxall, and R. B. Hirsch, "Work-Hardening in Niobium Single Crystals," Phil. Mag. 8, 1895-1920 (1963).

Taylor and Christian[25] further purified their material by resistance heating a 3 mm-diameter zone refined niobium rod to ~ 2400°C in ~ 1×10^{-8} torr vacuum. This treatment improved the resistance ratio, R(300°K)/R (20°K), of the as-zoned rod from ~ 100:1 to ~ 2000:1. Their value of resolved shear stress for yielding in compression at a strain rate of 6×10^{-4} sec^{-1} was 0.85 kg/mm^2.

Wronski and Fourdeux[26] used a "flash annealing" technique which probably accomplished the same result on polycrystalline niobium sheet. They obtained a resistance ratio, R(295°K)/R(77°K), equal to 5.68 and a resolved shear stress for yielding of ~ 2 kg/mm^2. Their vacuum was 1×10^{-6} torr. The specimen was heated to temperatures near the melting point for a few seconds at a time.

Annealing techniques will be utilized in future work at ORNL in an attempt to achieve further purification and increased perfection in niobium single crystals.

The tensile curves in Figs. 9 and 10 agree in their general features with those published by Mitchell, Foxall, and Hirsch.[24] There is a yield point followed by a region with an initially high hardening rate (stage 0) decreasing to the low rate characteristic of stage I. At about 30 to 40% tensile strain (approximately 0.6 to 0.8 shear strain) a transition region begins which is followed by a stage II hardening rate considerably higher than stage I. Stage III is characterized by a decreasing work hardening rate leading to fracture. All fractures were "chisel point" type with almost 100% reduction in area.

The yield points shown in Figs. 9 and 10 are extremely interesting when compared to the interstitial impurity analyses. A wide yield point and large yield drop with an extensive stage 0 (from a shear strain of 0.05 to 0.35 in Fig. 9 was characteristic of the Wah Chang one-pass niobium single crystals. The 12-pass Wah Chang niobium single crystal tensile curve exhibited a much sharper yield point and a smaller yield drop with

---

[25] G. Taylor and J. W. Christian, "The Effect of High Vacuum Purification on the Mechanical Properties of Niobium Single Crystals," Acta Met. 13, 1216-1218 (1965).

[26] A. Wronski and A. Fourdeux, "The Deformation of Polycrystalline Niobium at Room Temperature," J. Less-Common Metals 7, 205-211 (1964).

shorter stage 0 (Fig. 9). The chemical analyses were 11 ppm C, 30 ppm O_2, 24 ppm N_2 for the one-pass niobium and 45 ppm C, 24 ppm O_2, 5 ppm N_2 for the 12-pass material. This suggests that a sharp yield point and short stage 0 may be associated with the carbon impurity while the wide yield point and extensive stage 0 are due to oxygen and/or nitrogen.

The results on the DuPont single crystal niobium (Fig. 10) support this suggestion. In this case, the one-pass DuPont niobium single crystal exhibited a much sharper yield point, smaller yield drop and a less extensive stage 0 than the one-pass Wah Chang niobium. The 12-pass material had essentially no yield point and a very short stage 0. In this material there was ~ 26 ppm C, ~ 10 ppm O_2, < 5 ppm N_2 after one pass and ~ 23 ppm C, < 5 ppm O_2, < 5 ppm N_2 after four passes. The twelve-pass material has not been analyzed yet. Again, the sharp yield point and short stage 0 could be associated with the carbon interstitial impurity. Further work will be done on this point.

Conclusions

The resolved lower yield stress for niobium decreased with increasing number of electron beam floating zone passes. The lowest yield stress obtained was 1.2 kg/mm^2 for DuPont niobium zone refined with 12 passes at 10 cm/hr. The tensile stress-strain curves exhibited four stages of hardening similar to those described by Mitchell, Foxall, and Hirsch.[24] There was some indication that the carbon impurity may be associated with a sharp yield point and short stage 0 while oxygen and/or nitrogen may be associated with a wide yield point and extensive stage 0.

Dependence of Yield Stress on Neutron Dose in Niobium Single Crystals

R. P. Tucker, M. S. Wechsler, and N. E. Hinkle

It is well known that neutron bombardment induces significant changes in the physical and mechanical properties of metals. Considerable interest exists in the hardening, i.e. the increase in the critical shear stress for plastic deformation, produced by irradiation. Seeger[27] has proposed a

[27] A. K. Seeger, "On the Theory of Radiation Damage and Radiation Hardening," Proc. Second Internat'l Conf. Peaceful Uses of Atomic Energy, Vol. 6, 1958, p. 250.

theory in which radiation hardening is thought to be attributable principally to the vacancy-rich zones at the displacement spikes, which act as barriers to dislocation motion. This lattice hardening theory, in the absence of saturation effects, predicts that the critical shear stress varies as the square root of the neutron dose. Several investigations of the dependence of the yield stress on dose have been carried out on face-centered cubic metals. The first extensive study of the dependence of hardening on radiation dose was done on copper single crystals by Blewitt et al.[28] They found that the upper yield stress varies as the cube root of the dose over the range from 10^{16} to 10^{20} neutrons/cm^2. The cube root dependence is inconsistent with the Seeger theory of friction hardening due to interaction of dislocations with zones penetrating the slip plane. Blewitt et al. suggested hardening is due to the interaction of irradiation induced defects with dislocation sources. Diehl[29] also did dose dependence studies on copper as well as nickel single crystals, finding for copper better agreement to the square root than the cube root dependence for the lower yield stress in the low dose range and evoking a saturation effect to explain the results at higher doses.

Little work is reported in the literature on the dose dependence of the yield stress in body-centered cubic metals. Wronski et al.[30] have reported that polycrystalline molybdenum follows the square root dependence when the change in lower yield stress on irradiation is plotted as a function of neutron dose. They do not interpret the agreement with Seeger's theory to necessarily favor the friction hardening mechanism. Hinkle

---

[28] T. H. Blewitt, R. R. Coltman, R. E. Jamison, and J. K. Redman, Radiation Hardening of Copper Single Crystals," J. Nucl. Materials 2, 277 (1960).

[29] J. Diehl, "The Influence of Neutron Irradiation on the Mechanical Properties of Face-Centered Cubic Metal Crystals," p. 129 in Radiation Damage in Solids, Vol. 1, IAEA, Vienna, 1962.

[30] A. S. Wronski, G. A. Sargent, and A. A. Johnson, "Irradiation Hardening and Embrittlement in Body-Centered Cubic Transition Metals," Flow and Fracture of Metals and Alloys in Nuclear Environments, STP-380, American Society for Testing and Materials, Philadelphia, p. 69, 1965.

et al.[31] have reported for polycrystalline Ferrovac-E iron of two grain sizes slopes of 0.1 and 0.15 for a plot of lower yield stress versus dose and slopes of 0.22 and 0.35 when the increase in the lower yield stress rather than the stress itself is plotted.

A program to investigate the dependence of yield stress on neutron dose in niobium single crystals has been initiated and the initial results for doses over the range from 10^{15} to 10^{18} neutrons/cm^2 are reported.

Materials and Experimental Procedure

Niobium single crystals from Wah Chang Corporation starting stock were prepared by a single pass of an electron-beam-induced vertical, floating zone. The chemical analyses of the starting stock and single pass zoned material have been given previously.[32,33] The major metallic impurities remaining in the zoned niobium after one pass are tantalum and tungsten. Table 7 lists the metallic impurities as determined by spark source mass spectrometry which equal or exceed one weight part per million.

Tensile samples were prepared by centerless grinding 0.75 in. gage lengths on 1.5 in. long sections of the zoned rods. The 0.085 in. as-ground gage diameter was chemically polished to a nominal diameter of 0.065 in. using a solution of nitric acid (70 per cent) and hydrofluoric acid (48 per cent) mixed in proportions of 3 to 2. Polishing down 20 mils was found to be more than sufficient to remove all evidence of cold work detectable by the Laue back-reflection method. The final sample diameters were measured using a toolmaker's microscope.

The sample was oriented such that a uniaxial tensile load initially gave rise to a maximum resolved shear stress on the $(\bar{1}01)[111]$ slip system,

---

[31] N. E. Hinkle, N. K. Smith, and M. S. Wechsler, "Tensile Tests on Irradiated Iron," Radiation Metallurgy Section Solid State Division Progress Report for Period Ending February 1966, ORNL-3949, May 1966, p. 8.

[32] R. E. Reed and M. S. Wechsler, "Plastic Deformation in Niobium Single Crystals," Radiation Metallurgy Section Solid State Division Progress Report for Period Ending August 1965, ORNL-3878, August 1965, p. 36.

[33] R. E. Reed, "The Preparation and Purification of Single Crystals of Niobium," Radiation Metallurgy Section Solid State Division Progress Report for Period Ending February 1966, ORNL-3949, May 1966, p. 35.

Table 7. Major Metallic Impurities in Niobium as Determined by Spark Source Mass Spectrometry

Element	One Pass Zoned Refined Niobium (Weight ppm)
Fe	1
Hf	5
Mo	6
Ta	400
W	300
Zr	20

the primary slip system. A more detailed description of the slip geometry in the samples was given in an earlier report.[34]

The irradiations were carried out in Tube 12 of the Hydraulic Facility at the Oak Ridge Research Reactor. This facility permits sample insertion into and removal from position F-8 of the core while the reactor is at full power of 30 megawatts. During irradiation, pool water flows past the sample capsule to provide cooling. The bulk pool water temperature is generally greater than 90°F and must be kept below 100°F for the reactor to operate. To discharge the capsule the coolant flow is momentarily stopped while the direction of flow is reversed.

The final capsule design, shown in Figure 12, consisted of a cadmium tube 2-in.-long with a 9/32-in.-outside-diameter and 3/16-in.-inside-diameter. The tube was closed at each end with cadmium plugs which extended 7/32 in. into the tube such that the 1.5-in.-long sample had little freedom of movement. The end plugs permitted water to enter the cadmium tube and to flow past the sample but offered no direct line of sight to

[34] R. P. Tucker, R. E. Reed, and M. S. Wechsler, "Slip Line Observations on Irradiated Niobium Single Crystals," Radiation Metallurgy Section Solid State Division Progress Report for Period Ending February 1966, ORNL-3949, May 1966, p. 63.

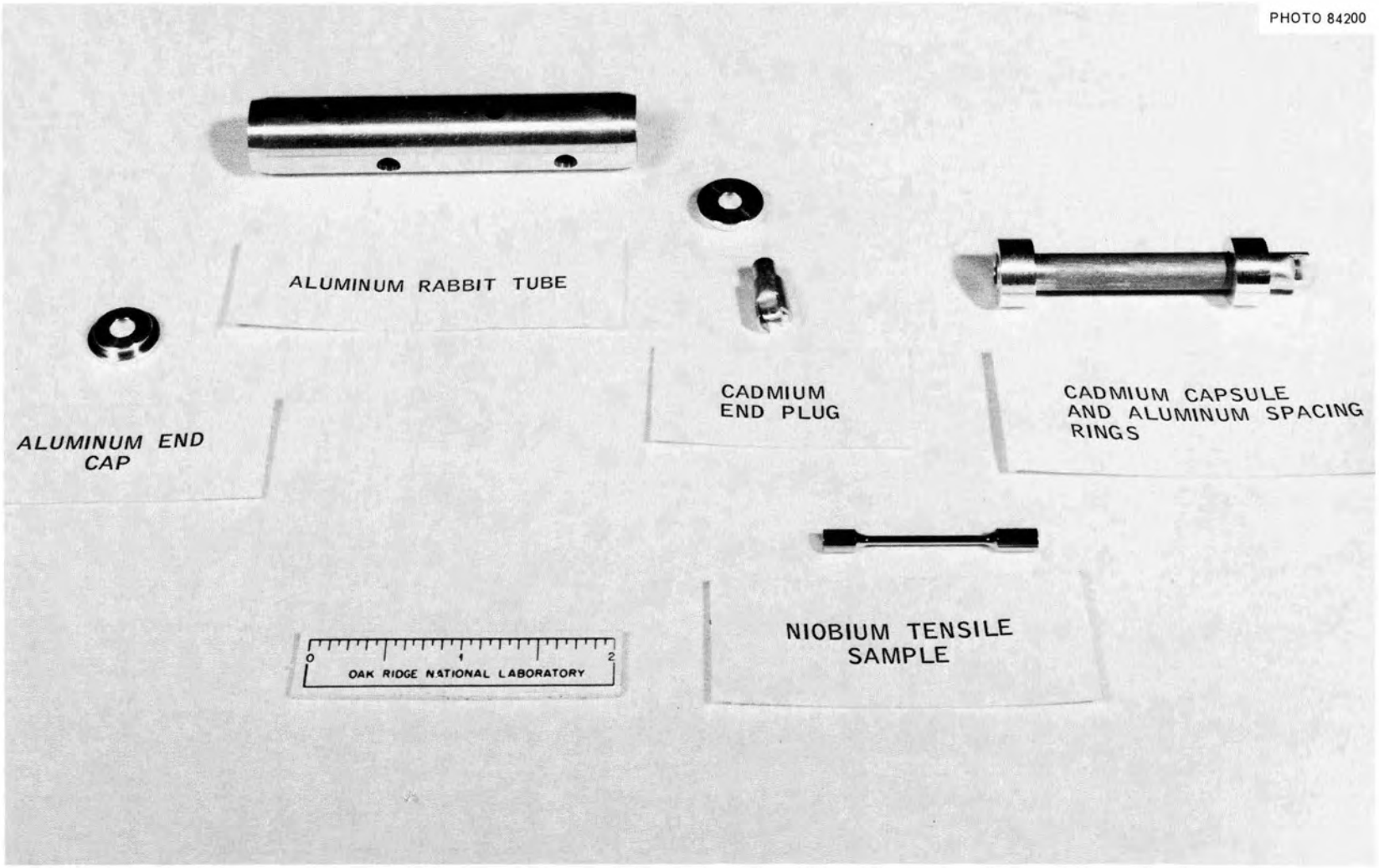

Fig. 12. Hydraulic Facility Capsule Assembly.

the neutrons. Two aluminum spacing rings were slipped on the ends of the cadmium tube to restrict its movement inside the perforated aluminum rabbit tube into which it was placed. The cadmium tube was enclosed in the aluminum rabbit by tapping the ends of the aluminum tube over to secure aluminum end caps. Cadmium, having a high cross-section for thermal neutrons, shielded the niobium from thermal neutrons in an attempt to keep the sample, post-irradiation activity to a minimum.

Two types of temperature monitors were used to estimate the irradiation temperature. For one irradiation using an aluminum inner capsule welded closed at each end, Wood's alloy melting at 73.0°C was included along with a niobium sample inside a cadmium foil wrapper. The temperature inside the capsule for one hour's irradiation exceeded the melting temperature of the Wood's alloy. In fact the cadmium foil stuck to the sample shoulder and the foil appeared to have melted in one region. This is not to say the temperature reached the melting point of cadmium as the Wood's alloy may have alloyed with the cadmium lowering its melting point. For this same irradiation the niobium sample was painted with five temperature sensitive lacquers for the range from 45 to 124°C. These lacquers are reported to be accurate to within ± 1 per cent. All of these lacquers appeared to have evaporated from the sample surface and were deposited on the cadmium foil. Additional tests were made in which the lacquers were painted on cadmium foil and included in the open-end flux determination capsules. From these tests the best estimate of the irradiation temperature, when water was in direct contact with the sample, is between 83 and 93°C.

The fast neutron flux in Tube 12 of the ORR-F-8 Hydraulic Facility was determined using as threshold monitors wires of iron, nickel, aluminum-0.103 weight per cent uranium-238, and an aluminum foil on which neptunium-237 was deposited. The monitors were shielded in approximately 50 mils of cadmium as were the niobium samples. The most reliable flux determination was for a 24-hour irradiation in which the monitors were sealed in quartz ampoules. The integral flux, $\Phi(E_i)$, above threshold energy E_i was calculated using the equation

$$\Phi(E_i) = \frac{A(t_i, t_w)}{N_o Y \sigma_{E_i} (1-e^{-\lambda t_i}) e^{-\lambda t_w}} \qquad (7)$$

where $A(t_i, t_w)$ is the activity in disintegrations per second upon irradiation for time t_i followed by a waiting time t_w, N_o is the initial number of detector atoms, Y is the fission yield of a fissionable isotope or the atomic abundance of a non-fissionable detector isotope, σ_{E_i} is the threshold cross section, and λ is the decay constant, $0.693/T_{1/2}$, where $T_{1/2}$ is the half-life of the activated isotope. The results of the fast flux measurements are given in Figure 13. Comment on the special problem which iron presents has previously been given.[35] For $^{237}Np[^{237}Np\ (n,f)\ ^{140}Ba]$ a radiochemical separation of ^{140}Ba was performed and the gross β activity counted from the reaction

$$^{140}Ba \xrightarrow{12.8\ \text{days}} {}^{140}La + {}_{-1}\beta^{o} + \lambda \qquad (8)$$

1.02 Mev (60%)
0.49 Mev (25%)

with a half-life of 12.8 days. The fission spectrum curve is also plotted

[35] J. M. Williams, W. E. Brundage, B. C. Kelley, and M. S. Wechsler, "The Position Five Facility in the Bulk Shielding Reactor," Radiation Metallurgy Section Solid State Division Prog. Rept., August 1965, ORNL-3878, p. 68.

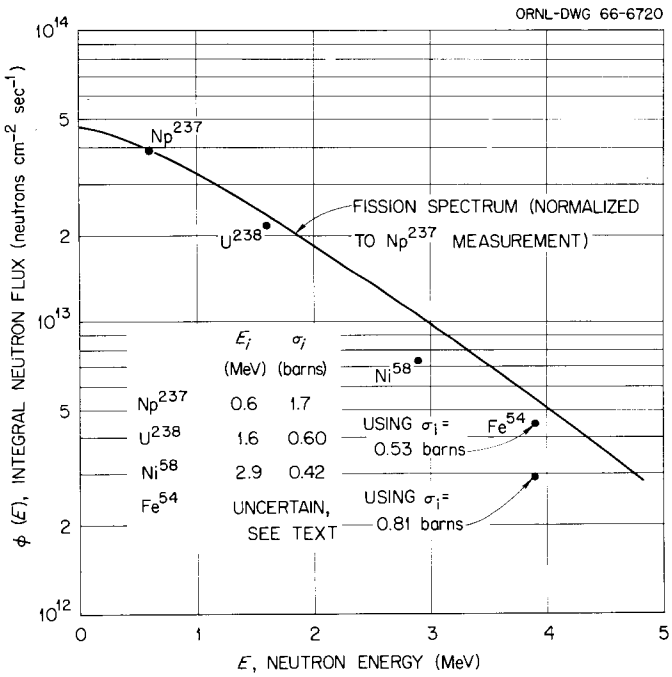

Fig. 13. Observed Integral Neutron Fluxes in Tube 12 of the ORR-F-8 Hydraulic Facility. The Fission Spectrum is shown for Comparison.

in Figure 13 for comparison. Based on the nickel monitor the flux in Tube 12 converted to energies greater than 1 Mev is 2.3×10^{13} neutrons/cm^2 sec. It was observed that refueling did not change the flux in Tube 12.

A qualitative activation analysis was run on a niobium sample 90 hours after it was irradiated for an hour. At that time the activity at 2 in. was 500 mr/hr; at 1 ft., 20 mr/hr. It was found that the major contributions to the activity were from the tantalum, tungsten, and hafnium impurities. The decay of ^{182}Ta and ^{187}W appears to be the source of the greatest portion of the activity.

The irradiation schedule included times from one minute to 24 hours, yielding doses from 1.4×10^{15} to 2.0×10^{18} neutrons/cm^2 (E > 1 Mev). A series of four samples all irradiated at 135°C in the Bulk Shielding Reactor to a dose of 4.2×10^{17} neutrons/cm^2 were tested along with the samples irradiated in the ORR.

The samples were tested in tension at room temperature on a table model Instron machine using split grips. All tests were carried out at a crosshead speed of 0.02 cm/min which for the 1.905 cm (0.75 in.) gage length corresponds to a strain rate of 1.75×10^{-4} sec^{-1}. Care was taken to align the sample in the grips. Prior to testing the sample was seated in the grips by a 1 kg preload.

Experimental Results and Discussion

Niobium single crystals were irradiated to nine doses in the range between 10^{15} and 10^{18} neutrons/cm^2, (E > 1 Mev). Upon testing in tension these crystals exhibited a variety of stress-strain behaviors and slip markings. Although each sample displayed an upper yield point, the shapes of the curves during the yield drop portion varied from a sharp drop to the lower yield stress to a rather gradual descent over an appreciable amount of strain, as shown in Figure 14. There does not appear to be a direct correlation between the shape of the yield point and the neutron dose. However, the results do suggest a trend toward an increase in the magnitude of the yield drop with increased dose. The magnitude of the yield drop increased rather consistently from 1 kg/mm^2 for the lowest dose of 1.4×10^{15} neutrons/cm^2 to 2.7 kg/mm^2 for the highest dose of 2.0×10^{18} neutrons/cm^2.

The slip markings of most of the samples were observed after straining to just beyond the lower yield stress. For low doses the slip line

[redacted]

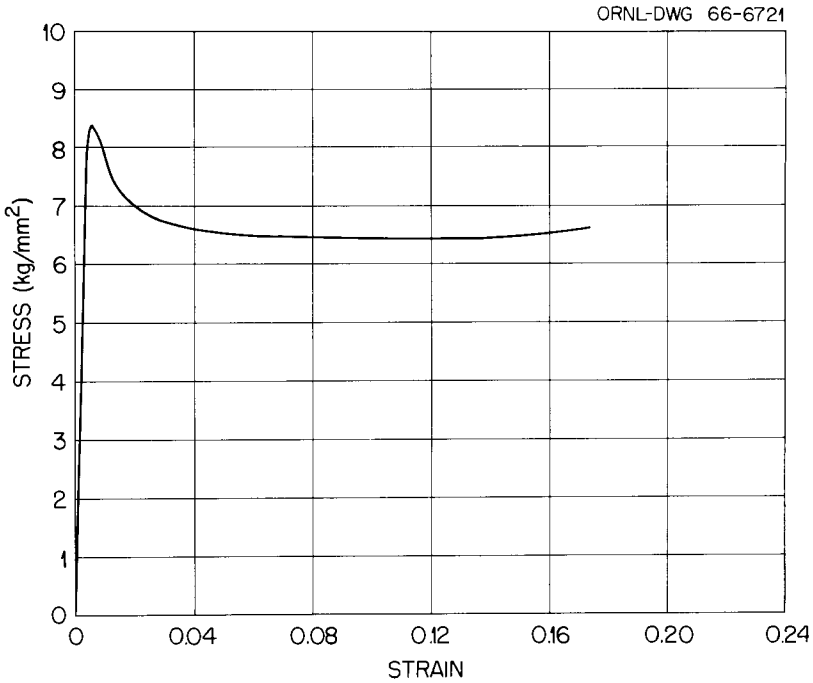

Fig. 14. Stress-Strain Curve for Single Crystal Niobium, Neutron Irradiated to 2.9×10^{17} neutrons/cm^2 (E > 1 Mev) at 90 ± 5°C.

pattern is not appreciably changed from that observed in unirradiated samples. However, there is some evidence to suggest that even at low doses the intensity of the slip step height is greater than that in the unirradiated samples for the same amount of strain. For doses of 10^{17} neutrons/cm^2 or greater the slip lines are usually widely spaced and intense and are connected by short cross slip segments. The intense lines broaden into bands as deformation increases. In the samples considerable variation in the density of slip lines was observed along the gage length as shown in Figures 15 and 16. The heterogeneity along the gage was attributable in part to the dimensional variation in the sample diameters. The poorest samples varied only ± 0.7 mil from the average diameters. The fact that the minimum diameter was always relatively near a shoulder, an area of stress concentration, resulted in the greatest deformation near one end of the gage and frequently much less visible deformation near the center.

In view of the above observations, the increase in the upper yield stress was taken as the measure of the radiation hardening. Figure 17 is a plot of the logarithm of the upper yield stress versus the logarithm of

[redacted]

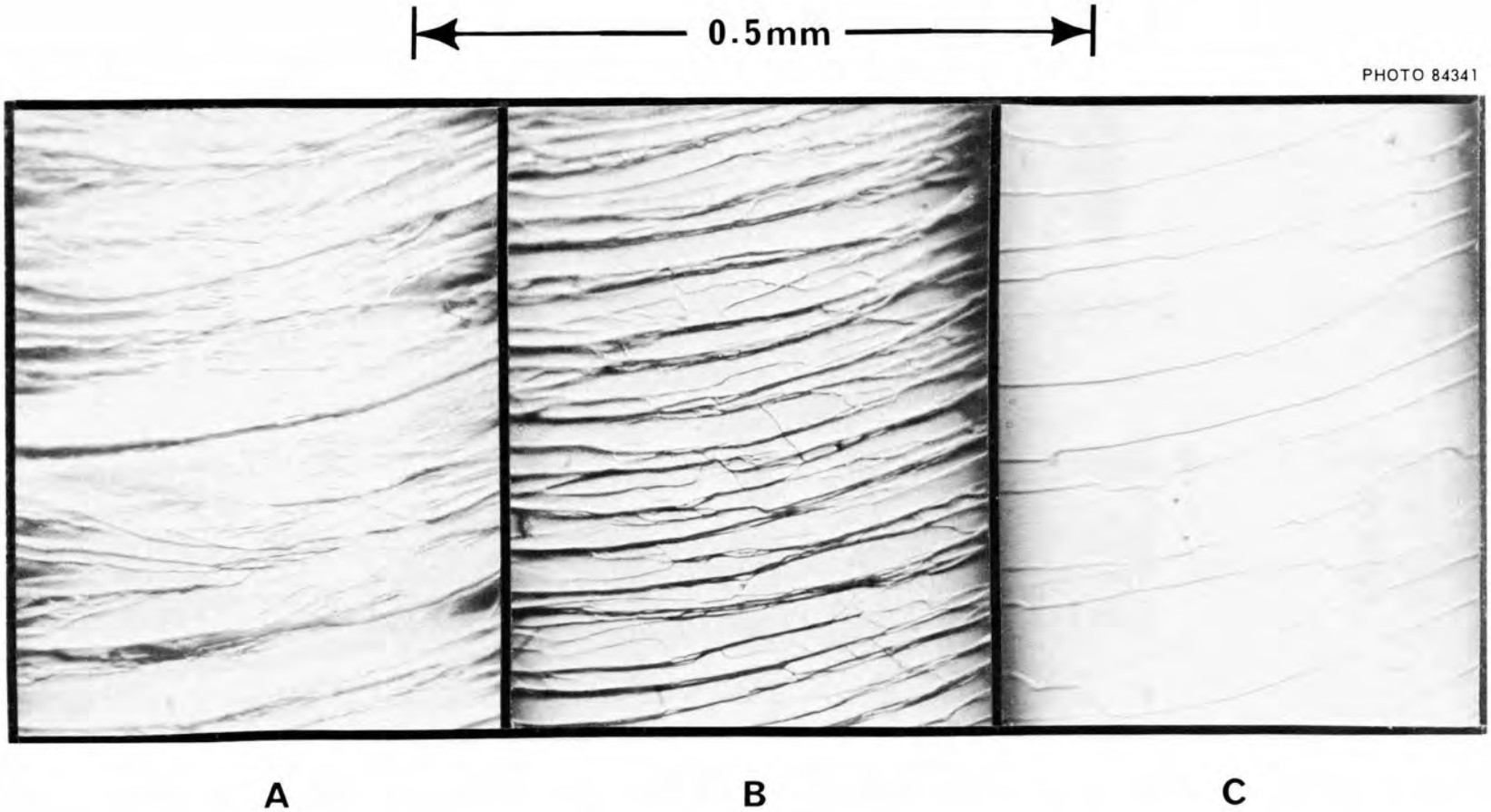

Fig. 15. Composite of Views of Slip Lines in a Sample Irradiated to a Dose of 1.7×10^{17} neutrons/cm^2 ($E > 1$ Mev): (A) Near Shoulder, (B) Toward Center, (C) Near Center.

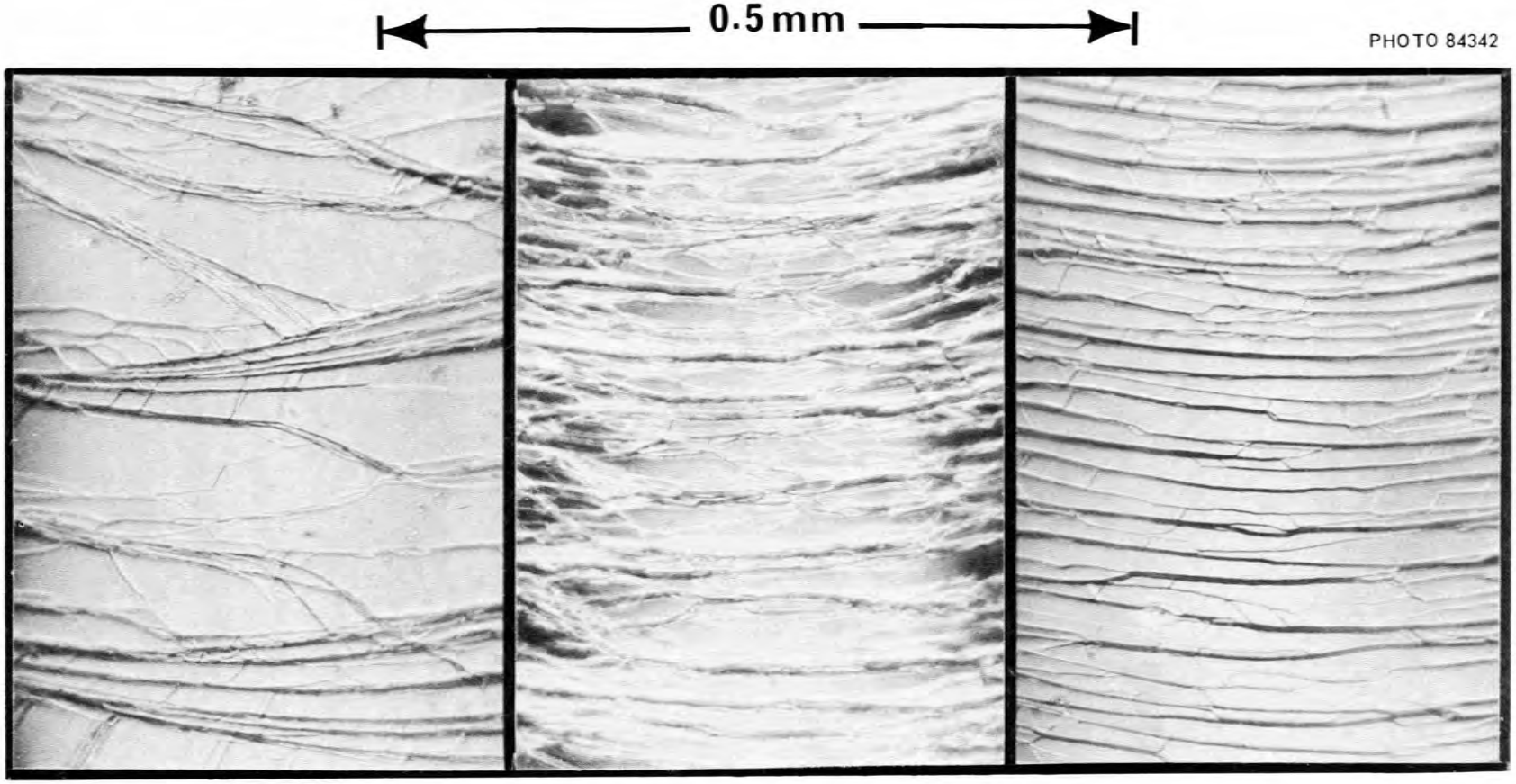

Fig. 16. Composite of Views of Slip Lines in a Sample Irradiated to a Dose of 2.9×10^{17} neutrons/cm^2 ($E > 1$ Mev): (A) Near Shoulder, (B) Toward Center, (C) Near Center.

[redacted]

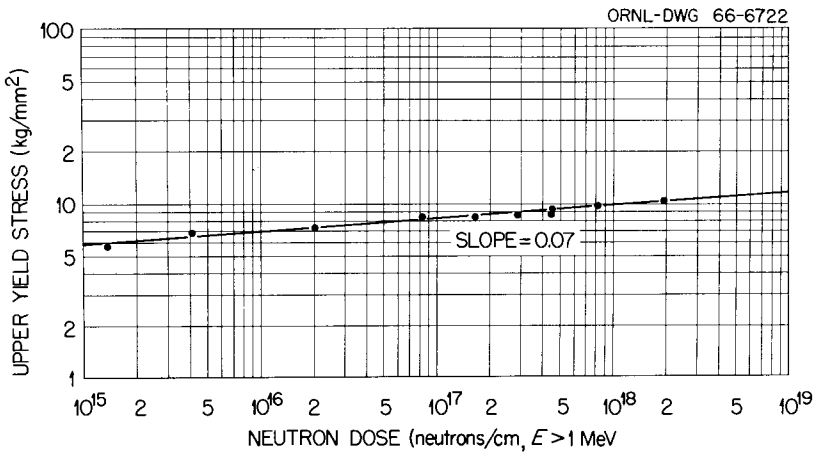

Fig. 17. Upper Yield Stress versus Neutron Dose for Niobium Single Crystals. Irradiation Temperature, 90 ± 5°C. Test Temperature, 25°C.

the neutron dose. The slope of the straight line through the points is 0.07. The size of the circles corresponds to the spread in the upper yield stress due to variations in cross sectional area along the gage length. The slope is of the same order as the 0.1 slope found by Hinkle et al.[31] for polycrystalline Ferrovac-E iron.

In body-centered cubic metals, in contrast to observations in face-centered cubic metals, the unirradiated material exhibits an upper yield stress which is of significant magnitude. Thus one finds for body-centered cubic metals that the increase in yield stress is usually considered to be the more significant property. An objection sometimes raised to subtracting the unirradiated upper yield stress from the irradiated value is that it has not been established that the increase in the upper yield stress upon irradiation is due to an additive cause. Since unirradiated face-centered cubic metals do not generally exhibit upper yield points and since the unirradiated yield stress is usually small compared to the irradiated, the dose dependence in face-centered cubic metals is relatively insensitive to the unirradiated yield stress. In body-centered cubic metals the relative magnitudes of the unirradiated and irradiated upper yield points are such that the dose dependence for the change in yield stress is appreciably different from that for the irradiated yield stress alone. The average of 15 upper yield stress values in the unirradiated niobium single crystals tested is 5.93 ± 0.52 kg/mm^2. The increase in the upper yield stress above the

[redacted]

average unirradiated upper yield stress is presented in Figure 18. The error bands correspond to the average deviation of the measurements of the unirradiated upper yield stress. The slope of the straight line through the points is 0.25. In order to test whether this one-quarter power dependence extrapolates with decreasing doses to the upper yield stress of the unirradiated niobium, the yield stresses were plotted versus $\Phi^{1/4}$ and the least squares straight line fit to the points for the irradiated samples was calculated. Fig. 19 shows that the line extrapolates well to the unirradiated value.

Stress Dependence of Dislocation Velocity in Irradiated and Unirradiated Niobium

H. D. Guberman

The dependence upon applied shear stress of the velocity of edge dislocations in single crystal niobium has been determined in several cases. The relationships were measured for non-irradiated material at room temperature and liquid nitrogen temperature, and at room temperature for material irradiated to a single dose level.

Measurements were made by means of the etch-pitting techniques previously described.[36] Static loading in a four point bending jig was used for all measurements. For liquid nitrogen temperature measurements, the sample was loaded in the bending jig and immersed in the bath as were the weights to be used. The load was applied when thermal equilibrium was established. The irradiated sample required no special handling other than that usually required by radio-active samples.

These samples were irradiated in the hydraulic facility of the Oak Ridge Research Reactor in cadmium shielding. They were exposed to a dose of 1.6×10^{17} neutrons/cm^2 ($E > 1$ Mev). They were allowed to decay for about five days in order to reach a manageable activity level, i.e. about 2.5 mr/hr on contact.

---

[36] H. D. Guberman, "Dislocation Etch Pits in Niobium," Radiation Metallurgy Section Solid State Division Progress Report for Period Ending August 1965, ORNL-3878, p. 49; February 1966, ORNL-3949, p. 56.

[redacted]

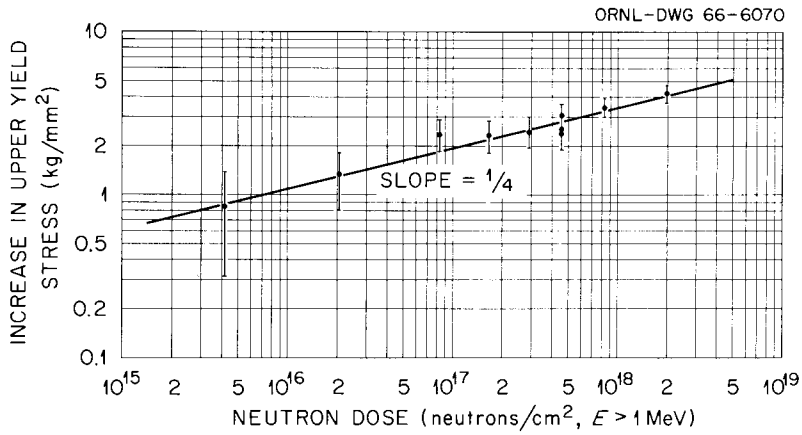

Fig. 18. Increase in Upper Yield Stress versus Neutron Dose for Niobium Single Crystals. Irradiation Temperature, 90 ± 5°C.

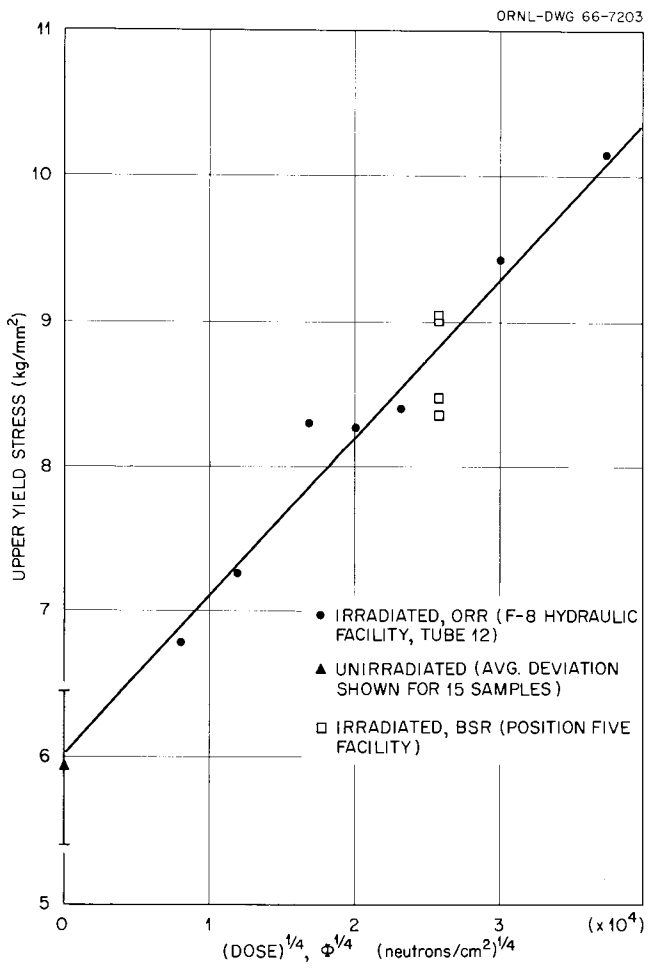

Fig. 19. Upper Yield Stress versus the Fourth Root of the Dose for Single Crystals of Niobium. Irradiation Temperatures: ORR, 90°C; BSR, 135°C.

[redacted]

[redacted]

The results of these measurements are shown in Fig. 20. They are plotted in accordance with the expression:

$$\bar{v} = (\tau/\tau_o)^m . \tag{10}$$

The parameters for the three cases are given in Table 8. Over the range considered, the data fit reasonably well to Eq. 10.

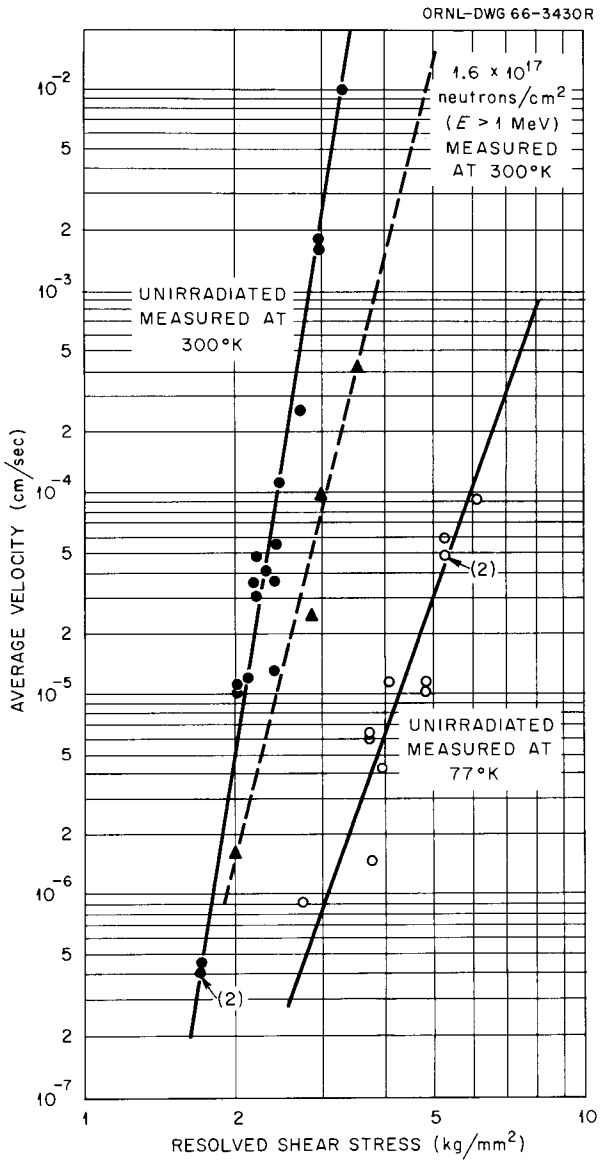

Fig. 20. Average Dislocation Velocity as a Function of Applied Shear Stress.

[redacted]

Table 8. Dislocation Mobility Parameters

Sample	m	τ_o
Non-Irradiated, 300°K	15	4.4
1.6×10^{17} n/cm^2, 300°K (E > 1 Mev)	10	7.7
Non-Irradiated, 77°K	6	30

It has been suggested by Gilman[37] that a more appropriate way to express the stress dependence of the dislocation velocity is an expression of the form:

$$v = v_o e^{-D/\tau} \tag{11}$$

where v_o is a limiting velocity near the velocity of sound, D is a characteristic drag stress, and τ the applied shear stress. The room temperature data are replotted in Fig. 21 according to Eq. 11. While the logarithm of the average dislocation velocity appears to be linearly related to the reciprocal shear stress as predicted by Eq. 11, the intercepts are considerably below the shear wave velocity in niobium (2.10×10^5 cm/sec).[38] It is significant that Schadler's data[39] of dislocation mobility in tungsten, when plotted according to Eq. 11, also intercepts the axis at a velocity of about 10^3 cm/sec.[2] This too is considerably below the shear wave velocity in tungsten. Thus Gilman's treatment appears to fit insofar as the functional relationship is concerned, but the intercepts do not follow as expected. For body-centered cubic metals, only the silicon-iron data of

---

[37] J. J. Gilman, "Dislocation Mobility in Crystals," J. Appl. Phys. 36, 3195 (1965).

[38] G. L. Miller, p. 396 in Tantalum and Niobium, Butterworths Scientific Publications, London, 1959.

[39] H. W. Schadler, "Mobility of Edge Dislocations on {110} Planes in Tungsten Single Crystals," Acta Met. 12, 861 (1964).

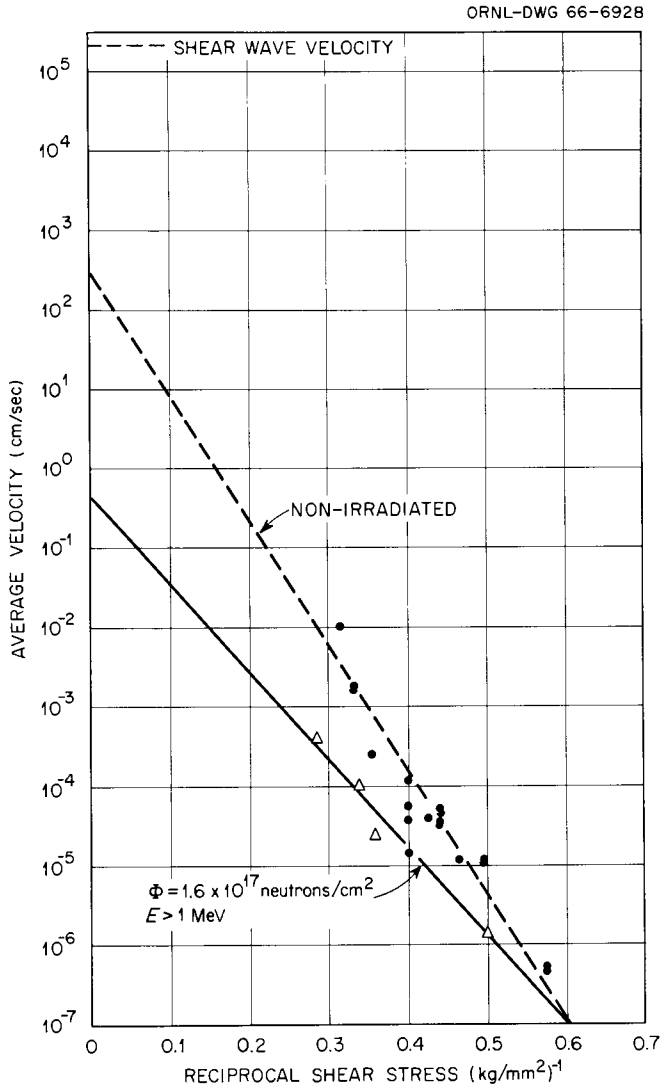

Fig. 21. Average Dislocation Velocity versus Reciprocal Shear Stress.

Stein and Low[40] provide an intercept greater than that for the shear wave velocity. Gilman[37] was able to adjust this case to fit his theory by considering the effects of long range stress fluctuations.

---

[40] D. Stein and J. Low, "Mobility of Edge Dislocation in Silicon-Iron Crystals," J. Appl. Phys. 31, 362 (1960).

Estimates of the internal stress fields in the niobium crystals are available[41] from a study utilizing a stress relaxation technique.[42] When the data are corrected to determine the effective stress by taking into account the internal stress field, the slope is decreased (Fig. 22) as in the case with Stein and Low's data, but now however, the intercept is still

---

[41] R. P. Tucker, Private communication.

[42] S. M. Ohr, "A Study of Radiation Hardening in Iron by Stress Relaxation Techniques," Radiation Metallurgy Section Solid State Division Progress Report for Period Ending August 1965, ORNL-3878, p. 16.

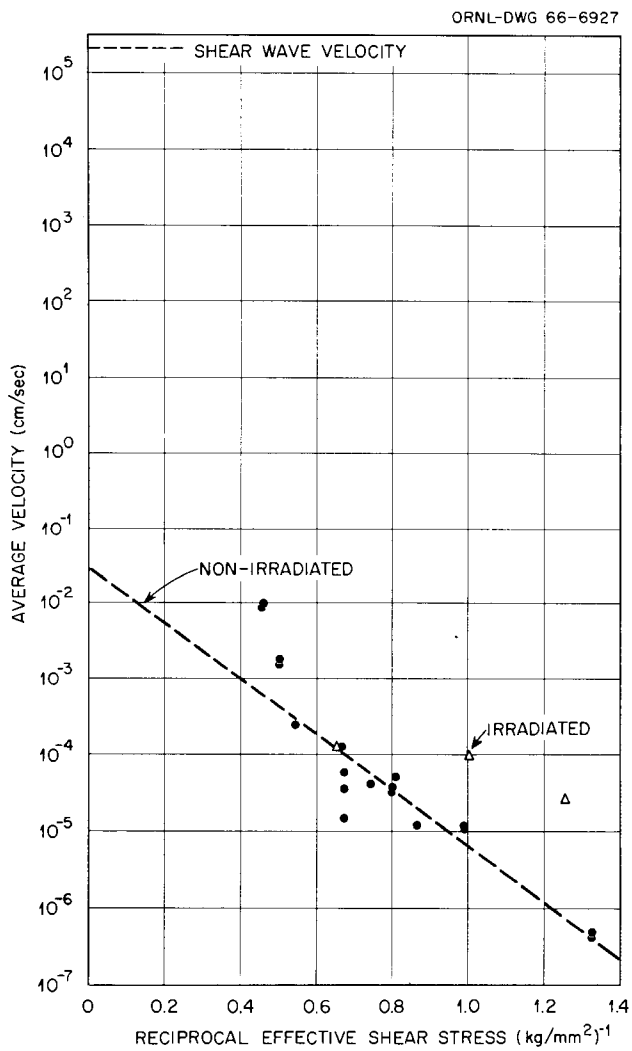

Fig. 22. Average Dislocation Velocity versus Reciprocal Shear Stress Corrected for Internal Stress Field.

further below that of the shear wave velocity. No curve is drawn for the irradiated material because the data are too sparce and the magnitude of the internal stress field is not yet well established.

It is apparent from the above considerations that further work must be done to elucidate the nature of the parameter v_o in Eq. 11. It also appears that internal stress field corrections as suggested by Gilman are inappropriate in relatively pure body-centered cubic metals.

When the dislocation mobility measurements are considered in conjunction with the results of deformation studies in similar material[43] some interesting points emerge. In Table 9 are presented yield stress data for two crystals in the non-irradiated and irradiated condition. These crystals were grown in an identical manner from identical starting material as those used for the mobility measurements.

Considering the lower yield stress first, the stress-strain curves are of a form consistent with uniform yielding. Thus at the local minimum where the elastic strain rate is zero, the plastic strain rate may be taken as:

$$\dot{\epsilon} = \dot{\epsilon}_p = 0.5 b \rho \bar{v} \tag{12}$$

[43] R. P. Tucker, This report.

Table 9. Summary of Yield Point and Associated Dislocation Mobility Data*

Sample	UYS (kg/mm^2)	LYS (kg/mm2)	$\bar{v}$ at UYS (cm/sec)	$\bar{v}$ at LYS (cm/sec)	Mobile Density at LYS (cm^{-2})
Non-Irradiated	2.75	2.26	7.5×10^{-4}	3.0×10^{-5}	3.5×10^{8}
$= 1.7 \times 10^{17} n/cm^2$ (E > 1 Mev)	4.13	3.24	1.6×10^{-3}	1.7×10^{-4}	6.1×10^{7}

*All stress values are true stress.

where $\dot{\epsilon}$ is the total applied strain rate, $\dot{\epsilon}_p$ is the plastic strain rate, b the Burger's vector, ρ the mobile dislocation density, and $\bar{v}$ the average dislocation velocity. The dislocation velocity at the lower yield point may be found from Fig. 20 and the known values of the stress. Thus it is determined that in the irradiated condition the average velocity is almost a factor of six greater than that for the non-irradiated case. As a further consequence, making use of Eq. 12, one finds that the mobile dislocation density in this irradiated sample has been reduced by about a factor of six compared to the non-irradiated case. (Values are summarized in Table 9). One can only speculate on the reasons for the decreased mobile density which requires more detailed study.

Little can be said about the respective dislocation multiplication rates during the yield process. The simple state of affairs assumed by Eq. 12 does not apply at the upper yield stress. Thus one cannot determine the mobile density just at or immediately prior to the upper yield point. Perhaps this might be determined from an etch pit count under static conditions in the preyield region as well as from stress relaxation data in the same region.

By a similar treatment knowing the stress at the upper yield point, one determines that the average dislocation velocity for the non-irradiated and irradiated samples are 7.5×10^{-4} and 1.6×10^{-3} cm/sec respectively, which are within a factor of two of each other. This is not a large difference considering the nature of the data involved. In fact the average value for the upper yield stress from a fairly large number of unirradiated samples would indicate a dislocation velocity of about 1.9×10^{-3} cm/sec with an average deviation such that the value for the sample chosen lies near the lower end of the spread in velocities. This suggests that an important factor in determining the onset of yielding is the dislocation velocity. In particular, a critical velocity may be required to initiate the processes which lead to the rapid multiplication of dislocations and the consequent drop in stress. These data, sparce though they are, fit in well with recent suggestions concerning the yield process.[44] Additional work is

---

[44] S. M. Ohr, Private communication.

being done at present to confirm (or reject) the hypothesis that the onset of yielding is governed by a critical dislocation velocity.

The Interaction of Radiation Produced Defects and Interstitial Impurity Atoms in Niobium

J. T. Stanley and W. E. Brundage

At the present time it is thought that interstitial impurity atoms play an important role in the annealing of radiation damage in body-centered cubic metals. Rosenfield[45] has suggested that the so-called Stage III annealing in radiation damaged and cold worked body-centered cubic metals is in fact associated with migration of interstitial impurity atoms to radiation produced defects. On the other hand, there is little direct evidence that interstitial impurity atoms do indeed interact with radiation produced defects. Only for the case of carbon[46] and nitrogen[47] in iron has evidence been presented for the existence of such an interaction. It is known from previous work that the interstitial impurities oxygen, carbon, and nitrogen in niobium cause internal friction peaks at temperatures characteristic of each impurity.[48] We have used these internal friction peaks to study the behavior of the interstitial impurities in neutron irradiated niobium. We have obtained evidence that the interstitial impurity oxygen in niobium interacts with radiation produced defects.

Specimen Preparation

Zone refined niobium rod, 1/4-in.-diameter, was swaged and drawn to 0.030-in.-diameter wire without intermediate anneals. The wire was etched

---

[45] A. R. Rosenfield, "Recovery of Cold Worked Body-Centered Cubic Metal," Acta Met. 12, 119 (1964).

[46] H. Wagenblast and A. C. Damask, "Kinetics of Carbon Precipitation in Irradiated Iron," J. Phys. Chem. Sol. 23, 221 (1962).

[47] J. T. Stanley and W. E. Brundage, "The Effect of Irradiation on Precipitation of Nitrides in Alpha Iron," Radiation Metallurgy Section Solid State Division Progress Report for Period Ending August 1965, ORNL-3878, p. 2.

[48] R. W. Powers and Margaret V. Doyle, "Diffusion of Interstitial Solutes in the Group V Transition Metals," J. Appl. Phys. 30, 514 (1959).

lightly, placed in a vacuum chamber, and annealed for about 10 minutes at approximately 1800°C in a vacuum of 10^{-5} torr by passing current through the wire. The impurity content of this material is given in Table 10.

Internal Friction Measurements in Unirradiated Niobium

Figure 23 presents results of internal friction measurements made on unirradiated niobium in the temperature interval from 110 to 350°C using a torsion pendulum. As expected from previous work, internal friction peaks corresponding to oxygen and nitrogen in solid solution were found.[48] These peaks were stable with time. Also, as expected, a transient internal friction response was observed in the temperature interval from 200 to 300°C. This transient internal friction annealed out during the time required to complete the first series of measurements, which were made with increasing temperature. This transient internal friction is almost certainly due to carbon retained in solution during the rapid cooling from the

Table 10. Chemical Composition of Niobium Samples in Weight PPM

Impurity	Zone refined 1/4" rod	Annealed 0.030" wire	
	Vacuum fusion	Vacuum fusion	Internal friction
O	27 ± 6	54	40
C	13 ± 6		
N	15 ± 6	5	7.7
Ta	368		
W	228		
Zr	10		
Cr	< 1		
Cu	< 1		
Fe	< 1		
Mg	< 1		

[redacted]

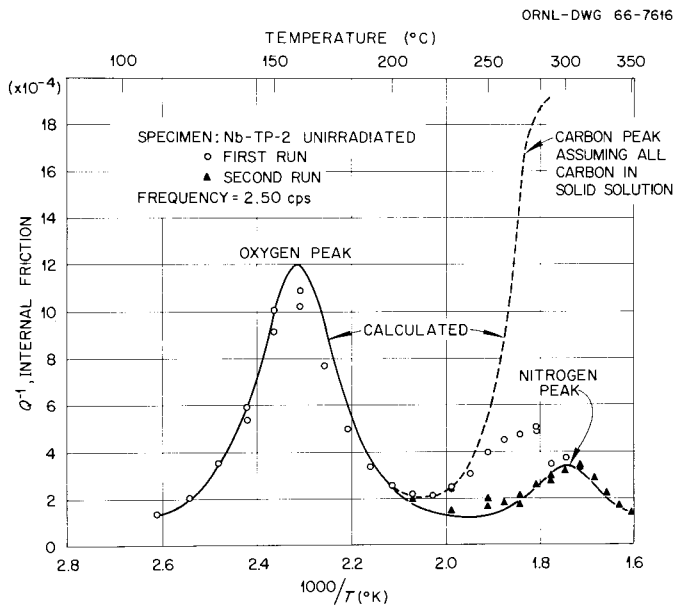

Fig. 23. Internal Friction versus Test Temperature for Unirradiated Niobium.

1800°C annealing temperature given the specimen prior to the internal friction measurements. Since the solubility of carbon is practically zero at 300°C, the carbon precipitates from solution at temperatures where the mobility of carbon becomes appreciable (about 240°C). The two peaks in solid curve in Fig. 23 were each obtained by fitting the data to the equation

$$Q^{-1} = \frac{\Delta_M}{2} \cdot \frac{2\omega\tau}{1 + \omega^2\tau^2} + Q_{BG}^{-1} \tag{13}$$

where Q^{-1} is the measured internal friction, $\frac{\Delta_M}{2}$ is the height of the internal friction peak, ω is the measured angular frequency of the pendulum, τ is the relaxation time for the interstitial, and Q_{BG}^{-1} is the background damping which is assumed to be constant in the temperature interval of the peak. The value of τ is given as a function of temperature by

$$\tau = \tau_o e^{\Delta H/RT} \tag{14}$$

where τ_o is the relaxation time at $1/T = 0$, and ΔH is the activation energy for diffusion of oxygen or nitrogen in niobium. Values of

[redacted]

activation energies and τ_o's for the three interstitial impurities were obtained from the work of Powers and Doyle[48] and are listed in Table 11. Equation 13 was used to fit a curve to the two stable internal friction peaks by determining values for $\frac{\Delta_M}{2}$ and Q_{BG}^{-1} using a least square analysis. The solid curve shown in Figure 23 was then drawn using the sum of the two peaks in the temperature interval where there was overlap. The values of Q_{BG}^{-1} determined for the two peaks were only slightly different so their average value was used for the background over the entire range. The fit to the data points obtained by this procedure was quite good, but a somewhat better fit could have been obtained by using a slightly different peak temperature (about 2° lower for the oxygen peak) than that obtained from the parameters in Table 11. The heights of the oxygen and nitrogen peaks were used to estimate the amounts of oxygen and nitrogen in solution using conversion factors determined by Powers and Doyle.[48,49] The results are listed in Table 10 for comparison with chemical analysis. The agreement is satisfactory.

As previously mentioned there is a transient internal friction in the temperature interval from 200 to 300°C which anneals out during the time required to complete the first series of measurements. This internal friction is most likely caused by carbon in solution since Powers and Doyle[48] showed that carbon does produce an internal friction peak in this temperature range which is not stable with time. We attempted to determine what

---

[49] R. W. Powers and Margaret V. Doyle, "Some Internal Friction Studies in Columbium," Trans. AIME 9, 1285 (1957).

Table 11. Values of Activation Energy and Pre-Exponential Factors Used in Data Fitting

Interstitial	τ_o, sec x 10^{-15}	ΔH, peak temp. cal/mole	ΔH, peak shape cal/mole
Oxygen	1.44	26,910	26,400
Carbon	7.57	33,020	33,000
Nitrogen	3.52	34,920	34,520

the height of this peak would have been if all of the carbon initially in solution had remained in solution during the measurements. This was done by subtracting the calculated curve described above from the data points obtained during the first run. The data points so obtained were plotted versus the quantity, $\left(\frac{\omega\tau}{1 + \omega^2\tau^2}\right)$, where the τ values for each temperature were determined from the constants in Table 11. This plot should yield a straight line through the origin with a slope equal to $\frac{\Delta_M}{2}$. In this instance the points taken at temperatures above 230°C deviate from a straight line due to the precipitation of carbon during the time used for measurements. However, points taken at temperatures below 230°C did fall on a straight line and these were used to obtain the carbon peak height. The peak so obtained is shown as a dashed curve in Fig. 23. The peak height is consistent with the amount of carbon given by chemical analysis.

Irradiation Procedure and Results

The specimen was irradiated twice and internal friction measurements were made after each irradiation. The first irradiation was done in the Bulk Shielding Reactor in the Liquid Nitrogen Cryostat.[50] The specimen was given an exposure of 2.6×10^{17} neutrons/cm^2 (E > 1 Mev) at an irradiation temperature of −160°C. The results of internal friction measurements made after this irradiation are shown in Fig. 24. In this case data are grouped into two runs since there again is a transient source of internal friction in the temperature interval between the oxygen and nitrogen peaks. After the aging away of this transient, the oxygen and nitrogen internal friction peaks are the same height as before irradiation. The temperature of the peaks seems to have shifted towards higher temperatures relative to the position indicated by the parameters given in Table 11. We do not know yet whether this is an effect of irradiation or due to some error in temperature measurement. There is some indication that the effect is due to irradiation since the same result was obtained after the second irradiation

[50] B. C. Kelley and C. E. Klabunde, "Irradiation Facilities in the Oak Ridge National Laboratory Bulk Shielding Reactor," Paper presented at International Symposium on Developments in Irradiation Capsule Technology, Pleasanton, Calif., May 3-5, 1966. To be published in TID-7697, Part 2.

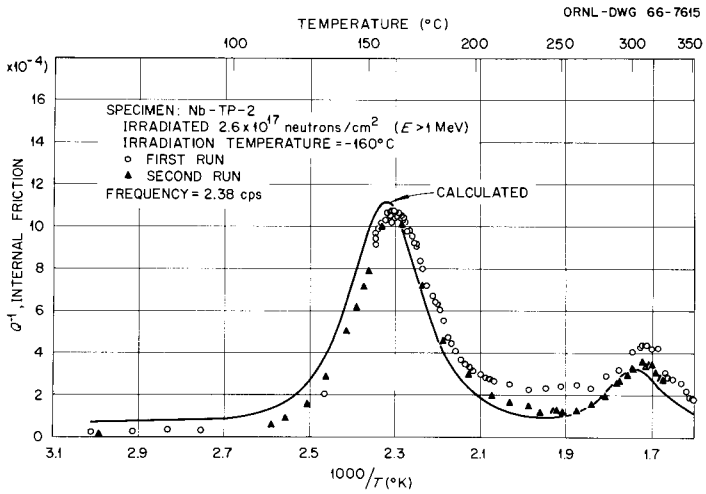

Fig. 24. Internal Friction versus Test Temperature for Niobium after Irradiation to 2.6 x 10^{17} neutrons/cm^2 (E > 1 Mev).

described below and also there appears to be a slight narrowing of the peak after irradiation. A narrowing of the peak corresponds to a higher activation energy and this is consistent with a shift to higher temperature.

The second irradiation was carried out in the Position Five Facility of the BSR.[51] In this case the specimen was given a fast neutron exposure of 8 x 10^{17} neutrons/cm^2 (E > 1 Mev) at a temperature of 50°C. The results of internal friction measurements made after this irradiation are shown in Fig. 25. Here the results have been divided into four runs to help separate the effects observed after a somewhat involved heating cycle. In the first run measurements were made at rather widely spaced temperature intervals up to 310°C. The oxygen peak appears to be about the same height as before irradiation. Again there appears an increase of internal friction above the preirradiation value in the temperature interval 200-300°C. The measurements marked second run were made in the vicinity of the oxygen peak for a period of about 40 hours. These measurements show that a decrease in the height of the oxygen peak occurred during the first run heating, but no

---

[51] J. M. Williams, W. E. Brundage, B. C. Kelley, and M. S. Wechsler, "The Position Five Facility in the Bulk Shielding Reactor," Radiation Metallurgy Section Solid State Division Progress Report for Period Ending August 1965, ORNL-3878, p. 68.

[redacted]

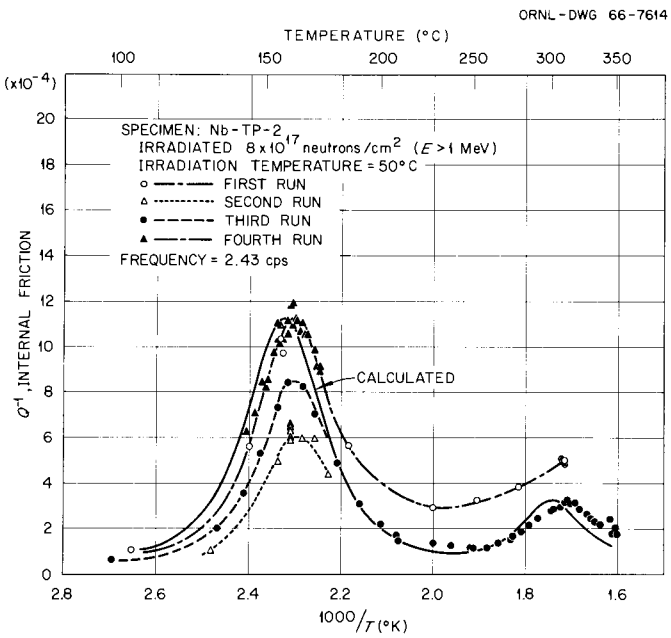

Fig. 25. Internal Friction versus Test Temperature for Niobium after Irradiation to 8 x 10^{17} neutrons/cm^2 (E > 1 Mev).

further change in the oxygen peak occurred during the subsequent 40 hours at 130 to 160°C. During the third run the temperature was raised to 350°C and then measurements were made with decreasing temperature. The nitrogen peak has about the same value as the preirradiation value. Some recovery of the oxygen peak is observed during this third run. Finally the fourth run shows results for the oxygen peak after annealing 6 hours at 400°C. After this treatment the oxygen peak is about the same height as the pre-irradiation value.

Discussion of Results

A. Nature of Stage III Annealing in Niobium

We believe that these internal friction results support the contention that the so-called Stage III annealing in niobium is really caused by oxygen atoms migrating to radiation produced defects. There are at least three arguments for this position:

1). As pointed out by Rosenfield[45] the activation energy for Stage III annealing (1.2 ev) and oxygen diffusion (1.17 ev) are identical within experimental error.

[redacted]

2). We have shown that oxygen is trapped by some sort of defect produced by irradiation. Although we have not yet obtained the kinetics for trapping of oxygen the time and temperature during which oxygen became trapped in run 1, Fig. 25, is reasonable for oxygen migration. Also it may be pointed out that if the defects moved to the oxygen atoms it seems reasonable to suppose that some of the nitrogen atoms would have also been trapped.

3). The actual magnitude of decrease of electrical resistivity in Stage III observed by Peacock and Johnson[52] is in agreement with the decrease expected if oxygen is responsible for this annealing stage. We observed a decrease of the oxygen peak corresponding to an oxygen concentration of 18 ppm after a fast neutron dose of 8×10^{17} neutrons/cm^2 ($E > 1$ Mev). Our results suggest that the traps are only able to absorb a fixed amount of oxygen per trap. Therefore, for Peacock and Johnson's irradiation to a dose of 2×10^{18} neutrons/cm^2 ($E > 1$ Mev), we would expect the traps to absorb 45 ppm oxygen. Peacock and Johnson found a resistivity decrease of 0.2μohm in Stage III for the irradiation dose of 2×10^{18} neutrons/cm^2 ($E > 1$ Mev). The resistivity increase caused by oxygen in solution has been found to be 3.9×10^{-3}μohm per ppm of oxygen.[53] Forty five ppm of oxygen therefore corresponds to a resistivity increment of .175μohm, which is in reasonable agreement with observations.

B. The Nature of the Oxygen Traps in Niobium

Very little information is available as to the nature of the defect structure which traps oxygen. It might be useful to point out that the ratio of trapped oxygen atoms to Frenkel defects produced is small. We found that 105 atom ppm was trapped for a fast neutron dose of 8×10^{17} neutrons/cm^2 ($E > 1$ Mev). For a scattering cross section of 5×10^{-24} cm^2 and 400 Frenkel pairs per primary knock on, we obtain about 16 Frenkel

---

[52] D. E. Peacock and A. A. Johnson "Stage III Recovery in Neutron Irradiated Molybdenum and Niobium," Phil. Mag. 8, 563 (1963).

[53] C. S. Tedmon, Jr., R. M. Rose, and J. Wulff, "Controlled Addition of Small Amounts of Oxygen to Niobium (Columbium)," Trans. AIME 230, 1732 (1964).

pairs per trapped oxygen atom. For the case of carbon and nitrogen interstitial impurities in iron, Wuttig, Birnbaum, and Stanley[54] have suggested that trapping by interstitial clusters is the dominant mechanism after neutron irradiation.

C. The Connection Between Oxygen in Niobium and Radiation Hardening

Makin and Minter[55] irradiated niobium tensile samples at 16°C to a fast neutron dose of 1×10^{20} neutrons/cm^2 (E > 1 Mev). They found an increase in yield stress of about 15,000 psi after the irradiation, but samples annealed in the temperature interval 150 to 200°C showed a further 15,000 psi increase of tensile strength. Furthermore, they found that the increase upon annealing occurred with an activation energy of 1.3 ± .1 ev. This activation energy corresponds to the activation energy for oxygen diffusion (1.17 ± .01 ev) within experimental error. Annealing at higher temperatures produced a decrease of yield stress beginning at 350°C. The yield stress decreased to the preirradiation value after 1 hr at 600°C. The temperature range of recovery of yield stress is not inconsistent with our observations of the recovery of the oxygen peak (6 hours at 400°C).

D. On the Nature of the Transient Increase of Internal Friction in the Temperature Interval 200-310°C after Irradiation

We presently believe that the increase of internal friction in the temperature interval 200-310°C is caused by carbon being put back into solution during the irradiation. The mechanism for this process involves break-up of carbide precipitates by displacement spikes. The evidence supporting this view is that the temperature interval in which the increase occurs corresponds to the interval in which the carbon internal friction peak is observed. Stage III annealing is also observed for metals such as Mo[52] which have very low solubilities of interstitial impurities. For these cases we believe that the mechanism described above

---

[54] M. Wuttig, H. Birnbaum, J. T. Stanley, "Interstitial Solute Trapping in Irradiated and Quenched Iron," submitted for publication.

[55] M. J. Makin and F. J. Minter, "The Mechanical Properties of Irradiated Niobium," Acta Met. 7, 361 (1959).

could put interstitial impurities in solution and upon subsequent annealing these impurities would migrate to traps to cause the observed change in properties.

Fission Flux Converter Facility for the BSR

W. E. Brundage

The Fission Spectrum Irradiation Facility, planned for the Bulk Shielding Reactor, has been discussed previously.[56,57] This facility will provide a flux of about 2.2×10^{12} neutrons/cm^2 sec which will closely approach a pure fission neutron spectrum. Specimens up to a 3-in.-diameter and 6-in.-long can be irradiated in the facility. The irradiation source is a sleeve containing ^{235}U which surrounds the sample chamber. Thermal neutrons from the BSR will be moderated by passing through D_2O and absorbed in the ^{235}U of the sleeve to provide the fission neutrons.

Moderating materials are minimized in a region around this sleeve to reduce the feed back of partly moderated neutrons to the sample chamber and calculations show that over 95% of the displacement damage produced in the specimens will be caused by neutrons in the fission spectrum.

The detailed design of the facility is now being carried out. The general features are similar to the earlier concept[56] except that the moderating D_2O tank at the side of the reactor will be separated from the converter facility housing. The reactor, which is moveable, and moderating tank will be positioned as required to vary the thickness of the light water between the housing and the tank. This will provide a method of reducing and controlling the thermal neutron flux incident on the converter sleeve and thus regulating the fissioning rate in this sleeve.

---

[56] W. E. Brundage, "A Converter Facility for Providing Fission-Spectrum Neutrons in the Bulk Shielding Reactor," Fuels and Materials Development Program Quart. Progr. Rept. March 31, 1965, ORNL-TM-1100, p. 87.

[57] W. E. Brundage and E. B. Johnson, "Criticality Tests on the Converter Facility for the Bulk Shielding Facility," Radiation Metallurgy Section Solid State Division Progress Report for Period Ending August 1965, ORNL-3878, p. 75.

[redacted]

Fig. 26 illustrates the active element and sample tube. Fig. 27 is the plan view of the facility. The D_2O tank is mounted on the reactor frame and the remainder of the housing is located permanently in the pool. The vertical section of the facility is illustrated in Fig. 28.

The detailed design of the facility is nearing completion. The only portion not complete is the detailing of the piping locations external to the reactor.

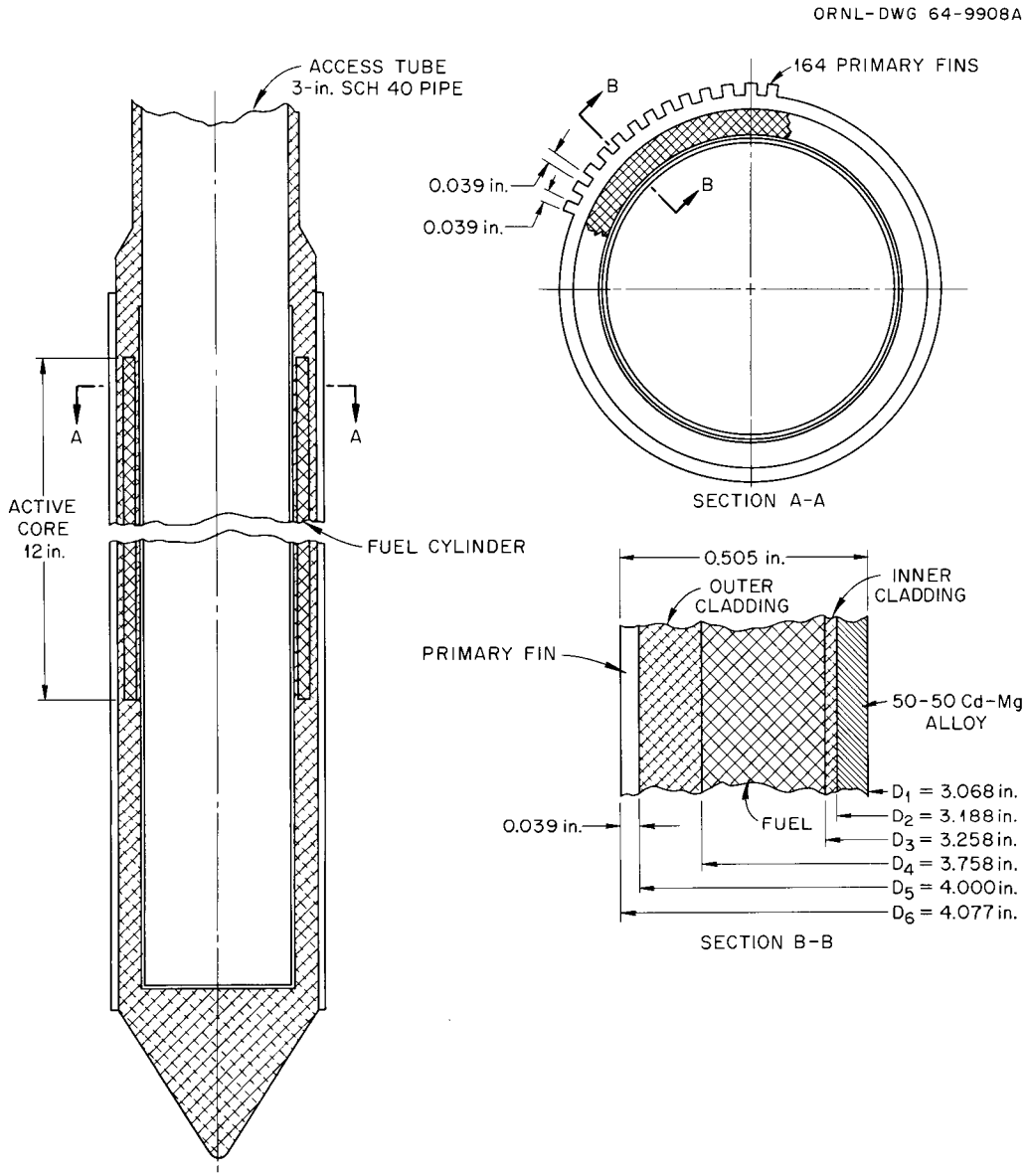

Fig. 26. Fuel Element Details.

[redacted]

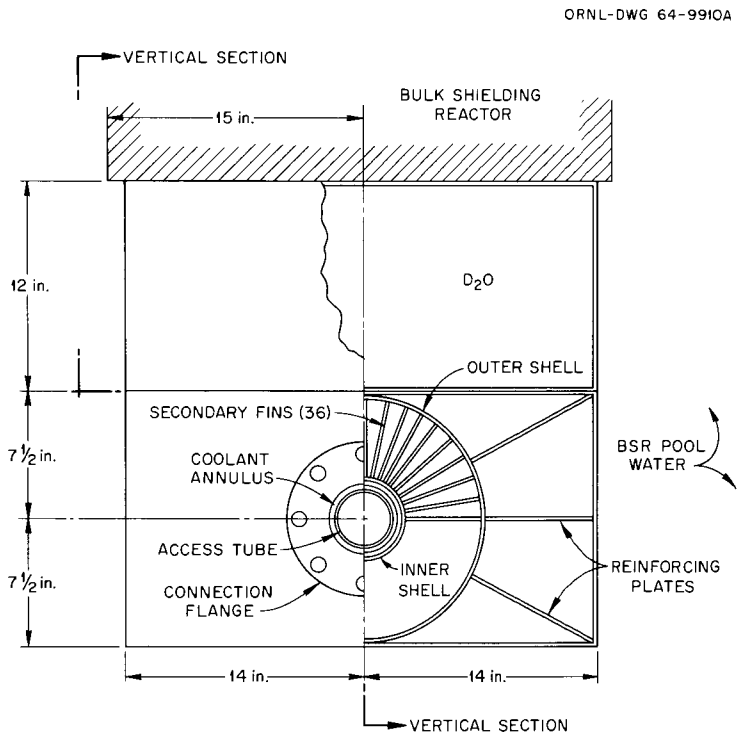

Fig. 27. Plan View of Tank and Fuel Element Assembly.

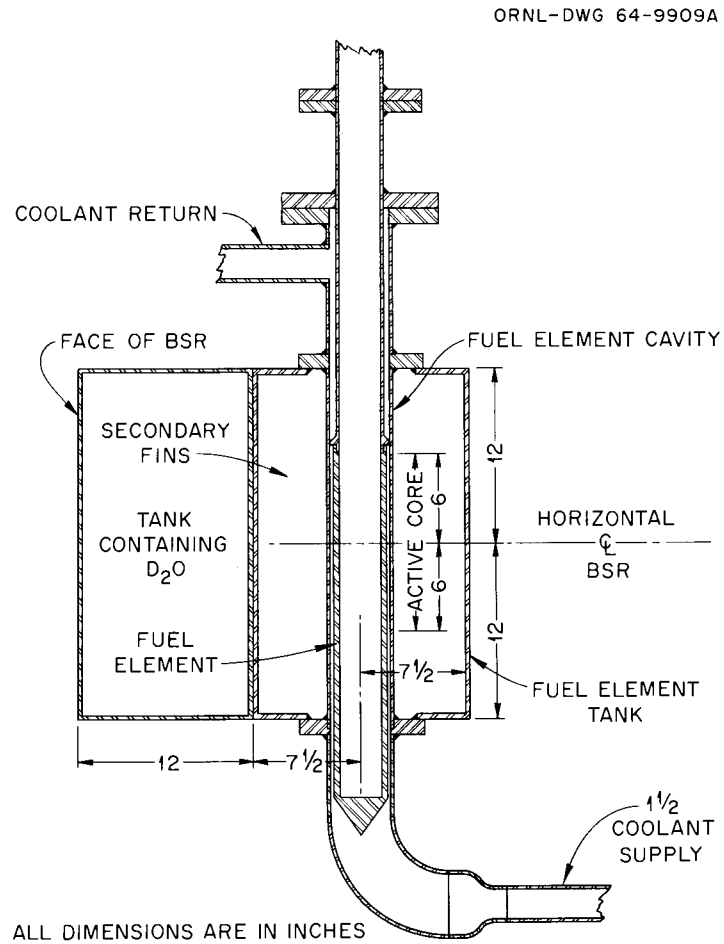

Fig. 28. Vertical Section Through the Tank and Fuel Element Assembly.

Previous reports in this series are:

ORNL-TM-920	Period Ending June 30, 1964
ORNL-TM-960	Period Ending September 30, 1964
ORNL-TM-1000	Period Ending December 31, 1964
ORNL-TM-1100	Period Ending March 31, 1965
ORNL-TM-1200	Period Ending June 30, 1965
ORNL-TM-1270	Period Ending September 30, 1965
ORNL-TM-1400	Period Ending December 31, 1965
ORNL-TM-1500	Period Ending March 31, 1966
ORNL-TM-1570	Period Ending June 30, 1966

[redacted]

INTERNAL DISTRIBUTION

1–3. Central Research Library
4–5. ORNL – Y-12 Technical Library
Document Reference Section
6–15. Laboratory Records
16. Laboratory Records, ORNL R.C.
17. ORNL Patent Office
18. G. M. Adamson, Jr.
19. J. H. Barrett
20. S. E. Beall
21. R. J. Beaver
22. M. Bender
23. R. G. Berggren
24. J. O. Betterton, Jr.
25. D. S. Billington
26. A. L. Boch
27. B. S. Borie
28. G. E. Boyd
29. W. H. Bridges
30. R. B. Briggs
31. W. E. Brundage
32. D. A. Canonico
33. R. M. Carroll
34. J. V. Cathcart
35. G. W. Clark
36. K. V. Cook
37. G. L. Copeland
38. J. H. Crawford
39. J. E. Cunningham
40. J. H. DeVan
41. C. V. Dodd
42. K. Farrell
43. J. I. Federer
44. B. E. Foster
45. A. P. Fraas
46. E. A. Franco-Ferreira
47. J. H Frye, Jr.
48. R. J. Gray
49. W. R. Grimes
50. H. D. Guberman
51. J. P. Hammond
52. D. G. Harman
53. W. O. Harms
54. R. L. Heestand
55–56. M. R. Hill
57. N. E. Hinkle
58. D. O. Hobson
59. H. W. Hoffman
60. W. R. Huntley
61. H. Inouye
62. T. N. Jones
63. G. W. Keilholtz
64. B. C. Kelley
65. J. A. Lane
66. A. P. Litman
67. A. L. Lotts
68. R. N. Lyon
69. H. G. MacPherson
70. R. E. MacPherson
71. M. M. Martin
72. W. R. Martin
73. R. W. McClung
74. H. E. McCoy, Jr.
75. H. C. McCurdy
76. R. E. McDonald
77. D. L. McElroy
78. C. J. McHargue
79. F. R. McQuilkin
80. A. J. Miller
81. E. C. Miller
82. J. G. Morgan
83. F. H. Neill
84. S. M. Ohr
85. P. Patriarca
86. F. H. Patterson
87. A. M. Perry
88. S. Peterson
89. M. L. Picklesimer
90. R. E. Reed
91. P. L. Rittenhouse
92. W. C. Robinson
93. M. W. Rosenthal
94. G. Samuels
95. A. W. Savolainen
96. J. L. Scott
97. O. Sisman
98. G. M. Slaughter
99. G. P. Smith, Jr.
100. N. K. Smith
101. S. D. Snyder
102. I. Spiewak
103. J. T. Stanley
104. W. J. Stelzman
105. J. O. Stiegler
106. D. B. Trauger
107. R. P. Tucker
108. J. T. Venard

[redacted]

[redacted]

109. G. M. Watson
110. A. M. Weinberg
111. J. R. Weir, Jr.
112. W. J. Werner
113. G. D. Whitman
114. J. M. Williams
115. R. O. Williams
116. J. C. Wilson
117. F. W. Young, Jr.
118. C. S. Yust

EXTERNAL DISTRIBUTION

119–122. F. W. Albaugh, Battelle, PNL
123. R. J. Allio, Westinghouse Atomic Power Division
124. R. D. Baker, Los Alamos Scientific Laboratory
125. C. Baroch, Babcock and Wilcox
126. L. Brewer, University of California, Berkeley
127. V. P. Calkins, GE, NMPO
128. W. Cashin, Knolls Atomic Power Laboratory
129. S. Christopher, Combustion Engineering, Inc.
130–131. D. F. Cope, AEC, Oak Ridge Operations
132. G. K. Dicker, Division of Reactor Development and Technology, AEC, Washington
133. D. E. Erb, Division of Reactor Development and Technology, AEC, Washington
134. E. A. Evans, GE, Vallecitos
135. W. C. Francis, Idaho Nuclear Corporation
136. R. G. Grove, Mound Laboratory
137. D. H. Gurinsky, BNL
138. A. N. Holden, GE, APED
139–141. J. S. Kane, University of California, Livermore
142. H. Kato, U.S. Department of the Interior, Bureau of Mines
143. J. H. Kittel, ANL
144. E. J. Kreih, Westinghouse, Bettis Atomic Power Laboratory
145. W. L. Larsen, Iowa State University, Ames Laboratory
146. J. J. Lombardo, NASA, Lewis Research Center
147. J. H. MacMillan, Babcock and Wilcox Company
148. R. Mayfield, ANL
149. M. McGurty, GE-NMPO
150. M. Nevitt, ANL
151. R. E. Pahler, Division of Reactor Development and Technology, AEC, Washington
152. S. Paprocki, BMI
153. D. Ragone, GA
154. B. Rubin, LRL
155. F. C. Schwenk, Division of Reactor Development and Technology, AEC, Washington
156–157. J. M. Simmons, Division of Reactor Development and Technology, AEC, Washington
158. L. E. Steele, Naval Research Laboratory
159. R. H. Steele, Division of Reactor Development and Technology, AEC, Washington
160. W. F. Sheely, Division of Research, AEC, Washington

[redacted]

[redacted]

161. A. Strasser, United Nuclear Corporation
162. A. Taboada, Division of Reactor Development and Technology, AEC, Washington
163. A. Van Echo, Division of Reactor Development and Technology, AEC, Washington
164. R. Van Tyne, Illinois Institute of Technology Research Institute
165. C. E. Weber, Atomic International
166. G. W. Wensch, Division of Reactor Development and Technology, AEC, Washington
167. Division of Research and Development, AEC, Oak Ridge Operations
168–182. Division of Technical Information Extension
183. W. J. Larkin, AEC, Oak Ridge Operations

[redacted]